RESEARCH ARTICLE SUMMARY

MOLECULAR BIOLOGY

Molecular basis of mRNA delivery to the bacterial ribosome

Michael W. Webster*†, Adrien Chauvier†, Huma Rahil†, Andrea Graziadei†, Kristine Charles, Nataliya Miropolskaya, Maria Takacs, Charlotte Saint-André, Juri Rappsilber, Nils G. Walter, Albert Weixlbaumer*

INTRODUCTION: Genetic information stored in DNA is transcribed into messenger RNAs (mRNAs) by RNA polymerase (RNAP) and translated into protein by the ribosome. In prokaryotes, transcription and translation of a gene occur concurrently and in proximity. This allows RNAP and the ribosome to coordinate their functions. A poorly understood aspect of this coupling between transcription and translation machineries is the potential for RNAP to promote ribosome binding to the mRNA that it is transcribing. A mechanism of mRNA "delivery" to the ribosome would protect the intervening mRNA from ribonucleases, suppress the formation of inhibitory RNA structures, and accelerate transcription by coupling it to the translation activity of the trailing ribosome.

Initial contact between mRNA and the ribosome is generally supported by the ribosomal protein bS1, an RNA-binding protein required for translation of most mRNAs in *Escherichia coli*. On the ribosome surface, bS1 is located close to the ribosomal RNA sequence that can base pair with a Shine-Dalgarno (SD) motif in the mRNA. Establishment of a stable complex between the ribosome and mRNA may therefore depend on coordination among bS1, the SD motif, and RNAP.

RATIONALE: In the pathway of bacterial translation initiation, the molecular basis of mRNA accommodation in the ribosome and initiator transfer RNA (tRNA) binding have been characterized. By contrast, structural information on the early stages of translation initiation, in which the mRNA and ribosome first interact, is limited. How RNAP contributes to the initiation of translation is also unclear. We sought to visualize how mRNAs are initially engaged by the bacterial ribos[illegible] using a combination of structural, biophysical, and proteomic methods.

RESULTS: For structural analysis by cryo–electron microscopy (cryo-EM), we prepared a complex in which the small ribosomal subunit was bound to an mRNA emerging from RNAP. Structures were determined of an ensemble of molecular states that reveal two routes of mRNA delivery from RNAP to the ribosome. In the first, the mRNA emerging from RNAP is bound by ribosomal protein bS1. This sheds light on how bS1 supports initial contact with mRNAs and promotes their unfolding for accommodation within the ribosome. The SD motif of the mRNA is base paired with the ribosomal RNA in an orientation not previously described. The continuous path of the mRNA from bS1 to the site of SD motif recognition reveals how bS1 can deliver mRNA to promote stable ribosome-mRNA complex formation before mRNA accommodation and tRNA recognition.

RNAP was located adjacent to bS1 in these structures. This suggested that bS1 contributes to RNAP-mediated delivery of mRNAs to the pioneering ribosome, and we confirmed this by in vitro single-molecule colocalization experiments. An increased rate of ribosome association to mRNAs within RNAP was observed only in the presence of bS1.

In other structural models, RNAP was tethered to the small ribosomal subunit by the coupling factor NusG. Here, the mRNA was delivered to the mRNA entry channel of the ribosome rather than to bS1. This indicates that NusG and its paralog RfaH likely support an alternative pathway of mRNA delivery to the ribosome. Finally, we confirmed that both contact sites between the ribosome and RNAP observed in our reconstituted sample occur in living cells using in-cell chemical cross-linking combined with mass spectrometry.

CONCLUSION: The structural models provide mechanistic insight into the roles of RNAP, bS1, and the SD motif during the early stages of translation initiation. Supported by kinetic analyses of ribosome binding and in-cell structural proteomic data, we present a model of two pathways of mRNA delivery to the bacterial ribosome. ■

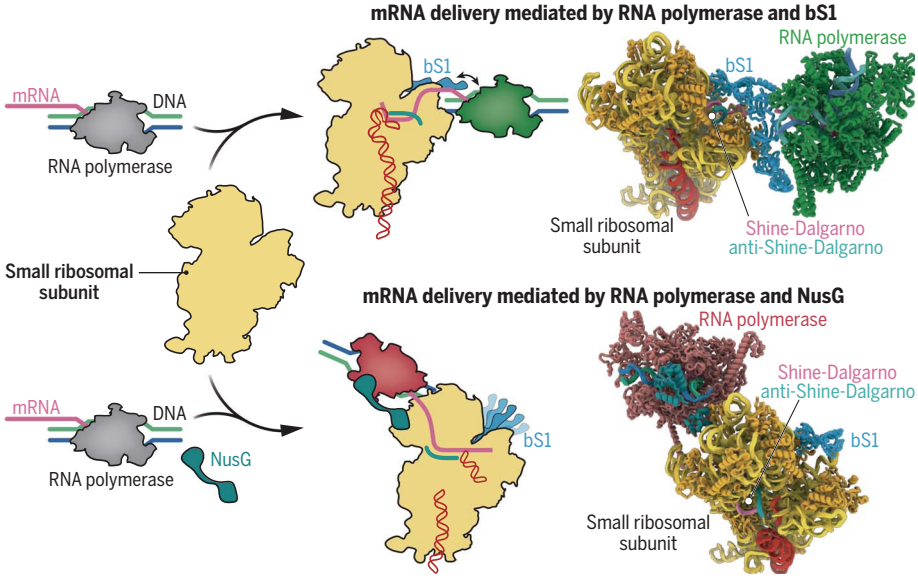

Early steps in ribosome recruitment to mRNA. RNAP (gray) synthesizes mRNA (pink) using DNA as a template. The small ribosomal subunit (yellow) is recruited to mRNA through two pathways. In the first, RNAP (green) contacts the ribosomal protein bS1 (cyan), which binds and channels mRNA to the anti-SD motif (top). Alternatively, NusG (teal) tethers RNAP (red) near the ribosomal entry tunnel (bottom). Translation initiation factors promote translation initiation to proceed (not shown).

The lst of author affiliations is available in the full article online.
*Corresponding author. Email: michael.webster@jic.ac.uk (M.W.W.); albert.weixlbaumer@igbmc.fr (A.W.)
†These authors contributed equally to this work.
Cite this article as M. W. Webster *et al.*, *Science* **386**, eado8476 (2024). DOI: 10.1126/science.ado8476

RESEARCH ARTICLE

MOLECULAR BIOLOGY

Molecular basis of mRNA delivery to the bacterial ribosome

Michael W. Webster[1,2,3,4,5]*†, Adrien Chauvier[6]†, Huma Rahil[1,2,3,4]†, Andrea Graziadei[7]†, Kristine Charles[7], Nataliya Miropolskaya[1,2,3,4], Maria Takacs[1,2,3,4], Charlotte Saint-André[1,2,3,4], Juri Rappsilber[7,8], Nils G. Walter[6], Albert Weixlbaumer[1,2,3,4]*

Protein synthesis begins with the formation of a ribosome-messenger RNA (mRNA) complex. In bacteria, the small ribosomal subunit (30*S*) is recruited to many mRNAs through base pairing with the Shine-Dalgarno (SD) sequence and RNA binding by ribosomal protein bS1. Translation can initiate on nascent mRNAs, and RNA polymerase (RNAP) can promote the recruitment of the pioneering 30*S*. Here, we examined 30*S* recruitment to nascent mRNAs using cryo–electron microscopy, single-molecule fluorescence colocalization, and in-cell cross-linking mass spectrometry. We show that bS1 delivers the mRNA to the ribosome for SD duplex formation and 30*S* activation. Additionally, bS1 and RNAP stimulate translation initiation. Our work provides a mechanistic framework for how the SD duplex, ribosomal proteins, and RNAP cooperate in 30*S* recruitment to mRNAs and establish transcription-translation coupling.

Bacterial protein synthesis begins with the recruitment of the small ribosomal subunit (30*S*) to an mRNA. The initial interaction between 30*S* and mRNAs is supported by the ribosomal protein bS1, which is an RNA-binding protein required to efficiently translate most mRNAs in *Escherichia coli* (*1*). The 30*S*-mRNA complex can be stabilized by base pairing of a Shine-Dalgarno (SD) sequence motif in the mRNA, located upstream of the translation start site, to the anti-SD (aSD) sequence at the 3′ end of the 16*S* rRNA within the 30*S* (*2*–*4*). The resulting SD-aSD duplex is stabilized by ribosomal protein bS21 in *E. coli* (*5*).

The 30*S* can be recruited to mRNAs that are being transcribed because of the spatial proximity of the transcription and translation machinery in prokaryotes (*6*–*9*). Coordination of translation initiation with transcription supports the translation of nascent transcripts, enhanced transcription elongation through the establishment of transcription-translation coupling, protection of the mRNA from ribonucleases, and minimization of inhibitory RNA structure formation (*10*, *11*). The aSD sequence and bS1 are located near the 30*S* mRNA exit channel. This ribosome region also interacts with RNA polymerase (RNAP) (*12*). The spatial proximity of the SD-aSD duplex, bS1, bS21, and RNAP suggests that their activities could be coordinated during the initiation of translation.

The early stages of the 30*S* preinitiation complex (PIC) assembly pathway involve multiple steps (Fig. 1A) (*13*). The mRNA transits from an initial interaction site on the ribosome (a "standby site") to an accommodated position within the ribosome mRNA-binding channel to scan for the start codon (*14*–*17*). This can require mRNA secondary structure unfolding, which is promoted by bS1 (*18*, *19*). The 30*S*-decoding center, which monitors binding of transfer RNAs (tRNAs) to mRNA codons and ensures translational fidelity, may not be organized in all free 30*S*. It has been proposed that some 30*S* must be "activated" by the repositioning of 16*S* rRNA helix 44 (h44) to form a functional decoding center (*20*–*23*), although the characteristics of the inactive 30*S* population in vivo remain unclear. A mechanistic understanding of these processes is lacking, including their potential coordination with each other.

Translation can initiate on transcripts emerging from RNAP. *E. coli* RNAP commonly pauses near the translation start site and is likely to coordinate with the ribosome and establish coupled translation (*24*, *25*). NusG and its paralog RfaH act as "coupling factors" that can bind concurrently to the ribosome and RNAP. RfaH can promote translation in vivo when the ribosome-binding sequence is removed (*6*), and NusG can promote 30*S* recruitment in vitro (*7*). This suggests that the stages of 30*S* recruitment to nascent mRNA may also be mediated by coupling factors.

We sought to understand how translation initiation is supported by ribosomal proteins, the SD motif, RNAP, and NusG. Cryo–electron microscopy (cryo-EM) structures of complexes of 30*S* and transcribing RNAP reveal that bS1 can deliver the mRNA to the ribosome for SD-aSD duplex formation and 30*S* activation. Single-molecule kinetic analysis of ribosome binding (SiM-KARB) (*26*) and in-cell cross-linking mass spectrometry (CLMS) showed that bS1 also mediates the accelerated recruitment of 30*S* to RNAP-bound mRNAs. These findings provide mechanistic insight into the early stages of bacterial translation initiation and how coupling between the transcription and translation machineries is established.

Structures of translation initiation complexes associated with RNAP and bS1

To structurally characterize molecular assemblies that occur during the recruitment of 30*S* to a nascent mRNA, we reconstituted complexes with 30*S* bound to the mRNA of a transcription elongation complex [TEC, a complex consisting of RNAP, a nascent mRNA transcript annealed to template DNA (tDNA), and non-template DNA (ntDNA)], initiator tRNA (fMet-tRNA^{fMet}), and NusG using purified *E. coli* components. The mRNA sequence mimics a state in which RNAP has transcribed 38 nucleotides beyond the start codon of a gene that has a strong SD motif (RNA-38; Fig. 1A and fig. S1A). This length reflects a natural transcript that exhibits TEC-stimulated 30*S* recruitment (*7*), but the sequence produces minimal RNA secondary structure (fig. S1B). Three cryo-EM reconstructions were obtained by two different particle classification strategies that were distinguished by the presence or absence of the TEC and its position relative to the 30*S* (Fig. 1, B to D, and fig. S1, C and D).

In the first reconstruction, TEC density was adjacent to the mRNA exit channel. Independent refinements focused on the 30*S* or TEC and additional particle subset selections were required to resolve each region of the complex (Fig. 1B and figs. S1, C and D, and S2). The substantial structural variability suggests that the 30*S*-TEC complex forms through concurrent binding to the flexible mRNA rather than through a consistent interaction interface, as in uncoupled 70*S*-TEC expressome complexes (*27*). Structural models of the 30*S* and TEC were built into reconstructions resolved to 2.8 and 4.2 Å, respectively (Fig. 1E). Further focused particle classification and refinement resolved bS1 and mRNA between the 30*S* and TEC (Fig. 1B). A structural model of 30*S* with bS1 and mRNA was built from the reconstruction resolved to 2.6 Å (Fig. 1F). Focused particle classification indicated that the 30*S* head domain oscillates with respect to the 30*S* body domain, producing variation in the mRNA-binding channel width. Unexpectedly, fMet-tRNA^{fMet}

[1]Department of Integrated Structural Biology, Institut de Génétique et de Biologie Moléculaire et Cellulaire (IGBMC), Illkirch Cedex, France. [2]Université de Strasbourg, Illkirch Cedex, France. [3]CNRS UMR7104, Illkirch Cedex, France. [4]INSERM U1258, Illkirch Cedex, France. [5]Department of Biochemistry and Metabolism, John Innes Centre, Norwich Research Park, Norwich, UK. [6]Single Molecule Analysis Group, Department of Chemistry and Center for RNA Biomedicine, University of Michigan, Ann Arbor, MI, USA. [7]Technische Universität Berlin, Chair of Bioanalytics, Berlin, Germany. [8]Wellcome Centre for Cell Biology, University of Edinburgh, Max Born Crescent, Edinburgh, UK.
*Corresponding author. Email: michael.webster@jic.ac.uk (M.W.W.); albert.weixlbaumer@igbmc.fr (A.W.)
†These authors contributed equally to this work.

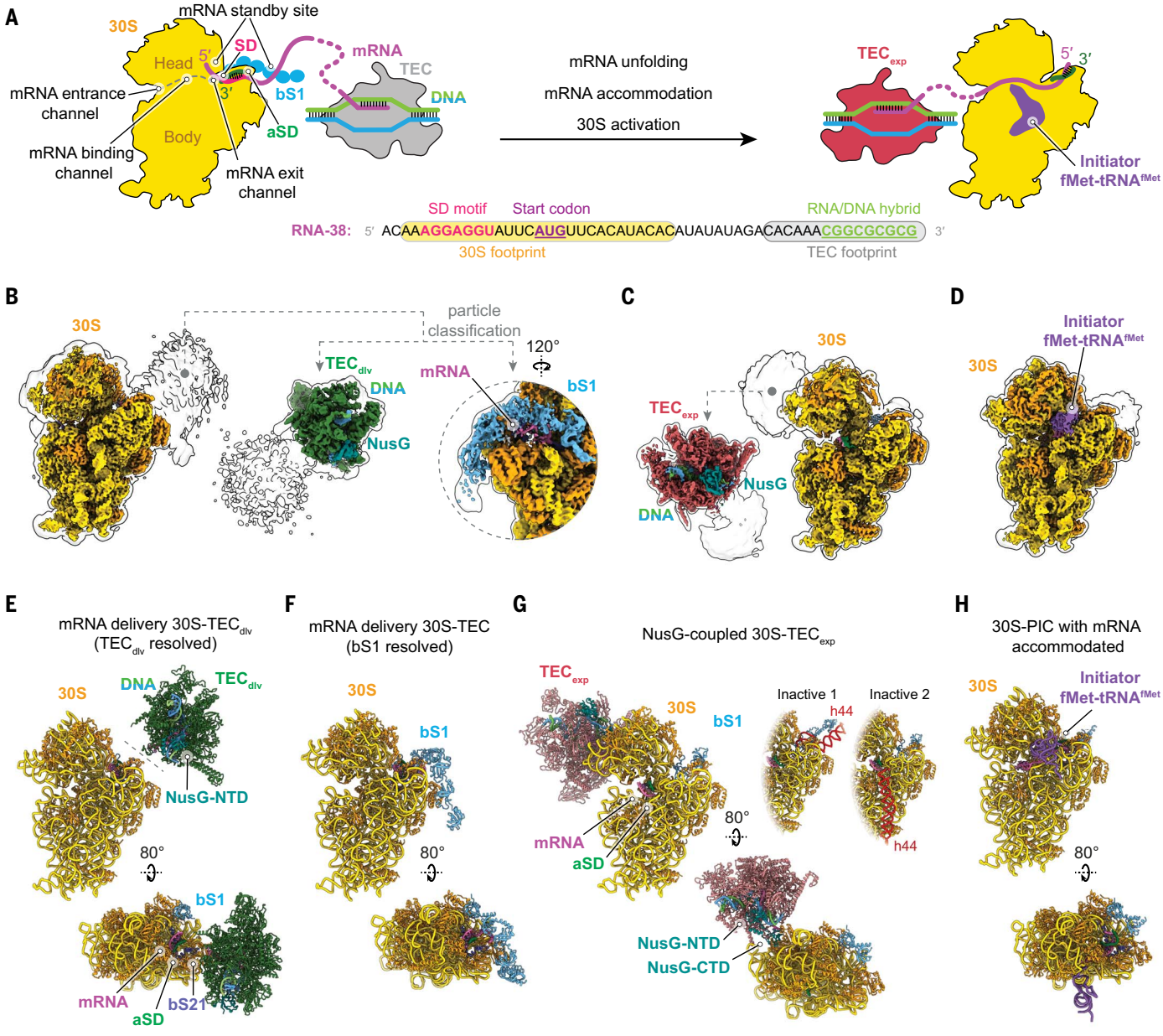

Fig. 1. Cryo-EM reconstructions of translation initiation complexes linked to transcription. (**A**) Recruitment of 30*S* to (nascent) mRNA involves multiple steps, including 30*S* activation, binding of an mRNA region to a standby site on the 30*S*, mRNA unfolding by bS1 and accommodation, positioning of the start codon in the ribosomal P-site, and reorganization to enable eventual formation of a coupled transcription-translation complex. Translation initiation factors (IFs, omitted for clarity) support several steps. The mRNA used in our work is shown below the schematic. (**B**) The reconstruction of the 30*S*-TEC_{dlv} mRNA delivery complex (gold, composite map; white, map filtered to 10 Å) revealed density surrounding the 30*S* platform. Focused classification identified a TEC (green, focused TEC_{dlv} map; white, map filtered to 10 Å) flexibly associated with 30*S* and a particle subset in which bS1 was resolved (cyan, focused map; white, map filtered to 10 Å). (**C**) The reconstruction of the NusG-coupled 30*S*-TEC_{exp} complex revealed density close to the mRNA entry channel. Focused classification identified this to be a TEC (red, focused TEC_{exp} map) coupled through NusG to ribosomal protein uS10. (**D**) The reconstruction of a 30*S*-PIC with accommodated mRNA in the ribosomal P-site bound to initiator tRNA (purple). (**E** to **H**) Models of mRNA delivery complex (30*S*-TEC_{dlv}) with TEC_{dlv} resolved (green), mRNA delivery complex with bS1 resolved (cyan), 30*S*-TEC_{exp} complex in two inactive states with a TEC_{exp} resolved (red) and coupled to 30*S* through NusG (teal), and 30*S*-PIC with initiator tRNA (purple) bound to an accommodated mRNA.

was observed to bind the solvent side of the 30*S* neck region, which connects the head and body domains, with the highest occupancy when the 30*S* head domain was closed and the mRNA-binding channel was narrow (fig. S2, D and E, and movie S1). The structural features of these reconstructions, detailed below, are consistent with a complex that precedes mRNA accommodation in the 30*S* mRNA-binding channel. We therefore refer to these as "mRNA delivery" complexes, in which the mRNA occupies a standby site, and refer to the ribosome and TEC as "$30S_{dlv}$" and "TEC_{dlv}," respectively.

In the second reconstruction, the TEC was adjacent to the mRNA entrance channel and connected to the 30*S* head by NusG (Fig. 1C and figs. S1C and D, and S3). An independent

focused refinement was similarly required to obtain a reconstruction of the TEC, indicating that the NusG-coupled TEC is mobile and occupies a position as in the NusG-coupled expressome (TEC_{exp}; figs. S1, C and D, and 3A) (*27*). The range of TEC_{exp} movement relative to the 30*S* was substantially less than in the mRNA delivery complex, likely because of the limited flexibility of the linker between the NusG domains that contact each complex and the mRNA tethering the TEC_{exp} to the 30*S* (movie S2). Whereas the mRNA delivery complexes contained the active 30*S* conformation, the NusG-coupled 30*S*-TEC_{exp} complexes contained inactive 30*S*. Reconstructions were obtained of two inactive conformations after further particle classification resolved to 3.3 and 3.1 Å resolution, into which atomic models were built (Fig. 1G and fig. S3B).

The third reconstruction lacked TEC density and resembled a PIC bound to fMet-$tRNA^{fMet}$ (Fig. 1D and figs. S1, C and D, and S4) (*28*). It is likely that a small fraction of 30*S* bound free mRNA or a nucleic acid scaffold that was not stably loaded with RNAP. The PIC model was constructed from a reconstruction resolved to 3.1 Å (Fig. 1H). As detailed below, the PIC model reveals the role of bS21 in stabilizing the position of the SD-aSD duplex upon mRNA accommodation.

SD-aSD duplex movement supports mRNA delivery

In the mRNA delivery complex, mRNA is bound to the aSD motif in the ribosome mRNA exit channel and also to bS1 and to TEC_{dlv}. Based on the roles of the aSD and bS1 in establishing the initial contact between 30*S* and mRNA (*13*), we hypothesize that this is a state that can precede mRNA accommodation in the 30*S*. This is supported by an observed difference in the SD-aSD duplex position between the mRNA delivery and PICs (Fig. 2A). In the PIC structure, the SD-aSD duplex is within the 30*S* mRNA exit channel with the mRNA 5′ end at the ribosome periphery, and downstream mRNA accommodated for tRNA binding. In the mRNA delivery complex, the SD-aSD duplex is similarly located within the 30*S* mRNA exit channel but inverted in its orientation. This allows the mRNA transcribed after the SD motif to interact with bS1, consistent with an initial encounter between mRNA and 30*S* (*14*–*17*). If the mRNA delivery complex does precede mRNA accommodation, then the SD-aSD must reorient during mRNA transit from this delivery complex to the accommodated complex (movie S3).

In both the delivery and accommodated mRNA positions, the SD-aSD duplex is bordered by ribosomal proteins bS1, uS2, bS21, and bS18 (Fig. 2A). In each, bS21 secures the RNA duplex between two helical segments through conserved basic residues in an arrangement analogous to chopsticks

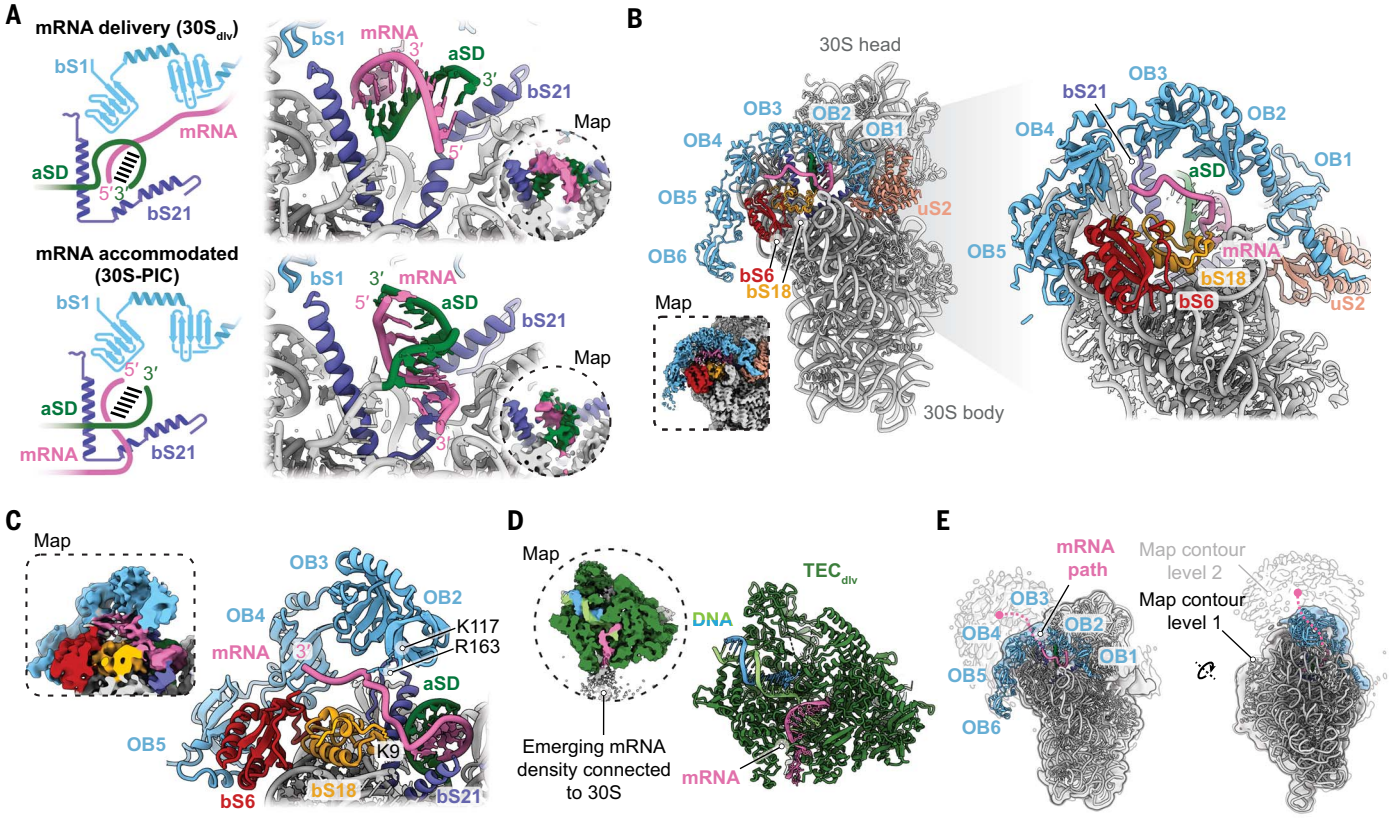

Fig. 2. mRNA delivery involves SD-aSD duplex inversion, bS1 arch formation and binding of mRNA, and TEC_{dlv} association. (**A**) Schematic (left) and structural model and cryo-EM map (right) of the 30*S* platform region comparing mRNA delivery complexes (top) and 30*S*-PIC (bottom). The SD-aSD duplex orientation is inverted in mRNA delivery complexes compared with an accommodated mRNA by rotation of the aSD close to 16*S* rRNA residue 1533. (**B**) Structural model and cryo-EM map (bottom left) of the 30S_{dlv} with bS1 resolved. The RNA-binding surfaces of bS1 face the 30*S* to form a pore for the delivery of mRNA (magenta). The zoomed-in structural model on the right indicates a representative mRNA path. The mRNA binds bS1-OB2 to bS1-OB4 and connects bS1-OB2 and the aSD sequence (green) at the 16*S* rRNA 3′-end. bS21 stabilizes the SD-aSD duplex. bS1 is anchored to ribosomal protein uS2 (salmon) through its N-terminal helix and bS1-OB1. bS1-OB4 and bS1-OB5 interact with ribosomal protein bS6 (red). (**C**) Segmented cryo-EM map showing mRNA density (magenta) associated with bS1 (cyan). Conserved residue K9 in bS18 (orange) stabilizes a sharp turn in the mRNA path so that it can interact with bS1-OB2 bordered by K117 and R163. (**D**) In mRNA-delivery complexes, the TEC_{dlv} orientation directs nascent mRNA toward the 30*S*. TEC_{dlv} focused cryo-EM reconstruction (left) shows density connecting the nascent mRNA to the 30*S* at lower contour levels (gray). (**E**) Low-pass-filtered maps showing TEC_{dlv} density close to bS1-OB3 and bS1-OB4, suggesting this to be the primary contact site between 30S_{dlv} and TEC_{dlv}.

(fig. S5, A and B). In the PIC, the SD-aSD position resembles that of *E. coli* 70*S* (*29*) but differs to varying degrees from that of *Thermus thermophilus* ribosomes, which lack bS21 (*28*, *30*, *31*) (fig. S5, C and D). The bS21 N-terminal α-helix interacts with the 16*S* rRNA, and the C-terminal α-helix interacts with the mRNA.

In the mRNA delivery complex, bS21 interacts with the 16*S* rRNA but not with the mRNA. The bS21 N-terminal α-helix contacts the 16*S* 3′ end, as in the PIC, but with opposite directionality, and the C-terminal α-helix contacts upstream 16*S* nucleotides. The mRNA 5′ end exits the ribosome close to uS11 and bS21 toward 16*S* rRNA helix 23. The presence of contacts between bS21 and the 16*S* rRNA leads us to speculate that the aSD position observed could be adopted before the arrival of the mRNA and facilitate scanning for the SD site by mRNA sliding until stable base pairing is achieved.

bS1 delivers mRNA to the ribosome

The ability of bS1 to bind and unwind mRNA is key to translation initiation. However, resolving how bS1 contacts mRNA has been challenging because of the dynamic nature of bS1: The six bS1 OB domains are flexibly connected and vary in their position in published structures (*32*, *33*). The interaction of bS1 with an accommodated mRNA bound to the aSD was recently observed in a 70*S* complex (*29*). Our model of the mRNA delivery complex, which includes a longer mRNA and all six OB domains of bS1, clarifies the structural basis of cooperativity between bS1 and the aSD.

bS1 forms a semicircular arch composed of domains OB1 to OB4 (Fig. 2B). The ends of the arch are anchored on one end by binding of the N terminus and OB1 to uS2, as previously characterized (*29*, *34*), and on the other by binding of OB4 and OB5 to bS6. The OB2 and OB3 domains are suspended above the mRNA exit channel on the 30*S* platform side. Together with bS6 and bS18, these domains produce a narrow pore that is lined with basic residues. The mRNA enters the ribosome by threading through this pore.

The local resolution of the cryo-EM reconstruction is limited to ~5 Å in the bS1-mRNA region (fig. S2C). The model is consequently representative of an ensemble of structurally similar complexes. In reconstructions of other particle subsets in the mRNA delivery complex, an arch conformation of bS1 was observed that was not anchored to bS6 (fig. S5E). The position of bS1 detached from bS6 is less defined, and the OB5 and OB6 domains were poorly resolved in this reconstruction.

Ten nucleotides of mRNA downstream of the SD were sufficiently ordered for the path to be traced in our representative model (Fig. 2C). Downstream of the SD, the mRNA path turns ~90° to allow the mRNA to contact the basic N terminus of bS18, including conserved residue K9, and the OB2 domain of bS1, including K117 and R163. Further downstream, the mRNA contacts the inner concave surface of bS1 domains OB3 and OB4, and bS6 on the outer 30*S* surface. The mRNA was not observed to contact bS1 domains OB5 and OB6.

RNAP can deliver mRNA to the ribosome through bS1

A TEC model was obtained from a reconstruction of a subset of mRNA delivery particles (TEC_{dlv}) (Fig. 2D). TEC_{dlv} structurally resembles a NusG-bound TEC (*35*, *36*), with additional density connecting the RNA exit channel to the 30*S*. This is consistent with concurrent binding of TEC_{dlv} to the 30*S*-bound mRNA. In the $30S_{dlv}$ reconstruction from the same particles, the arch comprising bS1 domains OB1 to OB4 is resolved upon low-pass filtering. The TEC_{dlv} density is adjacent to bS1 domains OB3 and OB4, consistent with the mRNA entrance point to the $30S_{dlv}$ identified when the bS1 arch was fully resolved (Fig. 2E).

bS1 can interact with RNAP (*12*, *37*), and this could occur alongside concurrent mRNA binding to stabilize the mRNA delivery complex architecture. However, we did not observe these contacts in focused reconstructions. To clarify whether these interactions occur in 30*S*-TEC_{dlv} complexes, we examined the interaction of bS1 with RNAP and a TEC using purified components (fig. S6A). This showed that bS1 interacts with RNAP in the absence of a nascent mRNA but only associates stably in the presence of a long mRNA in the TEC.

Whereas the N terminus of NusG is bound to the TEC_{dlv}, the C terminus of NusG does not interact with the ribosome because of its separation from its binding site on uS10 in the coupled expressome (*6*, *27*, *38*). This observation, and the inability to resolve $30S_{dlv}$ and TEC_{dlv} within a single reconstruction, shows that the transcription and translation machineries remain structurally independent in the mRNA delivery complex.

The independence of the transcription and translation machineries in the 30*S*-TEC_{dlv} contrasts a 30*S*-RNAP model prepared in the absence of mRNA and DNA (*12*). In the 30*S*-RNAP complex, extensive contacts were observed between RNAP and ribosomal proteins. Structural superposition revealed that ribosome-bound bS1 in the 30*S*-TEC_{dlv} overlaps with the position of RNAP in the 30*S*-RNAP complex (fig. S6B) (*12*). The structural differences are therefore a consequence of both the presence of nucleic acids within the TEC and the interaction of bS1 with the ribosome in our 30*S*-TEC_{dlv} sample.

mRNA delivery by NusG-coupled RNAP

The model of the NusG-coupled 30*S*-TEC_{exp} complex shows that NusG can tether RNAP to 30*S* as it does to 70*S* in the NusG-coupled expressome (Fig. 3A) (*27*, *38*). The NusG C-terminal domain interacts with uS10 on the 30*S* head, and the nascent mRNA contacts uS3 before entering the ribosome through the mRNA entrance channel. The occurrence of both the NusG-coupled 30*S*-TEC_{exp} and the mRNA delivery 30*S*-TEC_{dlv} in our sample suggests a competition between interaction interfaces that initiates complex formation. We hypothesize that if the ribosome binds NusG through uS10 before it binds the mRNA through bS1, then delivery through the mRNA entrance channel is favored.

mRNA delivery by bS1 promotes 30*S* activation

The free 30*S* adopts predominantly inactive conformations both in vivo and when purified (*22*, *23*). 30*S* activation involves repositioning of h44 to form a functional decoding center and relocation of the aSD from the A-site to the mRNA exit channel (*23*). Although activation was proposed to be promoted by mRNA accommodation and by IFs, the mechanism is not well understood (*20*).

We observed an active 30*S* conformation in our PIC model that is likely stabilized by contacts involving accommodated mRNA, fMet-$tRNA^{fMet}$, and the 30*S*. The 30*S* also adopted an active conformation in the mRNA delivery complex despite mRNA not being accommodated. This demonstrates that 30*S* activation can occur independently of IFs and before mRNA accommodation.

In the NusG-coupled 30*S*-TEC_{exp}, inactive 30*S* was observed in two conformations (Fig. 3, A and B) reminiscent of late stages in ribosome maturation (*39*). The structural features of the inactive 30*S* supports a model in which mRNA delivery by bS1 enables 30*S* activation. In one NusG-coupled 30*S*-TEC_{exp} model, bS1 binds h44 in a way that is mutually exclusive with bS1 binding mRNA in the delivery complex (Fig. 3A). The base of h44 is confined within the mRNA exit channel, and focused classification revealed that it is bound by bS1 in a subset of particles (fig. S1D and movie S4). The remainder of h44 is not resolved, suggesting that noncanonical base-paired nucleotides produce hinges that make the h44 tip mobile in this position. bS1 interaction with h44 is likely supported by transient single-stranded conformations of the noncanonical base pairing expected to occur in h44, although the details of this were not resolved (Fig. 3C). We call this bS1-clasped 30*S* conformation "inactive state 1."

In inactive state 1, the incoming mRNA cannot bind bS1 OB2 domain and the aSD in the 30*S* platform. It is likely that an equilibrium exists with a smaller fraction in an alternative conformation observed in the NusG-coupled 30*S*-TEC particles that we call "inactive state 2." Here, h44 is partially accommodated at the subunit interface as observed in inactive free *E. coli* 30*S*, idle *Staphylococcus aureus* 30*S*, and ribosome

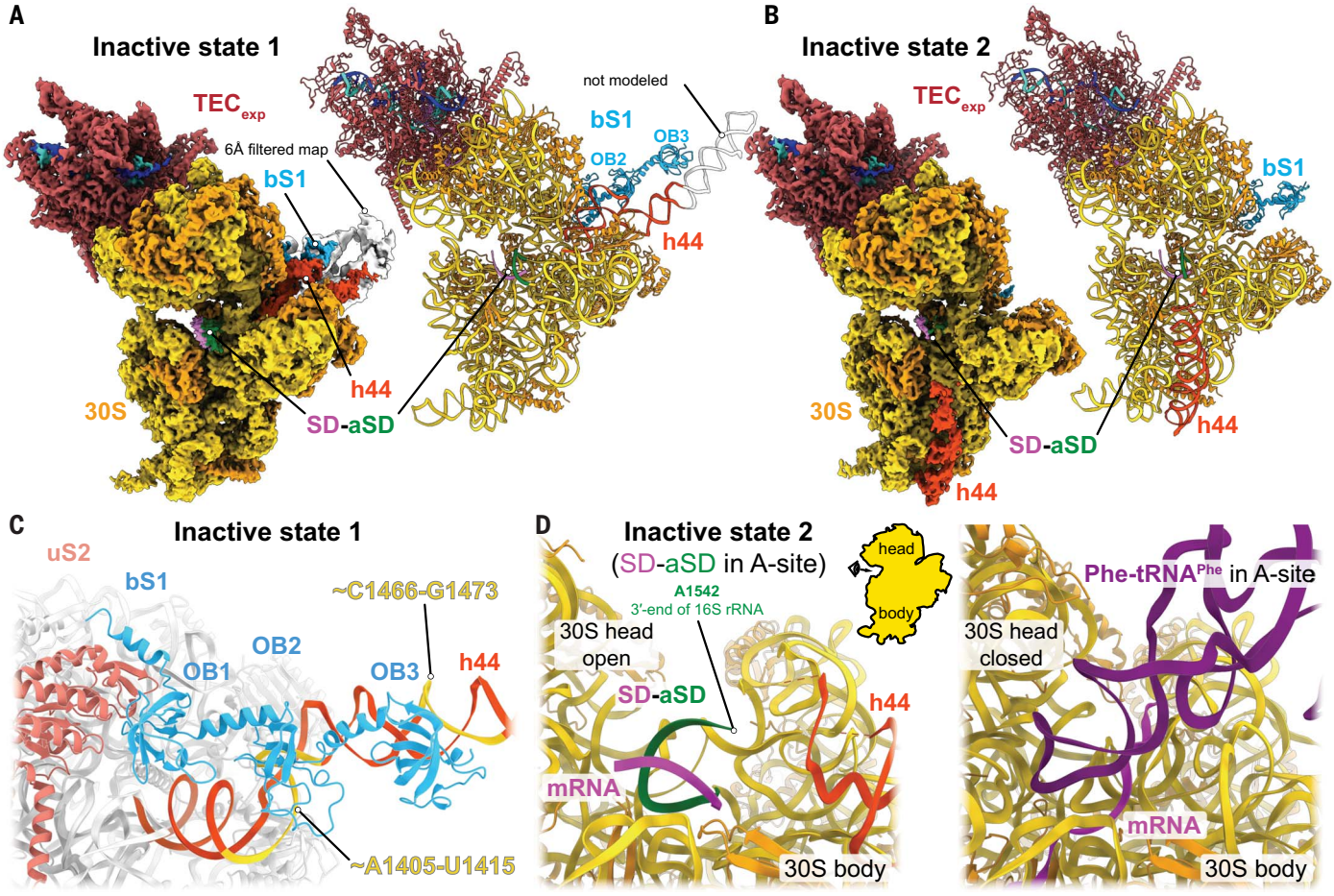

Fig. 3. 30*S* activation regulation by bS1 and SD-aSD position. Two inactive 30*S* conformations were identified by classification of NusG-coupled 30*S*-TEC$_{exp}$ particles. In both, the TEC is coupled to 30*S* by NusG and delivers the mRNA to the mRNA entry channel as observed in transcribing-translating expressomes. (**A**) Cryo-EM reconstruction (left, composite map; white, h44 and bS1 map filtered to 6 Å and overlaid) and structural model (right) of inactive state 1 showing that h44 in the mRNA exit channel interacts with ribosomal protein bS1. The SD base pairs with the aSD in the ribosomal A-site and prevents correct folding of the decoding center. (**B**) In inactive state 2, h44 has relocated to the 30*S* subunit interface side, but the decoding center has not correctly folded. mRNA delivery by TEC$_{exp}$ produced SD-aSD base pairing in the ribosomal A-site, hindering activation as in inactive state 1. (**C**) The positions of bS1 and h44 in inactive state 1 suggest that bS1 OB2 and OB3 contact h44. (**D**) The position of the SD-aSD helix in inactive states (left, only inactive state 2 shown) overlaps with an accommodated tRNA bound to the A-site codon in a TEC (PDB: 6ZTJ, right).

assembly intermediates (*23*, *39*, *40*). Transient release of h44 from bS1 was observed by three-dimensional (3D) variability analysis, which is expected to allow mRNA delivery to bS1 (movie S4). This prevents h44 from returning to the bS1-clasped inactive conformation and thereby shifts the equilibrium toward the active 30*S*.

In inactive states 1 and 2, the SD-aSD duplex is in the ribosomal A-site close to where the aSD is positioned in inactive free 30*S* (Fig. 3D) (*23*). This position overlaps with the folded decoding center and the IF1-binding site. Therefore, repositioning of the SD-aSD is needed for 30*S* activation to subsequently occur. Although it has been argued that free 30*S* predominantly adopts inactive conformations in vivo (*22*), their prevalence and their resemblance to inactive states observed in vitro is uncertain. It is therefore unclear whether the formation of SD-aSD duplex in the A-site is a general consequence of mRNA delivery through the mRNA entrance channel. Analysis of mRNAs with more nucleotides between the SD motif and the TEC may show that the SD-aSD duplex can alternatively form in the 30*S* exit channel as in 70*S*-TEC expressome complexes (*27*).

mRNA delivery can occur on translating 70*S* ribosomes

The mRNA delivery 30*S*-TEC$_{dlv}$ model suggests that a TEC$_{dlv}$ could, in principle, present nascent mRNA to actively translating 70*S* ribosomes as it does to free 30*S*. Further analysis of the cryo-EM dataset used to characterize the uncoupled expressome (*27*) yielded a reconstruction from a 70*S*-TEC particle subset in which the TEC was associated with the ribosomal mRNA exit channel (TEC$_{dlv}$; fig. S7, A to C and table S1).

As in the mRNA delivery 30*S*-TEC$_{dlv}$ reconstruction, TEC$_{dlv}$ density is strongest near the mRNA exit channel and bS1 and the relative orientations of the ribosome and TEC$_{dlv}$ are broadly distributed (fig. S7D). A structural model representing a single arrangement within the dynamic ensemble was generated by positioning TEC$_{dlv}$ and 70*S* models in focused reconstructions at the position with the highest occupancy in a distribution plot of relative orientations (fig. S7, D and E). Compared with the expressome, no substantial differences in the 70*S* or TEC$_{dlv}$ structures were identified.

In the 70*S*-TEC$_{dlv}$ complex, the SD-aSD duplex orientation is the same as that of the mRNA delivery 30*S*-TEC$_{dlv}$ models and inverted relative to the expressome particles that contain accommodated mRNA in the same dataset (Fig. 2A and fig. S7, E and F). A second mRNA molecule is accommodated in the main mRNA-binding

channel that interacts with tRNAs (fig. S7F). This complex therefore recapitulates delivery of an mRNA to the aSD during translation of a different transcript. Whether ribosomes queue mRNAs in this manner in bacterial cells, and how this is suppressed if not, remains to be assessed.

Recruitment of 30*S* to mRNA is promoted by RNAP and bS1

The proximity of the TEC_{dlv} to bS1 in the mRNA delivery complex model suggests that they co-operate in a way that may not be resolved by cryo-EM because of structural heterogeneity. We therefore sought to determine whether bS1 contributes to the recruitment of 30*S* to TECs over mRNAs that are not bound to RNAP.

SiM-KARB (*26*) was performed with Cy3-labeled RNA with the same sequence used for structural analyses (table S2). The RNA was either surface attached through a surface-immobilized DNA oligomer or as a paused TEC (pTEC) formed using a biotin-streptavidin roadblock (fig. S8A). RNA was visualized by total internal reflection fluorescence (TIRF), and the binding of Cy5-labeled 30*S* (*26*, *41*) was monitored by fluorescence colocalization within a diffraction limited spot (Fig. 4A and fig. S8A). Experiments were performed with 30*S* that contained or lacked bS1 to assess its kinetic contribution.

Time traces for 30*S* binding to individual transcripts showed repeated transient associations of 30*S* with RNA (fig. S8B). Two association and two dissociation rate constants were derived (Fig. 4B and table S3). pTEC was bound by bS1-containing 30*S* with an overall association

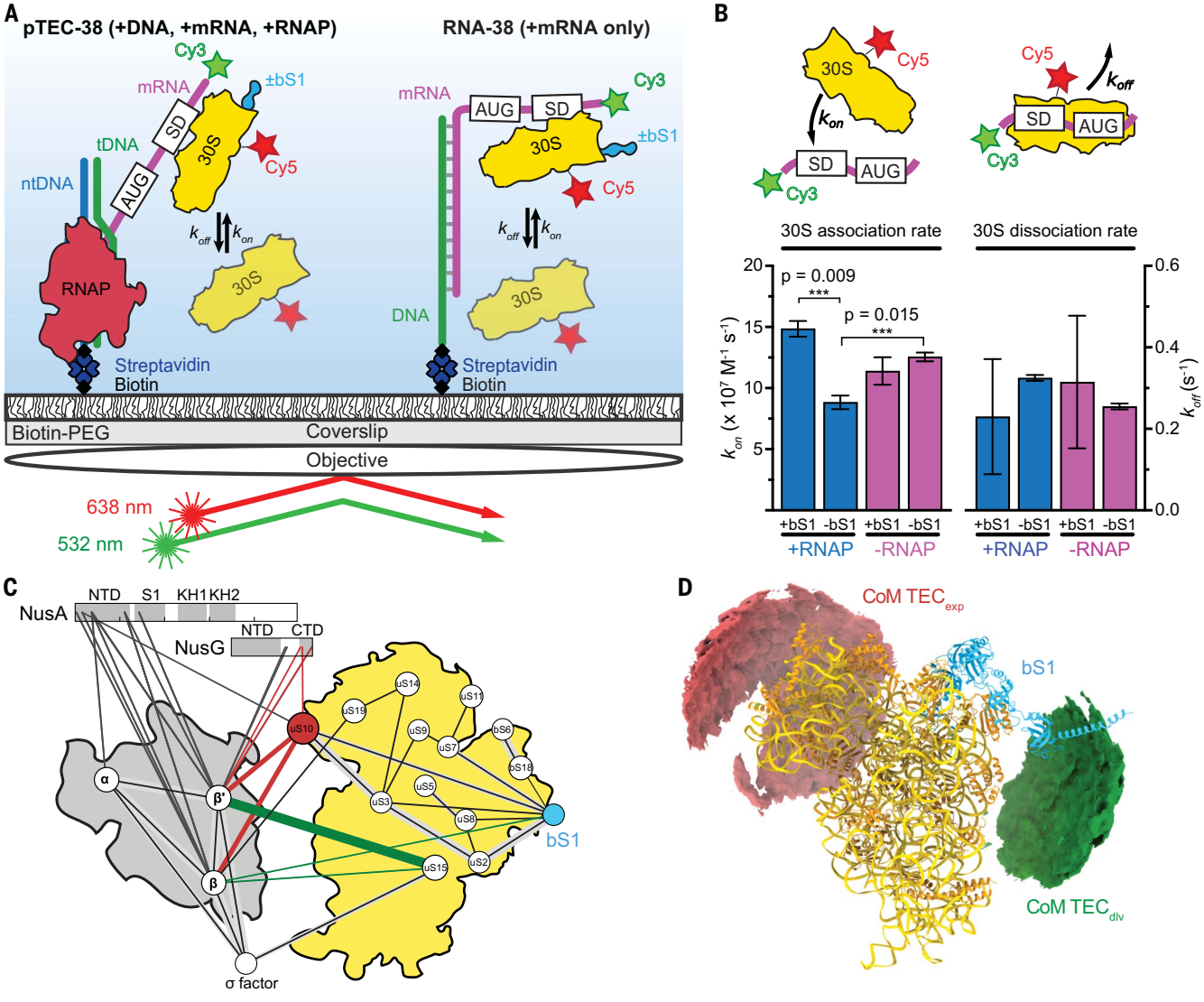

Fig. 4. 30*S* recruitment to mRNA is promoted by bS1 and a TEC, and in-cell cross-linking confirms TEC_{dlv} position. (**A**) Schematic of SiM-KARB experiment showing immobilization of pTEC-38 (left) or RNA-38 (right) and TIRF measurement of 30*S* binding. (**B**) Association (k_{on}) and dissociation (k_{off}) rate constants calculated from hidden Markov models for 30*S* binding to pTEC-38 (blue) and RNA-38 (purple) in the presence (+) or absence (−) of bS1. Values of k_{on} and k_{off} are reported in table S3. The total number of molecules analyzed were $N_{(pTEC+bS1)}$ = 180, $N_{(pTEC-bS1)}$ = 197, $N_{(RNA-38+bS1)}$ = 130, and $N_{(RNA-38-bS1)}$ = 152. ***P < 0.01, **P < 0.025, *P < 0.05. (**C**) In-cell CLMS interaction map of RNAP and ribosomal proteins. Cross-links between NusG and uS10 (red line) are consistent with NusG-coupled 30*S* and expressome models. Cross-links among β-bS1, β-uS15, and β′-uS15 (green lines) are consistent with mRNA-delivery complex models. Line thickness indicates number of cross-links supporting each interaction: thin lines, single cross-link; medium lines, two cross-links; and thick lines, more than two cross-links). (**D**) 30*S*-RNAP subunit CLMS flexibility analysis. Accessible interaction space analysis showing the volume occupied by the RNAP center of mass (CoM) consistent with at least two CLMS restraints performed with DisVis (*79*). Structural models of ribosome-TEC_{exp} complexes are consistent with one identified region (red density), and models of 30*S*-TEC_{dlv} or 70*S*-TEC_{dlv} complexes are consistent with the other identified region (green density).

constant that was ~20% faster than the RNA without RNAP, consistent with previous results on a different transcript (*7*). By contrast, pTEC was bound by 30*S* lacking bS1 ~40% more slowly than RNA without RNAP. Dissociation rate constants for 30*S* were not significantly changed by the presence of bS1 or RNAP, likely because complex stability with this transcript is predominantly maintained by a strong SD-aSD duplex interaction (Fig. 4B). We conclude that bS1 allows 30*S* to bind more rapidly to transcripts associated with RNAP.

In-cell CLMS reveals an interaction between bS1 and RNAP

We further investigated contact between transcription and translation complexes in vivo by in-cell CLMS. Affinity purification of RNAP from cross-linked *E. coli* cells was used to enrich the transcription-associated proteome. In-cell CLMS revealed 1458 residue pairs, of which 523 were heteromeric [5% cross-link–level false discovery rate (FDR)] (fig. S9 and table S4). This network reveals that ribosomal proteins interact directly with RNAP and with the coupling factors NusA and NusG in *E. coli* cells.

Cross-links were observed between RNAP and ribosomal proteins bS1 and uS15. The latter is situated on the 30*S* platform adjacent to the RNAP position in the mRNA-delivery complexes. These support the occurrence of the mRNA-delivery model in *E. coli* cells (Fig. 4C). Cross-links were also identified between ribosomal protein uS10 and RNAP, NusG, and NusA and support structural models of coupled RNAP-ribosome complexes presented here and previously (Fig. 4C and fig. S9) (*27*, *38*). These cross-links are, however, also consistent with models of transcription antitermination complexes, which may contain uS10 serving in its alternative role as transcription factor NusE (*42*). Analysis of the accessible interaction surface that is based on distance constraints provided by in-cell CLMS reveals that RNAP can occupy at least two positions relative to the ribosome in *E. coli* cells. These two positions are consistent with those we observed by cryo-EM of reconstituted complexes (Fig. 4D).

Conclusions

Our data reveal several roles of bS1 in translation initiation that are consistent with its contribution to translation of most *E. coli* mRNAs (*1*) (fig. S10). First, bS1 likely makes the initial contact between 30*S* and released mRNAs or with RNAP and nascent mRNAs (Fig. 4B and fig. S6A). The modular architecture of bS1 supports an effective search of the space around the 30*S*. The 30*S*-TEC$_{dlv}$ structure suggests that bS1 can bind incoming mRNA before SD-aSD pairing. This initial 30*S*-mRNA complex can be produced without the involvement of IFs, as suggested by biochemical data (*14*) and theoretical considerations (*15*). The 30*S*-TEC$_{dlv}$ structure shows that bS1 can funnel mRNA from the ribosome outer surface to the aSD within the mRNA exit channel, further stabilizing the interaction of the ribosome with mRNAs that contain a SD. The proximity of bS1 to bS21 and the aSD motif thereby supports SD-aSD duplex formation (Fig. 2).

Second, bS1 promotes unwinding of mRNA secondary structures inhibitory to 30*S* binding and mRNA accommodation (*16*, *18*, *43*). bS1 provides an extended basic surface (Fig. 2) to capture and stabilize single-stranded mRNA conformations important for its unwinding activity (*18*). mRNAs with strong SD motifs tend to harbor structured ribosome-binding sites (*44*). The bS1 proximity to the SD-aSD duplex explains why mRNA structure does not impede translation initiation. Finally, our structures reveal that bS1 may couple mRNA delivery to 30*S* activation (Fig. 3 and fig. S10). bS1 stabilizes an inactive 30*S* conformation, and contact with mRNA is expected to shift the 30*S* conformational equilibrium toward folding of the decoding center. However, the contribution of this "bS1-clasped" inactive 30*S* state to the translation initiation pathway in vivo remains to be determined. We propose that competition between bS1 binding to mRNA or bS1 binding to h44 causes mRNA delivery to shift the equilibrium to active 30*S*.

Our data show that an alternative pathway of transcription-assisted mRNA recruitment may also occur that is independent of bS1 (fig. S10). Coupling of the TEC to uS10 by NusG presents the mRNA directly to the mRNA entrance channel and allows SD-aSD duplex formation in the ribosomal A-site of inactive 30*S*. Whether coupling by TEC-bound NusG represents an alternative mRNA delivery route requires further investigation, but this would explain the effect of coupling factors on translation initiation (*6*, *7*).

The architecture of the 30*S*-TEC$_{dlv}$ and 30*S*-TEC$_{exp}$ complexes may change with the length of intervening mRNA between the TEC and the SD. For example, an increased distance between TEC and SD may favor a 30*S*-TEC$_{exp}$ complex with active 30*S* and with a SD-aSD duplex accommodated in the mRNA exit channel. Similarly, for 30*S*-TEC$_{dlv}$, it is also possible that interactions differ for transcripts with weaker SD motifs and lower affinity for bS1.

The formation of a 70*S* translation initiation complex (70*S*-IC) competent to start protein synthesis occurs downstream of the bS1-dependent and NusG-dependent 30*S* recruitment pathways (fig. S10). Addition of the translation IFs IF1, IF2, and IF3 to the samples that we structurally characterized produced 70*S*-IC (fig. S11). This confirms earlier observations (*20*) and supports the interpretation that the complexes we characterized are early in the initiation pathway. Future studies will reveal the precise role of IFs in activating 30*S* and facilitating the transition from 30*S*-TEC$_{dlv}$ or 30*S*-TEC$_{exp}$ to 30*S* translation initiation complexes.

Materials and methods

Materials

For plasmid construction, we used the *E. coli* TOP10 strain (Invitrogen). For recombinant protein expression, we constructed an *E. coli* strain called LACR II (low abundance of cellular RNAses). LACR II is derived from the *E. coli* LOBSTR strain (*45*) with additional RNase deletions to lower the amount of RNAse contamination in purified protein samples.

E. coli strain HMS174 and plasmids to express *E. coli* tRNA^{fMet}, *E. coli* tRNA^{Phe}, and methionyl-tRNA^{fMet} formyltransferase (FMT) were a generous gift from Venki Ramakrishnan. *E. coli* strain SG13009/pREP4 and plasmids to express *E. coli* translation IFs IF1, IF2, and IF3 (PURE_IF1, pQE30_EcIF2, pQE30_EcIF3, respectively) were a generous gift from Venki Ramakrishnan. Plasmids to express *E. coli* RelE (pSC2524HE_Eco_His-RelB_RelE) was a generous gift from Ditlev E. Brodersen.

Plasmid pAX0_(His)$_{10}$-HRV3C-pheS_pheT to express *E. coli* Phenylalanyl-tRNA synthetase (PheRS) was made by amplifying *E. coli pheS* and *pheT* genes with primers 5′- GTTCTGTTTCAGGGTCCGCATATGTCACATCTCGCAGAACTGGTTGC-3′ and 5′-AGTGGTGGTGGTGGTGGTGCTCGAGTCAATCCCTCAATGATGCCTGGAATCG-3′ and insertion into pAX0_(His)$_{10}$_HRV3C at the NdeI and XhoI sites using the SLiCE method (*46*).

Plasmid pAX1_(His)$_{10}$-TwinStrep-HRV3C-rpsA to express *E. coli* small ribosomal subunit protein bS1 was constructed by amplification of the *E. coli rpsA* gene with primers 5′-GTTCTGTTTCAGGGTCCGCATATGACTGAATCTTTTGCTCAACTCTTTG-3′ and 5′-AGTGGTGGTGGTGGTGGTGCTCGAGTTACTCGCCTTTAGCTGCTTTGAAAGC-3′ and insertion into pAX1_(His)$_{10}$_TwinStrep_HRV3C at the NdeI and XhoI sites using the SLiCE method (*46*).

Plasmid pAX1_(His)$_{10}$-TwinStrep-HRV3C-EcMetRS for expression of *E. coli* Methionyl-tRNA synthetase (MetRS) was constructed by amplification of the *E. coli metG* gene with primers 5′- GTTCTGTTTCAGGGTCCGCATATGACTCAAGTCGCGAAGAAAA-3′ and 5′- GTGGTGGTGGTGGTGGTGCTCGAGTTATTTCACCTGATGACCCGGT-3′ and insertion into pAX1_(His)$_{10}$-TwinStrep-HRV3C at the NdeI and XhoI sites using the SLiCE method (*46*).

E. coli *RNAP for cryo-EM*

E. coli RNAP with a C-terminally (His)$_{10}$–tagged β′-subunit was overexpressed in the *E. coli* LACR II strain from pEcrpoABC(-XH)Z co-transformed with pACYC_Duet1_rpoZ to avoid substoichiometric amounts of the RNAP ω-subunit (*47*). RNAP was purified as described before (*48*). For expression, 12 L of LB culture (100 μg/ml ampicillin, 34 μg/ml chloramphenicol) was

induced at an OD_{600} of 0.6 to 0.8 with 0.5 mM IPTG overnight at 18°C. Cells were harvested by centrifugation, resuspended in five volumes of lysis buffer (50 mM Tris-HCl, pH 8.0, 5% glycerol, 1 mM EDTA, 10 μM $ZnCl_2$, 10 mM DTT, 0.1 mM PMSF, 1 mM benzamidine, DNase I, 0.1 mg/50 g cell) and EDTA-free protease inhibitor cocktail (Sigma-Aldrich cOmplete, 1 tablet/50 ml) and lysed by sonication. The lysate was cleared by centrifugation at 40,000*g* for 30 min. RNAP was isolated from the supernatant by polyethyleneimine fractionation followed by ammonium sulfate precipitation as described previously (*49*). The precipitate was resuspended in immobilized metal affinity chromatography (IMAC) binding buffer (20 mM Tris-HCl, pH 8.0, 1 M NaCl, 5% glycerol, 10 μM $ZnCl_2$, 5 mM β-mercaptoethanol, 0.1 mM PMSF, 1 mM benzamidine), loaded on a 20 ml Ni-IMAC Sepharose HP column (Cytiva), and after several washing steps, RNAP was eluted into IMAC elution buffer (IMAC binding buffer containing 250 mM imidazole). Peak fractions were pooled and dialyzed overnight in the presence of His-tagged HRV3C (PreScission) protease (1 mg HRV3C per 8 mg of protein) into dialysis buffer (20 mM Tris-HCl, pH 8.0, 1 M NaCl, 5% glycerol, 5 mM β-mercaptoethanol, 10 μM $ZnCl_2$). Cleaved RNAP was separated from uncleaved RNAP and HRV3C protease by subtractive Ni-IMAC. The sample was then dialyzed into TGE buffer supplemented with $ZnCl_2$ (10 mM Tris-HCl, pH 8.0, 5% glycerol, 0.1 mM EDTA, 10 μM $ZnCl_2$, 1 mM DTT, 0.1 mM PMSF, 1 mM benzamidine) until the conductivity was ≤ 0 mS/cm. RNAP was then loaded on a 50-ml Bio-Rex 70 column (Bio-Rad) equilibrated with Bio-Rex buffer (10 mM Tris-HCl, pH 8.0, 5% glycerol, 0.1 mM EDTA, 0.1 M NaCl, 10 μM $ZnCl_2$, 1 mM DTT, 0.1 mM PMSF, 1 mM benzamidine) and was eluted using a linear gradient over 5 column volumes into Bio-Rex buffer containing 1 M NaCl. The peak was concentrated and further purified by size-exclusion chromatography using a HiLoad Superdex 200 PG 26/600 column (Cytiva) equilibrated with GF buffer (10 mM HEPES, pH 8.0, 0.5 M KCl, 1% glycerol, 10 μM $ZnCl_2$, 1 mM $MgCl_2$, 2 mM DTT, 0.1 mM PMSF, 1 mM benzamidine). The final protein was dialyzed into storage buffer (10 mM HEPES, pH 8.0, 150 mM KOAc, 5 mM $Mg(OAc)_2$, 10 μM $ZnCl_2$, 2 mM DTT) and concentrated, and then aliquots were flash frozen and stored at −80°C.

E. coli *NusG for cryo-EM*

E. coli NusG with an N-terminal $(His)_6$-tag was overexpressed in *E. coli* LACR II strain from pSKB2_$(His)_6$-HRV3C-NusG. For expression, 6 liters of LB culture (50 μg/ml kanamycin) was induced at an OD_{600} of 0.6 with 0.5 mM IPTG for 3 hours at 37°C. Cells were harvested by centrifugation, resuspended in 4 volumes of lysis buffer (50 mM Tris-HCl pH 8.0, 2 mM EDTA, 233 mM NaCl, 5% glycerol, 5 mM β-mercaptoethanol, 0.1 mM PMSF, 1 mM benzamidine, EDTA-free protease inhibitor cocktail; Sigma-Aldrich cOmplete, 1 tablet/50 ml) and lysed by sonication. The lysate was cleared by centrifugation at 40,000 g for 30 min at 4°C. The nucleic acids and their interacting proteins were precipitated by adding 0.6% of polyethyleneimine and removed by centrifugation at 20,000*g* for 20 min at 4°C. $(NH_4)_2SO_4$ was added to the supernatant to a final concentration of 0.37 g/ml, and the precipitate was collected by centrifugation at 40,000*g* for 30 min at 4°C. The pellet was resuspended in IMAC binding buffer (50 mM Tris-HCl, pH 8.0, 0.5 M NaCl, 5 mM imidazole, 1 mM β-mercaptoethanol, 0.1 mM PMSF, 1 mM benzamidine) and loaded on a 5-ml HiTrap IMAC HP column (Cytiva). After several washing steps, NusG was eluted at 60% of IMAC elution buffer (IMAC binding buffer containing 500 mM imidazole). Peak fractions were pooled and dialyzed overnight in the presence of His-tagged HRV3C (PreScission) protease (1 mg HRV3C per 18 mg of protein) into dialysis buffer (50 mM Tris-HCl, pH 8.0, 0.5 M NaCl, 5% glycerol, 1 mM β-mercaptoethanol). Cleaved NusG was separated from uncleaved NusG and HRV3C protease by subtractive Ni-IMAC. Cleaved NusG binds weakly to the IMAC column and was eluted at ~ 60 mM imidazole. The sample was then dialyzed into GF buffer (50 mM Tris-HCl, pH 8.0, 0.5 M NaCl, 5% glycerol, 1 mM DTT, 0.1 mM PMSF, 1 mM benzamidine) and loaded on Superdex 75 16/600 column (Cytiva). The final protein was concentrated, glycerol concentration was set to 15%, and aliquots were flash frozen and stored at −80°C.

E. coli *ribosomal 30S and 50S subunit purification for cryo-EM and biochemical assays*

Ribosomal subunits were purified from *E. coli* strain LACR II following standard procedures (*50*, *51*). The complete purification was done at 0-4°C and all buffers contained 1 mM DTT, 1 mM benzamidine and 0.1 mM PMSF added just before use. Briefly, *E. coli* LACR II cells were grown at 37°C in LB until they reached an OD_{600} of 1.3. The harvested cells were resuspended in 10 ml/g cell paste of buffer A (20 mM Tris-HCl, pH 7.5, 10.5 mM $Mg(OAc)_2$, 100 mM NH_4Cl, 0.5 mM EDTA, DNase I (0.4 mg/50 g cell), protease inhibitor cocktail (Sigma-Aldrich cOmplete, 1 tablet/50 ml), lysed by sonication, and the cell lysate was centrifuged in a Beckman Type 45 Ti rotor for 1 hour at 70,400*g* followed by a second centrifugation of the supernatant in the same rotor for 1 hour at 125,000*g*. The clear, top part of the supernatant was carefully taken, filtered through a 0.22 μm membrane and layered on 25 ml sucrose cushion (20 mM Tris-HCl, pH 7.5, 1.1 M sucrose, 0.5 M NH_4Cl, 10.5 mM $Mg(OAc)_2$, 0.5 mM EDTA) in 45 Ti tubes (40 ml supernatant on 25 ml cushion/tube). The ribosomes were sedimented overnight at 113,000*g* for 20-22 hours. The pellet was washed and resuspended in buffer C (20 mM Tris-HCl, pH 7.5, 0.5 M NH_4Cl, 10.5 mM $Mg(OAc)_2$, 0.5 mM EDTA) and sedimented through an additional sucrose cushion. To isolate tightly coupled 70*S* ribosomes and to remove excess 50S and 30*S* subunits the pellet was washed and resuspended in buffer D (20 mM Tris-HCl, pH 7.5, 60 mM NH_4Cl, 6 mM $Mg(OAc)_2$, 0.25 mM EDTA) and loaded on 15–30% sucrose gradient. This gradient was centrifuged in an SW32 rotor at 44,300*g* for 18 hours. The gradient was fractionated and the peak containing 70*S* ribosomes were collected avoiding any contamination by 50S subunits. The pooled fractions were concentrated and dialyzed into dissociation buffer (20 mM K-HEPES, pH 7.5, 200 mM NH_4Cl, 1 mM $Mg(OAc)_2$). The sample was loaded on 15–30% sucrose gradient that was centrifuged in SW32 rotor at 44,300*g* for 19 hours to separate 30*S* and 50S subunits. After the run, the gradient was fractionated, 30*S* and 50S peak fractions were collected, concentrated, dialyzed into storage buffer (20 mM K-HEPES, pH 7.5, 120 mM KOAc, 10 mM NH_4Cl, 10 mM $Mg(OAc)_2$, 10 μM $ZnCl_2$), flash frozen, and stored as small aliquots at −80°C.

E. coli *small ribosomal subunit protein bS1 for cryo-EM*

E. coli bS1 containing N-terminal $(His)_{10}$_Twin-Strep-tag was overexpressed from pAX1_$(His)_{10}$-TwinStrep-HRV3C-rpsA in the *E. coli* LACR II strain. For expression, 6 L of LB culture (50 μg/ml kanamycin) was induced at an OD_{600} of 0.6-0.8 with 1 mM IPTG for 3 hours at 37°C. Cells were harvested by centrifugation, resuspended in 3 volumes of lysis buffer (20 mM Tris-HCl, pH 7.5, 150 mM NH_4Cl, 500 mM KCl, 5% glycerol, 0.1 mM PMSF, 1 mM benzamidine, 2 mM β-mercaptoethanol, EDTA-free protease inhibitor cocktail (Sigma-Aldrich cOmplete, 1 tablet/50ml)) and lysed using sonication. The lysate was cleared using a Type 45 Ti rotor (Beckman) at 125,000*g* for 30 min. After increasing the NH_4Cl concentration of the supernatant to 1 M to dissociate bS1 from 70*S* ribosomes the sample was centrifuged in a Type 70 Ti rotor (Beckman) at 265,000*g* for 2 hours. The supernatant (containing bS1) was loaded on a 5 ml Ni-HiTrap HP column (Cytiva) equilibrated with IMAC buffer A (20 mM Tris-HCl, pH 7.5, 1 M NH_4Cl, 500 mM KCl, 5% glycerol, 0.1 mM PMSF, 1 mM benzamidine, 2 mM β-mercaptoethanol) and after extensive washing with 2% followed by 10% IMAC buffer B (same as IMAC buffer A but 250 mM imidazole), the protein was eluted with 100% IMAC buffer B. Peak fractions containing bS1 were directly loaded on a 5 ml StrepTrap HP column (Cytiva) equilibrated with Strep binding buffer (20 mM Tris-HCl, pH 7.5, 40 mM NH_4Cl, 150 mM KCl, 5% glycerol, 0.1 mM PMSF, 1 mM benzamidine, 2 mM β-mercaptoethanol) and

the protein was eluted with Strep elution buffer (20 mM Tris-HCl, pH 7.5, 40 mM NH_4Cl, 5% glycerol, 0.1 mM PMSF, 1 mM benzamidine, 2 mM β-mercaptoethanol, 5 mM D-Desthiobiotin). The peak fractions were directly loaded on 5 ml HiTrap Q HP column (Cytiva) equilibrated with Q buffer A (20 mM Tris-HCl, pH 7.5, 40 mM NH_4Cl, 5% glycerol, 0.1 mM PMSF, 1 mM benzamidine, 2 mM β-mercaptoethanol) and eluted using a linear gradient of 0-100% Q buffer B (20 mM Tris-HCl, pH 7.5, 40 mM NH_4Cl, 1 M KCl, 5% glycerol, 0.1 mM PMSF, 1 mM benzamidine, 2 mM β-mercaptoethanol) over 20 column volumes. The sample was dialyzed overnight in the presence of His-tagged HRV3C (PreScission) protease (1 mg HRV3C per 8 mg of protein) into dialysis buffer (20 mM Tris-HCl, pH 7.5, 1 M NH_4Cl, 500 mM KCl, 5% glycerol, 2 mM β-mercaptoethanol). Uncleaved protein, the cleaved $(His)_{10}$-TwinStrep-tag and HRV3C were selectively removed using the IMAC column; because cleaved bS1 weakly binds to the IMAC column it was eluted with 12% IMAC buffer B. The peak was concentrated and dialyzed into assembly buffer (5 mM HEPES, pH 7.5, 100 mM KOAc, 10 mM $Mg(OAc)_2$, 1 mM DTT). The final protein was concentrated and aliquots were flash frozen and stored at −20°C.

For RNAP-bS1 complex binding assay the HRV3C (PreScission) protease cleavage and the subsequent subtractive IMAC steps were skipped to get $(His)_{10}$_TwinStrep-tagged bS1 (HS-bS1).

E. coli *Methionyl-tRNA synthetase (MetRS)*

E. coli MetRS with an N-terminal $(His)_{10}$-TwinStrep-tag was overexpressed from pAX1_$(His)_{10}$-TwinStrep-HRV3C-metRS in the *E. coli* LACR II strain. For expression, 6 L of LB culture (50 μg/ml knamycin) were induced at an OD_{600} of 0.6 to 0.8 with 1 mM IPTG for 3 hours at 37°C. Cells were harvested by centrifugation, resuspended in 5 volumes of lysis buffer (50 mM HEPES, pH 7.5, 0.5 M KCl, 10 mM $MgCl_2$, 0.1 mM PMSF, 1 mM benzamidine, 7 mM β-mercaptoethanol, DNase I (0.5 mg/250 g cell), EDTA-free protease inhibitor cocktail (Sigma-Aldrich cOmplete, 1 tablet/50 ml)) and lysed using sonication. The lysate was cleared by centrifugation at 40,000*g* for 30 min. The supernatant was loaded on a 5-ml Ni-HiTrap HP column (Cytiva) equilibrated with IMAC buffer A (50 mM HEPES, pH 7.5, 0.5 M KCl, 10 mM $MgCl_2$, 0.1 mM PMSF, 1 mM benzamidine, 7 mM β-mercaptoethanol) and after extensive washing with Buffer A followed by 8% IMAC buffer B (same as IMAC buffer A but 250 mM imidazole) the protein was eluted with 100% IMAC buffer B. Peak fractions containing MetRS were directly loaded on a 5 ml StrepTrap HP column (Cytiva) equilibrated with IMAC buffer A and the protein was eluted with Strep elution buffer (same as IMAC buffer A containing 2.5 mM D-Desthiobiotin). Peak fractions were pooled, and cleaved overnight by His-tagged HRV3C (PreScission) protease (1 mg HRV3C per 20 mg of protein). Uncleaved protein, the cleaved $(His)_{10}$-TwinStrep-tag and HRV3C were selectively removed using the IMAC column and collecting the flow-through containing cleaved MetRS. The sample was dialyzed into storage buffer (50 mM HEPES, pH 7.5, 100 mM KOAc, 10 mM $Mg(OAc)_2$, 0.1 mM PMSF, 1 mM benzamidine, 2 mM DTT). The final protein was concentrated and aliquots were flash frozen and stored at −80°C.

Methionyl tRNA^{fMet} formyl transferase (FMT)

E. coli FMT with an N-terminal $(His)_6$-tag was overexpressed from pURE_EcFmt plasmid (*52*) in the *E. coli* LACR II strain. For expression, 6 L of LB culture (100 μg/ml Ampicillin) were induced at an OD_{600} of 0.6-0.8 with 0.1 mM IPTG for 3 hours at 37°C. Cells were harvested by centrifugation, resuspended in 5 volumes of IMAC buffer A (50 mM HEPES, pH 7.5, 0.5 M KCl, 10 mM $MgCl_2$, 10 mM imidazole, 0.1 mM PMSF, 1 mM benzamidine, 7 mM β-mercaptoethanol, DNase I (0.5 mg/250 g cell), EDTA-free protease inhibitor cocktail (Sigma-Aldrich cOmplete, 1 tablet/50 ml)) and lysed using sonication. The lysate was cleared by centrifugation at 40,000*g* for 30 min. The supernatant was loaded on a 5 ml Ni-HiTrap HP column (Cytiva) equilibrated with IMAC buffer A and after extensive washing with Buffer A followed by 8% IMAC buffer B (same as IMAC buffer A but 250 mM imidazole) the protein was eluted with 100% IMAC buffer B. Peak fractions were pooled, and the sample was dialyzed into storage buffer (50 mM HEPES, pH 7.5, 100 mM KOAc, 10 mM $Mg(OAc)_2$, 0.1 mM PMSF, 1 mM benzamidine, 1 mM DTT). The final protein was concentrated and aliquots were flash frozen and stored at −80°C.

E. coli *phenylalanyl-tRNA synthetase (PheRS)*

E. coli PheRS with an N-terminally $(His)_{10}$-tagged α-subunit was overexpressed from pAX0_$(His)_{10}$-HRV3C-pheS_pheT in the *E. coli* LACR II strain. For expression, 6 L of LB culture (50 μg/ml kanamycin) were induced at an OD_{600} of 0.6-0.8 with 0.5 mM IPTG for 3 hours at 37°C. Cells were harvested by centrifugation, resuspended in 5 volumes of lysis buffer (50 mM HEPES-KOH pH 7.5, 1 M NH_4Cl, 10 mM $MgCl_2$, 0.1 mM PMSF, 1 mM benzamidine, 2 mM β-mercaptoethanol, DNase I (0.5 mg/250 g cell), EDTA-free protease inhibitor cocktail (Sigma-Aldrich cOmplete, 1 tablet/50 ml)) and lysed using sonication. The lysate was cleared using a Type 45 Ti rotor (Beckman) at 185,000*g* for 1 hour. The supernatant was loaded on a 5 ml Ni-HiTrap HP column (Cytiva) equilibrated with IMAC buffer A (50 mM HEPES-KOH pH 7.5, 1 M NH_4Cl, 10 mM $MgCl_2$, 10 mM imidazole, 0.1 mM PMSF, 1 mM benzamidine, 2 mM β-mercaptoethanol) and after extensive washing with Buffer A followed by 5% IMAC buffer B (same as IMAC buffer A but 400 mM imidazole) the protein was eluted using a linear gradient of 5-100% IMAC buffer B. Peak fractions were pooled, and dialyzed overnight in the presence of His-tagged HRV3C (PreScission) protease (1 mg HRV3C per 8 mg of protein) into dialysis buffer (50 mM HEPES-KOH pH 7.5, 1 M NH_4Cl, 10 mM $MgCl_2$, 2 mM β-mercaptoethanol). Uncleaved protein, the cleaved $(His)_{10}$-tag and HRV3C were selectively removed using the IMAC column and collecting the flowthrough containing cleaved PheRS. The sample was dialyzed into Q binding buffer (10 mM HEPES-KOH pH 7.5, 50 mM NaCl, 1 mM DTT, 0.1 mM PMSF, 1 mM benzamidine) until the conductivity was ≤ 6mS/cm. PheRS was loaded on two 5 ml HiTrap Q columns (Cytiva) equilibrated in Q binding buffer and eluted using a linear gradient into Q binding buffer containing 1 M NaCl over 10 column volumes. The peak fractions were concentrated and dialyzed into storage buffer (50 mM HEPES-KOH pH 7.5, 100 mM NaCl, 2 mM DTT). The final protein was concentrated to ~50 mg/ml, equal volume of 100% glycerol was added, and aliquots were flash frozen and stored at −20°C.

tRNA purification and aminoacylation

Total tRNA extraction: The tRNAs were expressed, purified and aminoacylated as was previously described (*53*, *54*). *E. coli* HMS174 cells overexpressing tRNA^{fMet} or tRNA^{Phe} were grown in LB (100 μg/ml Ampicillin) for 24 hours at 37°C. Cells were harvested by centrifugation and resuspended in 10 ml lysis buffer per liter of culture (10 mM Tris-HCl pH 7.5, 10 mM Mg$(OAc)_2$). An equal volume of phenol pH 4.3 was added to the sample and vortexed twice for 30 s. The aqueous phase was separated from the organic phase by centrifugation at 27,000*g*, 20°C for 30 min and was ethanol precipitated by addition of 3 volumes of ethanol. After one hour of incubation at −20°C the sample was centrifuged at 8600*g*, 4°C for 30 min. To separate high molecular weight nucleic acids, the pellet was resuspended in 50 ml 1 M NaCl by vortexing and rolling at room temperature and was cleared by centrifugation at 8600*g*, 4°C for 5 min. 3 volumes of ethanol were added to the supernatant and stored overnight at −20°C to precipitate tRNA. After centrifugation at 8600*g*, 4°C for 20 min, the pellet was resuspended in 25 ml 1.5 M Tris-HCl pH 8.8 and was incubated in a water bath at 37°C for 2 hours to deacylate tRNAs. The total tRNA was ethanol precipitated by addition of 3 volumes of ethanol.

E. coli tRNA^{fMet} purification: The total tRNA pellet was resuspended in Q-sepharose A buffer (20 mM Tris-HCl pH 7.5, 8 mM $MgCl_2$, 200 mM NaCl, 0.1 mM EDTA). The sample was filtered through a 0.22 μm membrane and loaded on a 5 ml HiTrap Q FF column (Cytiva) and was eluted using a linear gradient 0-60% into Q-sepharose B buffer (same as buffer A with 1 M NaCl) over

20 column volumes. Peak fractions corresponding to 37-47 mS/cm conductivity were pooled and dialyzed into aminoacylation reaction buffer (20 mM Tris-HCl pH 7.5, 7 mM $MgCl_2$, 150 mM KCl).

$tRNA^{fMet}$ aminoacylation: 20 μM $tRNA^{fMet}$, 200 μM L-methionine, 4 mM ATP, 1 μM MetRS, and 2 U/ml pyrophosphatase (Sigma-Aldrich) were mixed in aminoacylation reaction buffer and incubated for 30 min at 37°C.

Met-$tRNA^{fMet}$ formylation: Formyl donor and formyl transferase were added to the aminoacylated tRNA at a final concentration of 250 μM and 5 μM, respectively, and the sample was incubated for 30 min at 37°C. The reaction was stopped by ethanol precipitation (0.1 volume 3M NaOAc, 2.5 volume ice cold ethanol). The pellet was resuspended in 5PW A buffer and loaded on a Phenyl-5PW column (see next section).

The formyl donor (N^5-N^{10}-methenyltetrahydrofolic acid) was prepared by dissolving 100 mg folinic acid calcium salt in 8 ml 50 mM β-mercaptoethanol, adding 880 μl 1M HCl and incubating at RT for 3 hours. It was aliquoted and stored at −80°C. Before use, 100 μl formyl donor was neutralized by addition of 10 μl 1M Tris-HCl, pH 8.0 ,and 10 μl 1 M KOH and incubation at RT for 20 min.

fMet-$tRNA^{fMet}$ purification: After aminoacylation and formylation (see previous section), fMet-$tRNA^{fMet}$ was purified on 54 ml TSKgel® Phenyl-5PW column (Tosoh Bioscience) equilibrated wit 5PW buffer A [10 mM NH_4OAc pH 6.3, 1.7 M $(NH_4)_2SO_4$]. tRNAs were eluted using a linear gradient of 10-35% 5PW buffer B (10 mM NH_4Oac, pH 6.3) for 4 column volumes. Peak fractions with conductivity between 168-157 mS/cm were pooled and dialyzed into tRNA storage buffer (10 mM NH_4OAc pH 4.5, 50 mM KCl). fMet-$tRNA^{fMet}$ was concentrated and aliquots were flash frozen and stored in liquid nitrogen.

E. coli $tRNA^{Phe}$ purification: The ethanol precipitated total tRNA pellet was resuspended in Phe-sepharose A buffer [20 mM NaOAc pH 5.3, 10 mM $MgCl_2$, 1.5 M $(NH_4)_2SO_4$] and was loaded on a 50 ml phenyl Sepharose column (Cytiva). After one column volume wash step the tRNAs were eluted with a linear gradient of Phe-sepharose B buffer (20 mM NaOAc pH 5.3, 10 mM $MgCl_2$) 0-60% for 2.3 column volumes, followed by 0.5 column volumes at 60% and 2 column volumes at 100%. Peak fractions with conductivity between 145-110 mS/cm were pooled, the $(NH_4)_2SO_4$ concentration was adjusted to ≥ 1.7 M, and the sample was loaded on 54 ml TSKgel® Phenyl-5PW column (Tosoh Bioscience) equilibrated with 5PW buffer A (10 mM NH_4OAc pH 6.3, 1.7 M $(NH_4)_2SO_4$). tRNAs were eluted using a linear gradient of 10-35% 5PW buffer B (10 mM NH_4OAc pH 6.3) for 4 column volumes. Peak fractions with conductivity between 176-181 mS/cm were pooled and dialyzed into aminoacylation reaction buffer.

$tRNA^{Phe}$ aminoacylation: 20 μM $tRNA^{Phe}$, 200 μM phenylalanine, 4 mM ATP, 0.2 μM PheRS, and 2 U/ml pyrophosphatase (Sigma-Aldrich) were mixed in reaction buffer (20 mM Tris-HCl pH 7.5, 7 mM $MgCl_2$, 150 mM KCl) and incubated for 30 min at 37°C. The sample was precipitated by addition of three volumes of ethanol. The pellet was resuspended in 5PW A buffer and loaded on a Phenyl-5PW column (see next section).

Phe-$tRNA^{Phe}$ purification: After aminoacylation (see previous section), Phe-$tRNA^{Phe}$ was separated from $tRNA^{Phe}$ on a Phenyl-5PW column (see $tRNA^{Phe}$ purification) Peak fractions were pooled and dialyzed into tRNA storage buffer. Phe-$tRNA^{Phe}$ was concentrated and aliquots were flash frozen and stored at −80°C.

E. coli *translation initiation factors IF-1 and IF-3*

E. coli IF1 or IF3 containing an N-terminal $(His)_6$-tag was overexpressed from PURE_IF1, or pQE30_IF3, respectively, in the *E. coli* SG13009/pREP4 strain. For expression of both, 6 L of LB culture (100 μg/ml Ampicillin, 50 μg/ml kanamycin) was induced at an OD_{600} of 0.6-0.8 with 1 mM IPTG for 3 hours at 37°C. Cells were harvested by centrifugation, resuspended in 3 volumes of lysis buffer (50 mM HEPES-KOH pH 7.5, 1 M NH_4Cl, 10 mM $MgCl_2$, 0.2 mM PMSF, 1 mM benzamidine, 7 mM β-mercaptoethanol, EDTA-free protease inhibitor cocktail (Sigma-Aldrich cOmplete, 1 tablet/50ml), DNase I (0.1 mg/50 g cell)) and lysed using sonication. The lysate was cleared using a Type 45 Ti rotor (Beckman) at 125,000*g* for 30 min. The supernatant was loaded on a 5 ml Ni-HiTrap HP column (Cytiva) equilibrated with IMAC buffer A (50 mM HEPES-KOH pH 7.5, 1 M NH_4Cl, 10 mM $MgCl_2$, 10 mM imidazole, 0.2 mM PMSF, 1 mM benzamidine, 7 mM β-mercaptoethanol) and the protein was eluted with a 0-100% gradient with IMAC buffer B (same as IMAC buffer A but 400 mM imidazole). Peak fractions containing IF1 or IF3 were dialyzed overnight into storage buffer (50 mM HEPES-KOH pH 7.5, 1 M NH_4Cl, 10 mM $MgCl_2$, 30% glycerol, 0.2 mM PMSF, 1 mM benzamidine, 2 mM DTT). The final protein was concentrated and aliquots were flash frozen and stored at −80°C.

E. coli *translation initiation factor IF-2*

E. coli IF2 containing an N-terminal $(His)_6$-tag was overexpressed from pQE30_IF2 plasmid in the *E. coli* SG13009/pREP4 strain. For expression, 6 L of LB culture (100 μg/ml Ampicillin, 50 μg/ml kanamycin) was induced at an OD_{600} of 0.6-0.8 with 1 mM IPTG for 3 hours at 37°C. Cells were harvested by centrifugation, resuspended in 3 volumes of lysis buffer (50 mM HEPES-KOH pH 7.5, 1 M NH_4Cl, 10 mM $MgCl_2$, 0.2 mM PMSF, 1 mM benzamidine, 7 mM β-mercaptoethanol, EDTA-free protease inhibitor cocktail (Sigma-Aldrich cOmplete, 1 tablet/50ml), DNase I (0.1 mg/50 g cell)) and lysed using sonication. The lysate was cleared using a Type 45 Ti rotor (Beckman) at 125,000*g* for 30 min. The supernatant was loaded on a 5 ml Ni-HiTrap HP column (Cytiva) equilibrated with IMAC buffer A (50 mM HEPES-KOH pH 7.5, 1 M NH_4Cl, 10 mM imidazole, 0.2 mM PMSF, 1 mM benzamidine, 7 mM β-mercaptoethanol, 2 mM DTT) and was eluted with a 0-100% gradient with IMAC buffer B (same as IMAC buffer A but 400 mM imidazole). The sample was then dialyzed into HIC buffer B (50 mM HEPES-KOH pH 7.5, 500 mM NaCl, 0.2 mM PMSF, 1 mM benzamidine, 1 mM DTT). After dialyses an equal volume of HIC buffer B + 2 M $(NH_4)_2SO_4$ was added to reach a final concentration of 1 M $(NH_4)_2SO_4$. IF2 was then loaded on a 10 ml butyl-sepharose high performance column (Cytiva) equilibrated with HIC buffer A (50 mM HEPES-KOH pH 7.5, 500 mM NaCl, 1 M $(NH_4)_2SO_4$, 0.2 mM PMSF, 1 mM benzamidine, 1 mM DTT) and was eluted using a linear gradient over 20 column volumes into HIC buffer B. The peak was concentrated and further purified by size-exclusion chromatography using a HiLoad Superdex 200 PG 16/600 column (Cytiva) equilibrated with GF buffer (50 mM HEPES-KOH pH 7.5, 1 M NH_4Cl, 10 mM $MgCl_2$, 0.2 mM PMSF, 1 mM benzamidine, 1 mM DTT). Peak fractions containing IF2 were dialyzed overnight into storage buffer (50 mM HEPES-KOH pH 7.5, 1 M NH_4Cl, 10 mM $MgCl_2$, 30% glycerol, 0.2 mM PMSF, 1 mM benzamidine, 2 mM DTT). The final protein was concentrated and aliquots were flash frozen and stored at −80°C.

EF-G and EF-Tu purification for RelE cleavage assay

E. coli EF-G and EF-Tu with a cleavable N-terminal $(His)_{10}$-TwinStrep-tag were overexpressed in the *E. coli* LACR II strain from pAX1_10His-TwinStrep-HRV3C-EcoEF-G and pAX1_10His-TwinStrep-HRV3C-EcoEF-Tu. For expression, 6 L of LB culture (50 μg/ml kanamycin) was induced at an OD_{600} of 0.6 with 0.1 mM IPTG for 4 hours at 37°C. Cells were harvested by centrifugation, resuspended in 4 volumes of lysis buffer (50 mM HEPES-KOH pH 7.6, 1 M NH4Cl, 10 mM $MgCl_2$, 0.1% Triton X100, 7 mM β-mercaptoethanol, 0.1 mM PMSF, 1 mM benzamidine, EDTA-free protease inhibitor cocktail (Sigma-Aldrich cOmplete, 1 tablet/50 ml)) and lysed by sonication. The lysate was cleared using a Type 45 Ti rotor (Beckman) at 125,000*g* for 30 min at 4°C. The filtered supernatants were loaded on a 5 ml Ni-HiTrap HP column (Cytiva) equilibrated with IMAC buffer A (50 mM HEPES-KOH pH 7.6, 1 M NH4Cl, 10 mM $MgCl_2$, 7 mM β-mercaptoethanol, 0.1 mM PMSF, 1 mM benzamidine) and after extensive washing with 2% followed by 10% IMAC buffer B (same as IMAC buffer A except 250 mM imidazole), the protein was eluted with 100% IMAC buffer B. Peak fractions containing EF-G or EF-Tu were directly loaded on a 5 ml StrepTrap

HP column (Cytiva) equilibrated with Strep binding buffer (50 mM HEPES-KOH pH 7.5, 0.5M KCl, 10 mM $MgCl_2$, 7 mM β-mercaptoethanol, 0.1 mM PMSF, 1 mM benzamidine) and the proteins were eluted with Strep elution buffer (50 mM HEPES-KOH pH 7.5, 0.5 M KCl, 10 mM $MgCl_2$, 7 mM β-mercaptoethanol, 5mM D-desthiobiotin, 0.1 mM PMSF, 1 mM benzamidine). The samples were incubated with His-tagged HRV3C (PreScission) protease (1 mg HRV3C per 25 mg of protein) for 30 min at 4°C. Uncleaved proteins, the cleaved $(His)_{10}$-TwinStrep-tag and HRV3C were selectively removed using the IMAC column. In contrast to cleaved EF-G, cleaved EF-Tu weakly binds the IMAC column and was eluted with 20% IMAC buffer B. The EF-G flow-through or EF-Tu peak fractions were dialyzed into storage buffer (50 mM HEPES-KOH, pH 7.5, 100 mM KCl, 10 mM $MgCl_2$, 30% glycerol, 7 mM β-mercaptoethanol, 0.1 mM PMSF, 1 mM benzamidine). The purified proteins were concentrated to 10 mg/ml and aliquots were flash frozen and stored at −80°C.

RelE purification for RelE cleavage assay

E. coli RelE was overexpressed in a complex with RelB in the *E. coli* LACR II strain from pSC2524HE_Eco_His-RelB_RelE. For expression, 6 L of LB culture (10 μg/ml Ampicillin) was induced at an OD_{600} of 0.6 with 0.2 mM IPTG for 4 hours at 37°C. Cells were harvested by centrifugation and resuspended in 10 volumes of lysis buffer (50 mM Tris, pH 8.0, 0.3 M NaCl, 5 mM $MgCl_2$, 0.1 mM PMSF, 1 mM benzamidine and 5 mM β-mercaptoethanol). EDTA-free protease inhibitor cocktail (Sigma-Aldrich cOmplete, 1 tablet/50 ml) was added and cells were lysed by sonication. The lysate was cleared using a Type 45 Ti rotor (Beckman) at 125,000*g* for 30 min at 4°C and the filtered supernatant was loaded on a 5 ml Ni-HiTrap HP column (Cytiva). After washing the column with lysis buffer containing 15 mM imidazole, RelE was eluted from immobilized RelB using on-column denaturation (50 mM Tris-HCl, pH 8, 0.3 M NaCl, 9 M urea, and 5 mM β-mercaptoethanol) at 20°C. The fractions containing pure RelE were refolded by dialysis overnight into storage buffer (20 mM HEPES-KOH, pH 7.5, 120mM KCl, 10 mM NH4Cl, 1mM DTT). The final protein was concentrated to 10 mg/ml and aliquots were flash frozen and stored at −80°C.

Oligonucleotide scaffold preparation for cryo-EM

DNA (Sigma-Aldrich) and RNA (Dharmacon, IDT) oligonucleotides were chemically synthesized and purified by the manufacturer. Both DNA and RNA were dissolved in RNase free water and aliquots were stored at −80°C.

For nucleic acid scaffold assembly, tDNA and mRNA were mixed in a 1:1 molar ratio in reconstitution buffer (10 mM HEPES, pH 7.0, 40 mM KOAc, 5 mM $Mg(OAc)_2$) and annealed by heating to 95°C followed by stepwise cooling to 10°C in a PCR machine; ntDNA was added during complex formation.

Binding assay for RNAP-bS1 complex

For the binding assays bS1 with an N-terminal $(His)_{10}$-TwinStrep-tag (HS-bS1) was used that enabled the detection of the protein by immunoblotting using a His-tag specific antibody.

Size exclusion chromatography: RNAP, HS-bS1 and RNAP_HS-bS1 samples were incubated in TGED + 0.1 M NaCl buffer (10 mM Tris-HCl, pH 8.0, 5% glycerol, 0.1 mM EDTA, 100 mM NaCl, 1 mM DTT) for 15 min at 37°C. The final concentration of the proteins in the reactions was the following: RNAP 3.3 μM, HS-bS1 6.5 μM. After centrifugation at 21,000*g* for 20 min the entire reaction mixture (300 μl) was injected onto a Superdex 200 Increase 10/300 column (Cytiva) preequilibrated with TGED + 0.1 M NaCl buffer using a 0.5 ml loop. The column was run at 0.4 ml/min flow rate and 0.5 ml fractions were collected. Fractions corresponding to the elution volume of RNAP (fractions A9 to A11, corresponding to 8.36 to 9.86 ml) were separated on Nu-PAGE 4-12% Bis-Tris gel (Invitrogen) before Western blotting. 15 μl sample was loaded per lane.

Western blotting: The transfer of proteins on nitrocellulose membrane was done by the iBlot® Dry Blotting System (Invitrogen). For detecting HS-bS1 a His-tag specific monoclonal mice primary antibody (prepared in house, ref.: HIS-1G4) and polyclonal donkey anti-mouse secondary antibody (Jackson ImmunoResearch) was used. Signal detection was done with SuperSignal West Pico PLUS (Thermo Scientific Pierce) chemiluminescent substrate in Amersham Imager 600 (Cytiva) chemiluminescence imager.

Native polyacrylamide gel electrophoresis

Complexes were assembled by mixing components in assembly buffer (20 mM K-HEPES, pH 7.5, 100 mM KOAc, 10 mM NH_4Cl, 10 mM $Mg(OAc)_2$, 10 μM $ZnCl_2$, 1mM DTT) in 10 μl final volume. First RNAP and, when present, nucleic acid scaffolds (table S2) were incubated for 15 min at 37°C; ntDNA and bS1 were added followed by incubation for 5 min at 37°C after the addition of each component. The final concentration of the components was the following: RNAP 4 μM, nucleic acid scaffold 8 μM, ntDNA 8 μM, bS1 16 μM.

Samples were separated at 100V on 6% polyacrylamide gel at 4°C using Tris-Alanine buffer (125 mM Tris-HCl pH 8.8, 0.44 mM Alanine). 4 μl sample was loaded per lane. The gel was stained with ethidium-bromide followed by Coomassie Blue G-250 staining.

RelE cleavage assay

The TEC was purified on a Superose 6 10/300 gel filtration column (see next section on Cryo-EM sample preparation for details) except chemically synthesized tDNA and ntDNA carried a 5′-mono-phosphate (Eurofins; table S2). After purification, the TEC was incubated with T4 polynucleotide kinase (Thermo Fisher Scientific) and ^{32}P-γ-ATP for 10 min to label nascent RNA-38 and then transferred on ice. All the reactions including TEC labeling were done at 37°C in EM buffer (20 mM HEPES-KOH, pH 7.5, 120 mM KOAc, 10mM NH4Cl, 10 mM $Mg(OAc)_2$, 10μM $ZnCl_2$, 1mM DTT).

To test RNAP activity the labeled TEC (0.5 μM) was incubated with 100 μM of GTP for 1 min. The reaction was stopped by adding an equal volume of loading buffer (8 M urea, 20 mM EDTA pH 8, 5 mM Tris-HCl pH 7.5, 0.5% bromophenol blue, and 0.5% xylene cyanol).

For the RelE cleavage assay the following components were added stepwise to the labeled TEC (0.5 μM): fMet-tRNA^{fMet} (2 μM), 30*S* (1 μM), 50S ribosomal subunits (1 μM), IFs (5 μM of each IF1, IF2 and IF3), Phe-tRNA^{Phe} (2 μM), elongation factors (5 μM of each EF-G and EF-Tu) and GTP (200 μM). After each addition, the reaction was incubated for 5 min and an aliquot was transferred on ice. Each aliquot was incubated with RelE (5 μM) for 10 min at 37°C and reactions were stopped by adding an equal volume of loading buffer. Individual samples were analyzed on a denaturing 20% polyacrylamide gel. For data analysis, gels were exposed to storage phosphor screens and quantified using a Typhoon PhosphorImager and ImageQuant software (Cytiva).

Cryo-EM sample preparation

The TEC was prepared by mixing *E. coli* RNAP (64 μM final) with nucleic acid scaffold (tDNA; RNA-38) in EM buffer (20 mM HEPES-KOH, pH 7.5, 120 mM KOAc, 10mM NH_4Cl, 10 mM $Mg(OAc)_2$, 10μM $ZnCl_2$,) and incubated for 15 min at 37°C. ntDNA was added followed by incubation for 5 min at 37°C. For the TEC, the molar ratio of the components was as follows RNAP:tDNA:RNA-38:ntDNA=1:2:2:2. The TEC was further purified on a Superose 6 10/300 gel filtration column (Cytiva). Peak fractions were collected and concentrated. The 30*S*-RNAP complex was directly assembled by mixing 5 μM of purified TEC with *E. coli* 30*S* subunits and *E. coli* bS1 and incubated for 15 min at 37°C. Next *E. coli* NusG and *E. coli* fMet-tRNA^{fMet} were added to the mixture followed by 5 min incubation at 37°C. The final molar ratio of the components was as follows: 30*S*:bS1:fMet-tRNA^{fMet}:TEC:NusG=1:1:2:1:4. The sample was directly used for cryo-EM grid preparation for structural characterization.

Cryo-EM grid preparation and data collection

Quantifoil R2/2 300 mesh holey carbon copper grids were plasma cleaned on a Model 1070 (Fischione Instruments) for 90 s at 35% power and with an 80% Argon and 20% Oxygen mixture. 8 mM of CHAPSO was added before the

application of 3.5 µl sample to the grid, which was plunge-frozen in liquid ethane using a Vitrobot Mark IV (FEI) with 95% chamber humidity at 10 °C. The grids were imaged using a 300 keV Titan KRIOS (FEI) with a K3 Summit direct electron detector (Gatan) at pixel size of 0.84 Å/px. Movies with 50 frames were collected with a total electron dose of 49.95 $e^-/Å^2$ at a rate of 18.55 e^-/px/sec in counting mode with defocus values in the range −0.8 to −2.0 µm.

Details for grid preparation and data collection of the 70*S* sample have been described previously (*27*).

Cryo-EM data processing

Image frames for all datasets were aligned and corrected for particle motion using MotionCor2 (*55*). Contrast transfer function (CTF) parameters were calculated in CryoSPARC (ver 4.3, 30*S* ribosomal subunit containing samples) using Patch CTF Estimation (*56*) or with Gctf (70*S* ribosome containing sample) (*57*). All subsequent steps were performed using CryoSPARC (30*S* samples) (ver 4.3) (*56*) or RELION-3 (70*S* samples) (*58*). Details for further data processing for the 70*S* ribosome containing sample have previously been described (*27*) and we describe 30*S* sample data processing from here on. Initially, particles were picked using a blob picker from a subset of images and subjected to reference free 2D classification to generate templates. The best 2D classes containing 30*S* subunits were used for reference-based particle picking. After removing particles that poorly aligned or lacked 30*S* subunits by 2D classification, 508,804 particles remained and were used for ab initio reconstructions to obtain an initial reference for several iterative rounds of 3D refinements and classifications (fig. S1C). Downstream processing and classification were done using two distinct approaches (fig. S1D): either, global classification, or focused classification using a mask covering helix 44 (table S4) of the 30*S* subunit was carried out and led to comparable results.

For the global classification, an initial round of reference-based 3D classification was done to remove poorly aligned particles. Further classification yielded two initial sets of particles with additional density in the position of TEC_{dlv} and of TEC_{exp}, containing 172,325 and 193,911 particles respectively. For the 172,325 30*S*-TEC_{dlv} particles, 3D variability analysis using a mask covering TEC_{dlv} and bS1 density was employed using CryoSPARC and separated 121,575 particles corresponding to 30*S*-TEC_{dlv} and 20,551 particles corresponding to the 30*S*-PIC. For the 30*S*-TEC_{dlv} subset, conventional 3D classification was ineffective to confirm the presence of TEC and an alternative approach was adopted. Particles were re-extracted after being recentered on the TEC density and a consensus reconstruction was obtained. The ribosome signal was subtracted on a per-particle basis using a soft mask covering the entire 30*S* subunit (table S4), several rounds of 2D classification were carried out to select particles with strong TEC signal and a reconstruction confirming the presence of the TEC was obtained for 7,284 30*S*-TEC_{dlv} particles. Focused refinements using soft masks covering 30*S* head, body and platform (table S4) improved the local resolution and focused maps were used for model building.

The final reconstruction corresponding to the 30*S*-PIC was obtained by conventional homogeneous 3D refinement. Focused refinements using soft masks covering 30*S* head, body and platform (table S4) improved the local resolution and focused maps were used for model building.

For the NusG-coupled 30*S*-TEC_{exp} subset, conventional 3D classification also failed to separate 30*S* subunits with and without TEC_{exp} and the same approach was used as for 30*S*-TEC_{dlv}. Particles were re-extracted, recentered on the TEC_{exp} density and were subjected to homogeneous refinement. After ribosome signal subtraction using a soft mask covering the entire 30*S* (table S4) and several rounds of 2D classification 47,390 30*S* ribosome particles with a NusG-coupled TEC_{exp} (in a position observed before in a NusG-coupled expressome (*27*)) were identified. The signal subtraction was reversed and homogeneous refinement produced a consensus 30*S*-TEC_{exp} map with weak helix 44 density. 3D variability analysis in CryoSPARC using a mask covering TEC_{exp} (table S4) enabled visualization of TEC_{exp} mobility and independently confirmed the presence of NusG-coupled TEC_{exp} (fig. S3A). Focused classification using a soft mask covering helix 44 (table S4) of the 30*S*-TEC_{exp} ribosome further classified these particles into two classes, 30*S*-TEC_{exp} Inactive state 1 and 30*S*-TEC_{exp} Inactive state 2, having 30,337 and 12,337 particles, respectively.

Alternatively, we directly used focused 3D classification of 508,804 particles using a soft mask covering helix 44 (table S4). This resulted in the initial separation of particles containing additional density in the position of TEC_{dlv} (30*S*-TEC_{dlv}) and of TEC_{exp} (30*S*-TEC_{exp}) with 301,292 and 164,396 particles respectively. For the 30*S*-TEC_{dlv}, particles were subject to focused 3D variability analysis with a soft mask generated in UCSF ChimeraX (*59*, *60*) and covering density for TEC_{dlv} and bS1. This separated 27,560 particles corresponding to the 30*S*-PIC and 256,024 particles corresponding to a consensus 30*S*-TEC_{dlv} complex. Further classification using the same approach separated the 256,024 particles into five classes: 40,511 particles (Subclass 1) contained extra density that appeared to be in a similar position as observed for the global classification. 56,033 particles (Subclass 2) contained extra density partially overlapping with a previously reported RNAP position bound to the 30*S* subunit in absence of mRNA and DNA (Demo *et al.*, 2017). Finally, we identified additional classes with variable bS1 conformations and additional density that corresponds to TEC_{dlv} (Subclass 3, Subclass 4, and Subclass 5, with 51,717 particles, 62,425 particles, and 23,774 particles, respectively).

The 56,033 30*S*-TEC_{dlv} particles (subclass 2) were subjected to recentering on TEC_{dlv} density, re-extraction and subtraction of ribosome signal on a per-particle basis (see above for 30*S*-TEC_{exp}) and resulted in a final subset of 5,463 particles confirming the extra density corresponds to a flexibly tethered TEC_{dlv}.

With this approach we could identify new bS1 conformations bound to 30*S* ribosomes, which we were unable to separate in our first approach. Additionally, focused 3D variability analysis of potential mRNA delivery complexes (256,024 particles) with a soft mask around the 30*S* head domain (table S4) separated particles into homogeneous subsets with open head and closed head conformational states with 112,399 and 52,113 particles, respectively.

For the 30*S*-TEC_{exp}, particles were subject to further focused 3D variability analysis with a soft mask covering helix 44. This separated 97,819 particles corresponding to the 30*S*-TEC_{exp} Inactive state 1 and 66,550 particles corresponding to 30*S*-TEC_{exp} Inactive state 2. 3D variability analysis using a soft spherical mask centered on the mRNA exit channel revealed structural heterogeneity of helix 44 in the exit channel and identified a subset of 11,965 particles with helix 44 bound by bS1 OB2 and OB3.

Masks used for focused classifications, focused 3D variability analysis, or focused refinements were either generated using a molecular model (table S4) followed by mask expansion, and smoothing using ncsmask (*61*) or in ChimeraX by volume segmentation and deletion of regions outside the desired volume. A resolution-dependent soft edge (typically 5*resolution/apix) was added after import in CryoSPARC.

Model building

Initial models for the active and inactive 30*S* ribosome were generated by docking previously published high-resolution structures of the 30*S* and 70*S* ribosome (PDB: 6ZTJ, PDB: 7NAT, PDB: 7K00, PDB: 6W77) (*23*, *27*, *39*, *62*) in UCSF ChimeraX (*59*, *60*) and locally adjusted using Coot (*63*). The same approach was used for the *E. coli* TEC (PDB: 6ZTJ). The deposited AlphaFold prediction for bS1 (AF-P0AG67-F1) was used for modelling of bS1 into the EM density (*64*). The base of h44 was built de novo and peripheral parts were built by rigid body docking fragments followed by local adjustments in Coot. The mRNA was built de novo in Coot. Models were manually adjusted and rebuilt where necessary in Coot and were subject to iterative rounds of real-space refinement

against focused maps using secondary structure restraints and geometry optimization in Phenix (*65*). The accession numbers for the 10 refined models (30*S*-PIC with fMet-tRNA^{fMet} bound to an accommodated mRNA in the P-site and no TEC, 30*S*-TEC$_{exp}$ Inactive state 1 with saturating NusG and TEC$_{exp}$ bound in the expressome position, 30*S*-TEC$_{exp}$ Inactive state 2 with saturating NusG and TEC$_{exp}$ bound in the expressome position, 30*S*-TEC$_{dlv}$ with TEC$_{dlv}$ resolved – 30*S*$_{dlv}$ and TEC$_{dlv}$ deposited separately, mRNA delivery complex 30*S*$_{dlv}$ with bS1 resolved, mRNA delivery complex 30*S*$_{dlv}$ consensus, mRNA delivery complex 30*S*$_{dlv}$ open head, mRNA delivery complex 30*S*$_{dlv}$ closed head, mRNA delivery complex 70*S*-TEC$_{dlv}$) are 9GUQ, 9GUX, 9GUW, 9GUS, 9GUR, 9GUT, 9GUU, 9GUP, 9GUV, 9GR1 (table S1).

The accession numbers for the 10 reported cryo-EM reconstructions, each typically consisting of a composite and consensus map, and if applicable individual focused maps (30*S*-PIC with fMet-tRNA^{fMet} bound to an accommodated mRNA in the P-site and no TEC, 30*S*-TEC$_{exp}$ Inactive state 1 with saturating NusG and TEC$_{exp}$ bound in the expressome position, 30*S*-TEC$_{exp}$ Inactive state 2 with saturating NusG and TEC$_{exp}$ bound in the expressome position, 30*S*-TEC$_{dlv}$ with TEC$_{dlv}$ resolved – 30*S*$_{dlv}$ and TEC$_{dlv}$ deposited separately, mRNA delivery complex 30*S*$_{dlv}$ with bS1 resolved, mRNA delivery complex 30*S*$_{dlv}$ consensus, mRNA delivery complex 30*S*$_{dlv}$ open head, mRNA delivery complex 30*S*$_{dlv}$ closed head, mRNA delivery complex 70*S*-TEC$_{dlv}$) in this paper are EMD-51616, EMD-51602, EMD-51603, EMD-51604, EMD-51623, EMD-51596, EMD-51597, EMD-51598, EMD-51599, EMD-51600, EMD-51622, EMD-51591, EMD-51592, EMD-51593, EMD-51594, EMD-51595, EMD-51618, EMD-51584, EMD-51585, EMD-51586, EMD-51601, EMD-51617, EMD-51619, EMD-51580, EMD-51581, EMD-51582, EMD-51583, EMD-51620, EMD-51576, EMD-51577, EMD-51578, EMD-51579, EMD-51615, EMD-51572, EMD-51573, EMD-51574, EMD-51575, EMD-51621, EMD-51587, EMD-51588, EMD-51589, EMD-51590, EMD-51517 (table S1).

Preparation of fluorescently labeled nascent transcripts for single-molecule colocalization experiments

In vitro transcription reactions were performed in two steps to allow the specific incorporation of Cy3 at the 5′-end of the RNA. Transcription reactions were performed in transcription buffer (20 mM Tris-HCl, pH 8.0, 20 mM NaCl, 20 mM $MgCl_2$, 0.1 mM EDTA). Transcription reactions were initiated by adding 100 μM of a synthetic ApC-Cy3 dinucleotide (Horizon Discovery) and 25 μM ATP/UTP/GTP nucleotides at 37°C for 10 min, thus yielding a fluorescent halted complex. The sample was next passed through a Sephadex G50 column to remove any free nucleotides and transcription resumed upon addition of all four rNTPs at 1 mM and heparin (450 μg/ml) to prevent re-initiation of transcription. The resulting released transcript was hybridized to the 5′-biotinylated capture probe (Anchor_Bio oligonucleotide) complementary to the 3′-end capture sequence, allowing immobilization of the complex on the microscope slide in absence of a TEC. The capture probe was mixed in a ratio of 10:1 with the RNA transcript and added 5 min before adding the sample on to the microscope slide.

In the case of pTEC transcription, the DNA templates contained a biotin at the 5′-end of the tDNA strand. Streptavidin was mixed in a ratio of 5:1 with the DNA template for 5 min before starting the transcription reaction.

30S purification and fluorescent labeling for single-molecule colocalization experiments

A plasmid (pKK3535) encoding a mutant 16*S* rRNA with an extension at the tip of helix 44 (h44) was obtained from the Puglisi laboratory and expressed in *E. coli*. This allows labeling of the 30*S* subunits using a fluorescent DNA oligonucleotide complementary to the h44 extension. Single salt-washed ribosomes were prepared using previously described protocols with minor modifications (*41*, *66*). Briefly, the pKK3535 expressing strain containing mutated ribosomes was grown in LB medium at 37°C to an OD_{600} of 0.8 to 1 starting from an overnight culture. The cells were then cooled at 4°C for 45 min and pelleted at 5,000 rpm for 15 min. All subsequent steps were performed on ice or at 4°C. The cell pellet was resuspended in buffer A (20 mM Tris-HCl, pH 7.05 at 25°C, 100 mM NH_4Cl, 10 mM $MgCl_2$, 0.5 mM EDTA, and 6 mM β-mercaptoethanol), and the cells were lysed in a single pass using a M-110L Microfluidizer Processor (Microfluidics). The lysate was cleared by centrifugation at 16,000 rpm in a JA-20 Rotor. The cleared lysate was then layered on top of a 35 ml sucrose cushion (1.1 M sucrose, 20 mM Tris-HCl, pH 7.0 at 25°C, 500 mM NH_4Cl, 10 mM $MgCl_2$, and 0.5 mM EDTA) in a Beckman Type 45 Ti Rotor and centrifuged overnight at 37,000 rpm. The pellet was washed twice with 1 ml buffer B (20 mM Tris-HCl, pH 7.0 at 25°C, 500 mM NH_4Cl, 10 mM $MgCl_2$, and 0.5 mM EDTA) and resuspended in 6 ml buffer B by gentle stirring. The salt-washed 70*S* ribosomes were then dialyzed against low magnesium buffer E (50 mM Tris-HCl, pH 7.0 at 25°C, 150 mM NH_4Cl, 1 mM $MgCl_2$, and 6 mM β-mercaptoethanol) three times to induce ribosomal subunit dissociation. Next, 100 A_{260} units of the dissociated ribosomes were loaded on a 36 ml 0-20% sucrose gradient and separated by centrifugation at 20,000 rpm for 18 hours in a Beckman SW28 rotor. The gradients were then fractionated using a Brandel Gradient fractionator coupled with a UV signal monitor. Appropriate fractions were pooled together as pure 30*S* and pure 50S fractions. The 30*S* and 50S fractions were then sedimented separately for 12 hours at 66,000 rpm in a Beckman Type 70 Ti Rotor. Pelleted subunits were resuspended in storage buffer (50 mM Tris-HCl, pH 7.5 at 25°C, 70 mM NH_4Cl, 30 mM KCl, 7 mM $MgCl_2$, and 6 mM β-mercaptoethanol) and flash frozen with liquid nitrogen and stored at −80°C. bS1-depleted 30*S* subunits (30*S* ΔbS1) were prepared by incubation of the purified 30*S* subunits with polyU resin according to a method described previously (*67*). bS1 content in our 30*S* preparations was assessed by a composite nondenaturing 3% polyacrylamide: 0.5% agarose gel following a method established by Dahlberg *et al.* (*68*). The gel was stained with SYBR-Gold and imaged using an Amersham Typhoon scanner (GE Lifesciences). Gel images were quantified with the ImageLab (Bio-Rad Laboratories) software.

To observe direct binding of the 30*S* to the nascent mRNA, we doubly labeled the *E. coli* 30*S* subunits with Cy5 by hybridizing a dual Cy5-labeled DNA oligonucleotide to the engineered h44 extension of the 16*S* rRNA. The 30*S* labeling was performed with a 10-fold excess of dual Cy5-labeled DNA oligonucleotide at a final 30*S* concentration of 1 μM and a buffer composition (50 mM Tris-OAc, pH 7.5 at 25°C, 100 mM KCl, 5 mM NH_4OAc, 0.5 mM $Ca(OAc)_2$, 5 mM $Mg(OAc)_2$, 6 mM β-mercaptoethanol, 0.5 mM EDTA, 5 mM putrescine, and 1 mM spermidine), which has been optimized for the activity of purified ribosomes (Blanchard *et al.* 2004, PNAS). The reaction was protected from light and incubated for 10 min at 37°C and then 60 min at 30°C and finally cooled gradually to room temperature. Excess fluorescent oligonucleotides were removed by spin column purification (Millipore, UFC510024), and the solution containing the labeled 30*S* subunits was flash frozen in aliquots and stored at −80°C. The final concentration of the 30*S* in the recovered solution was determined spectrophotometrically using the extinction coefficient ε_{260} = 14492753.62 M^{-1} cm^{-1} for 30*S* and ε_{650} = 250000 M^{-1} cm^{-1} for Cy5.

Expression and purification of E. coli *ribosomal protein bS1 for single-molecule colocalization experiments*

A plasmid encoding the *E. coli* ribosomal protein bS1, with a cleavable N-terminal His-tag was prepared by mutagenesis from the ASKA(−) clone JW0894 (National BioResource Project—*E. coli* at the National Institute of Genetics) (*69*). pCA24N_6xHis-TEV_rpsA was expressed in the *E. coli* BLR(DE3) strain using conditions based on those described before (*70*). Briefly, 1 L of LB-Miller broth containing 68 μg/ml chloramphenicol was inoculated 1:500 from a saturated overnight culture and grown with shaking at 37°C, induced with 1 mM IPTG at an OD_{600} ~0.6, and harvested 2h post-induction. All subsequent steps were performed at 4°C or

on ice. The cell pellet was lysed using a microfluidizer in 30 ml of buffer B (15 mM Tris-HCl, pH 7.05 at 25°C, 30 mM NH_4Cl, 10 mM $MgCl_2$, 6 mM β-mercaptoethanol, 0.1 mM PMSF), and cleared by centrifugation. The cleared lysate was combined with 5 ml of Ni-NTA Agarose resin (Qiagen, 30210) pre-equilibrated in buffer B and incubated for ~2.5 hours. The resin was washed with 25 ml of buffer C (15 mM Tris-HCl, pH 7.05 at 25°C, 30 mM NH_4Cl, 10 mM $MgCl_2$, 6 mM β-mercaptoethanol, 10 mM imidazole, pH 8.0) containing 500 mM NaCl to reduce the amount of copurifying RNA, and then washed again with 25 ml of buffer C to remove excess NaCl. Bound protein was eluted using buffer D (15 mM Tris-HCl, pH 7.05 at 25°C, 30 mM NH_4Cl, 10 mM $MgCl_2$, 6 mM β-mercaptoethanol, 250 mM imidazole, pH 8.0). Fractions containing significant amounts of 6His-TEV-bS1 were pooled and the concentration of 6His-TEV-bS1 was estimated from the A280 of the solution (ε280 = 48 930 M^{-1} cm^{-1}, ExPASy ProtParam, Swiss Institute of Bioinformatics). The N-terminal His-tag was cleaved using TEV protease during overnight dialysis into buffer E (15 mM Tris-HCl, pH 7.05 at 25°C, 5 mM NH_4Cl, 10 mM $MgCl_2$, 6 mM β-mercaptoethanol). The cleaved His-tag and TEV protease were separated from bS1 using 5 ml of Ni-NTA Agarose resin (Qiagen) pre-equilibrated in buffer E, and the bS1-containing flow-through was loaded on a 5 ml Q Sepharose Fast Flow anion exchange column (GE Healthcare, 17-0510-01), pre-equilibrated with buffer E. The bS1 protein was eluted using a step-wise gradient of buffer F (15 mM Tris-HCl, pH 7.05 at 25°C, 600 mM NH_4Cl, 10 mM $MgCl_2$, 6 mM β-mercaptoethanol) in buffer E. bS1-containing fractions were pooled, concentrated using a centrifugal filtration device, and dialyzed into protein storage buffer A(10) (25 mM Tris-HCl, pH 7.05 at 22°C, 100 mM NH_4Cl, 10 mM $MgCl_2$, 10% v/v glycerol, 6 mM β-mercaptoethanol). The bS1 concentration was measured after dialysis (ε_{280} = 47 440 M^{-1} cm^{-1}), then snap frozen in aliquots and stored at −80°C. This final protein solution had a measured 260/280 absorbance ratio of 0.74, suggesting the absence of any copurifying nucleic acid.

Single-molecule experiments

All single molecule fluorescence microscopy experiments were performed using the Oxford Nanoimager (ONI) microscope in TIRF mode. All movies were collected at 100 ms time-resolution using an intensified CCD camera (Hamamatsu C13440-20CU scientific CMOS camera). PEG-passivated glass coverslips with a chamber were assembled as described in previous works (*71*). The surface of the chamber was coated with streptavidin (0.2 mg/ml) for 10-15 min before flowing the released transcripts hybridized to the CP. In the case of pTEC analysis, the fluorescent pTECs were directly injected into the chamber using the biotin-streptavidin roadblock for immobilization. The excess of unbound complexes was then washed off the chamber with transcription buffer.

An enzymatic oxygen-scavenging system (OSS) consisting of 44 mM glucose, 165 U/ml glucose oxidase from *Aspergillus niger*, 2170 U/ml catalase from *Corynebacterium glutamicum* and 5 mM Trolox was added to extend the lifetime of the fluorophores and to prevent photo-blinking of the dyes (*72*) as well as 0.2 nM dual Cy5-labeled 30*S* and was allowed to equilibrate for 5 min prior to imaging. bS1 protein (when supplemented) was added at a molar ratio of 4:1 with WT-30*S*. The raw movies were collected for 15 min with direct green (532 nm) and red (640 nm) laser excitation.

Locations of molecules and fluorophore over time traces were extracted from raw movie files using MATLAB (MathWorks). Genuine fluorescence time traces for individual molecules were selected manually and analyzed using custom MATLAB (The MathWorks) scripts using the following criteria: single-step photobleaching of Cy3 and at least two Cy5 intensity spikes of more than twofold above the background intensity. Dual Cy5 labeling of 30*S* allowed us to distinguish 30*S* dissociation events (single-step Cy5 intensity decrease) from photobleaching events (double-step Cy5 intensity decrease). Traces showing binding events were idealized using a two-state hidden Markov model for the unbound and bound states in QuB (*73*). From the idealized traces, dwell times of 30*S* subunits in the bound (τ_{bound}) and the unbound ($\tau_{unbound}$) states were calculated. Cumulative of bound and unbound dwell-time distributions were plotted and fitted in OriginLab with single exponential or double exponential functions to obtain the lifetimes in the bound and unbound states. The dissociation rates (k_{off}) were calculated as the inverse of the τ_{bound}, whereas the association rates (k_{on}) were calculated by dividing the inverse of the $\tau_{unbound}$ by the concentration of 30*S* subunits used during the data collection. The statistical significance of differences in the rate constants was determined using the two-tailed Student's *t* test. P values <0.05 were considered significant.

In vivo DSSO cross-linking and affinity purification

RpoB FLAG-tagged *E. coli* (Horizon Discovery SPA-tagged strain) were picked from glycerol stocks and precultured in LB medium containing 50 μg/ml kanamycin. Precultures were incubated overnight at 37°C with constant agitation at 200 rpm. Subsequently, 250 ml of terrific broth was inoculated with the preculture to achieve a starting OD_{600} of 0.15. The cultures were grown at 37°C with continuous shaking at 200 rpm until an OD_{600} of 1.4 was reached. Cells were then harvested by centrifugation at 2500*g* and 4°C for 7 min. The resulting pellet was washed with 30 ml of PBS without magnesium and calcium and spun down. For the cross-linking reaction, the 2.25 g of wet cell mass were resuspended in PBS in the presence of disucciinimidyl sulfoxide (DSSO) solubilised in dimethylformamide (DMF, Thermo Fisher Scientific) to a final concentration of 7.5 mM DSSO in PBS containing 5% DMF. The reaction was incubated for 30 min at room temperature on a tilting platform and then quenched by adding 50 mM Tris-HCl pH 7.5. Cross-linked cells were then spun down at 4°C, snap-frozen in liquid nitrogen, and stored at −80°C.

The cells were resuspended to a concentration of 0.25 g wet cell mass/ml in lysis buffer (20 mM HEPES-KOH, pH 7.5, 6 mM $MgCl_2$, 150 mM NaCl, 1 mM DTT) supplemented with 1 spatula tip of lysozyme, EDTA-free protease inhibitors (Roche) and DNase I (genaxxon). Lysis was further aided by sonication on ice using a Bandelin Sonoplus sonicator (3 min, 50% output, 3 s on, 10 s off). The lysate was then clarified by centrifugation at 14,000*g* and 4°C for 40 min. Affinity purification was performed with 140 μl of M2A anti-FLAG agarose bead slurry (Sigma Aldrich) prepared according to the manufacturer's protocol before the addition of the lysate. The clarified lysate was applied to the beads and bound overnight at 4°C with end-over-end rotation. The beads were washed three times with M2S buffer (10 mM Tris-HCl, 100 mM NaCl, 10% glycerol) finally equilibrated with TICO buffer (20 mM HEPES-KOH, 6 mM $Mg(OAc)_2$, 30 mM KOAc). In the final step, the buffer volume was adjusted to 200 μl, and eluted with TEV protease (New England BioLabs) overnight at 4°C. The eluate proteins were then precipitated with acetone and stored at −20°C until digestion.

Peptide preparation for mass spectrometry

The protein pellet was processed for mass spectrometry by in-solution digestion. Briefly, the pellet was resuspended in 8 M urea at room temperature and cysteines were reduced with 2.5 mM DTT and alkylated with 5 mM iodoacetamide. Urea concentration was brought down to 2 M by dilution in 50 mM NH_4HCO_3 before the addition of tryspin (1:50 weight/weight ratio, Pierce) for overnight digestion at room temperature. The peptides were desalted by StageTip extraction with a C18 matrix (Empore) and subsequently separated by size exclusion chromatography on a Superdex Peptide 3.2/300 increase column (Cytiva) equilibrated with 30% acetonitrile, 0.1% trifluoroacetic acid. Next, 50-μl fractions were collected and early eluting fractions were taken for cross-linking MS acquisitions by LC-MS.

Cross-linking mass spectrometry data acquision

LC-MS analysis of SEC-enriched cross-linked peptides was performed using an Orbitrap Fusion Lumos tribrid mass spectrometer (Thermo

Fisher Scientific) coupled to an Ultimate 3000 RSLC nano system (Dionex, Thermo Fisher Scientific). The column was a C18 50-cm pepMap EasySpray column (C18, 50 cm, 75 µm ID, 2 µm particle size, 100 Å pore size, Thermo Fisher Scientific). Mobile phase A consisted of 0.1% formic acid by volume and mobile phase B of 80% acetonitrile, 0.1% formic acid. Samples were loaded in 4% B and separated over 120-min gradients matched to each SEC fraction. Each fraction was injected twice. The experiment was performed in data-dependent acquisition (DDA) mode with a duty cycle of 2.5 s. The MS1 settings were: resolution 120000, maximum injection time 50 ms with a normalized automatic gain control of 250%. The MS1 scan ranged from 400 to 1450 m/z. Precursors ranging from charge state 3 to charge state 7 were selected for MS2 with a decision tree strategy (*74*) that prioritizes charge states 4 to 7 before moving on to acquiring charge state 3. In a first injection, the precursors are selected in order of decreasing intensity, and in a second injection precursor selection moved from highest to lowest charge. MS2 scans were acquired with a resolution of 60000 and HCD fragmentation with normalized stepped normalized collision energies of 18, 24, 30. The normalized automatic gain control target was set to 250% with a maximum ion injection time of 118ms.

Cross-linking mass spectrometry data analysis

The raw data was searched against the *E. coli* proteome in MaxQuant 1.6.12.0 (*75*) and the top 300 proteins by iBAQ were used to construct a database for the cross-linking MS search. For cross-linking MS, raw files were converted to mascot generic format using ProteoWizard MSConvert version 3.0.11729 (*76*) and recalibrated in both MS1 and MS2 using the mass error from a linear proteomic search to account for mass shifts during the measurements. The spectra were then analyzed using xiSEARCH 1.7.6.1 (*77*) with MS1/MS2 error tolerances of 3 and 5 ppm, respectively. The search was performed with carbamidomethylation of cysteine as a fixed modification and methionine oxidation as a variable modification. The DSSO crosslinker was defined as cleavable and reactive with K,S,T,Y resides and protein N-termini, with a score penalty for matches to S,T,Y residues. Modifications related to the cross-linker included hydrolysed DSSO (+176.0143295 Da) and amidated DSSO (+176.0143295 Da), searched on protein N-terminini and K,S,T,Y residues of linear peptides. The search was also set to account for noncovalent associations (*78*) and two missed cleavages. Results were then filtered in xiFDR to a 5% false discovery rate at the residue pair level using the boosting feature and exported to xiView.org for visualization. Accessible interaction for volumes for RNAP against the 30*S* subunit were computed with DisVis 2.2.0 in "quick scanning" mode (*79*).

REFERENCES AND NOTES

1. M. A. Sørensen, J. Fricke, S. Pedersen, Ribosomal protein S1 is required for translation of most, if not all, natural mRNAs in *Escherichia coli* in vivo. *J. Mol. Biol.* **280**, 561–569 (1998). doi: 10.1006/jmbi.1998.1909; pmid: 9677288
2. J. Shine, L. Dalgarno, The 3′-terminal sequence of *Escherichia coli* 16*S* ribosomal RNA: Complementarity to nonsense triplets and ribosome binding sites. *Proc. Natl. Acad. Sci. U.S.A.* **71**, 1342–1346 (1974). doi: 10.1073/pnas.71.4.1342; pmid: 4598299
3. J. A. Steitz, K. Jakes, How ribosomes select initiator regions in mRNA: Base pair formation between the 3′ terminus of 16*S* rRNA and the mRNA during initiation of protein synthesis in *Escherichia coli*. *Proc. Natl. Acad. Sci. U.S.A.* **72**, 4734–4738 (1975). doi: 10.1073/pnas.72.12.4734; pmid: 1107998
4. K. Saito, R. Green, A. R. Buskirk, Translational initiation in *E. coli* occurs at the correct sites genome-wide in the absence of mRNA-rRNA base-pairing. *eLife* **9**, e55002 (2020). doi: 10.7554/eLife.55002; pmid: 32065583
5. C. Backendorf *et al*., Basepairing potential of the 3′ terminus of 16*S* RNA: Dependence on the functional state of the 30*S* subunit and the presence of protein S21. *Nucleic Acids Res.* **9**, 1425–1444 (1981). doi: 10.1093/nar/9.6.1425; pmid: 7232220
6. B. M. Burmann *et al*., An α helix to β barrel domain switch transforms the transcription factor RfaH into a translation factor. *Cell* **150**, 291–303 (2012). doi: 10.1016/j.cell.2012.05.042; pmid: 22817892
7. S. Chatterjee, A. Chauvier, S. S. Dandpat, I. Artsimovitch, N. G. Walter, A translational riboswitch coordinates nascent transcription-translation coupling. *Proc. Natl. Acad. Sci. U.S.A.* **118**, e2023426118 (2021). doi: 10.1073/pnas.2023426118; pmid: 33850018
8. H. El Sayyed, O. J. Pambos, M. Stracy, M. E. Gottesman, A. N. Kapanidis, Single-molecule tracking reveals the functional allocation, in vivo interactions, and spatial organization of universal transcription factor NusG. *Mol. Cell* **84**, 926–937.e4 (2024). doi: 10.1016/j.molcel.2024.01.025; pmid: 38387461
9. T. Yokoyama *et al*., Structural insight into bacterial co-transcriptional translation initiation. bioRxiv, 2024.03.19.585385 (2024). doi: 10.1101/2024.03.19.585385
10. M. Irastortza-Olaziregi, O. Amster-Choder, Coupled transcription-translation in prokaryotes: An I. *Front. Microbiol.* **11**, 624830 (2021). doi: 10.3389/fmicb.2020.624830
11. M. W. Webster, A. Weixlbaumer, Macromolecular assemblies supporting transcription-translation coupling. *Transcription* **12**, 103–125 (2021). doi: 10.1080/21541264.2021.1981713; pmid: 34570660
12. G. Demo *et al*., Structure of RNA polymerase bound to ribosomal 30*S* subunit. *eLife* **6**, e28560 (2017). doi: 10.7554/eLife.28560; pmid: 29027901
13. P. Milón, M. V. Rodnina, Kinetic control of translation initiation in bacteria. *Crit. Rev. Biochem. Mol. Biol.* **47**, 334–348 (2012). doi: 10.3109/10409238.2012.678284; pmid: 22515367
14. M. A. Canonaco, C. O. Gualerzi, C. L. Pon, Alternative occupancy of a dual ribosomal binding site by mRNA affected by translation initiation factors. *Eur. J. Biochem.* **182**, 501–506 (1989). doi: 10.1111/j.1432-1033.1989.tb14856.x; pmid: 2666129
15. M. H. de Smit, J. van Duin, Translational standby sites: How ribosomes may deal with the rapid folding kinetics of mRNA. *J. Mol. Biol.* **331**, 737–743 (2003). doi: 10.1016/S0022-2836(03)00809-X; pmid: 12909006
16. S. M. Studer, S. Joseph, Unfolding of mRNA secondary structure by the bacterial translation initiation complex. *Mol. Cell* **22**, 105–115 (2006). doi: 10.1016/j.molcel.2006.02.014; pmid: 16600874
17. C. O. Gualerzi, C. L. Pon, Initiation of mRNA translation in bacteria: Structural and dynamic aspects. *Cell. Mol. Life Sci.* **72**, 4341–4367 (2015). doi: 10.1007/s00018-015-2010-3; pmid: 26259514
18. X. Qu, L. Lancaster, H. F. Noller, C. Bustamante, I. Tinoco Jr., Ribosomal protein S1 unwinds double-stranded RNA in multiple steps. *Proc. Natl. Acad. Sci. U.S.A.* **109**, 14458–14463 (2012). doi: 10.1073/pnas.1208950109; pmid: 22908248
19. M. Duval *et al*., *Escherichia coli* ribosomal protein S1 unfolds structured mRNAs onto the ribosome for active translation initiation. *PLOS Biol.* **11**, e1001731 (2013). doi: 10.1371/journal.pbio.1001731; pmid: 24339747
20. A. Zamir, R. Miskin, D. Elson, Interconversions between inactive and active forms of ribosomal subunits. *FEBS Lett.* **3**, 85–88 (1969). doi: 10.1016/0014-5793(69)80103-1; pmid: 11946975
21. D. Moazed, B. J. Van Stolk, S. Douthwaite, H. F. Noller, Interconversion of active and inactive 30 S ribosomal subunits is accompanied by a conformational change in the decoding region of 16 S rRNA. *J. Mol. Biol.* **191**, 483–493 (1986). doi: 10.1016/0022-2836(86)90143-9; pmid: 2434656
22. J. L. McGinnis *et al*., In-cell SHAPE reveals that free 30*S* ribosome subunits are in the inactive state. *Proc. Natl. Acad. Sci. U.S.A.* **112**, 2425–2430 (2015). doi: 10.1073/pnas.1411514112; pmid: 25675474
23. D. Jahagirdar *et al*., Alternative conformations and motions adopted by 30*S* ribosomal subunits visualized by cryo-electron microscopy. *RNA* **26**, 2017–2030 (2020). doi: 10.1261/rna.075846.120; pmid: 32989043
24. R. A. Mooney *et al*., Regulator trafficking on bacterial transcription units in vivo. *Mol. Cell* **33**, 97–108 (2009). doi: 10.1016/j.molcel.2008.12.021; pmid: 19150431
25. M. H. Larson *et al*., A pause sequence enriched at translation start sites drives transcription dynamics in vivo. *Science* **344**, 1042–1047 (2014). doi: 10.1126/science.1251871; pmid: 24789973
26. S. Ray, S. S. Dandpat, S. Chatterjee, N. G. Walter, Precise tuning of bacterial translation initiation by non-equilibrium 5′-UTR unfolding observed in single mRNAs. *Nucleic Acids Res.* **50**, 8818–8833 (2022). doi: 10.1093/nar/gkac635 pmid: 35892287
27. M. W. Webster *et al*., Structural basis of transcription-translation coupling and collision in bacteria. *Science* **369**, 1355–1359 (2020). doi: 10.1126/science.abb5036; pmid: 32820062
28. T. Hussain, J. L. Llácer, B. T. Wimberly, J. S. Kieft, V. Ramakrishnan, Large-scale movements of IF3 and tRNA during bacterial translation initiation. *Cell* **167**, 133–144.e13 (2016). doi: 10.1016/j.cell.2016.08.074; pmid: 27662086
29. G. D'Urso, S. Chat, R. Gillet, E. Giudice, Structural insights into the binding of bS1 to the ribosome. *Nucleic Acids Res.* **51**, 3410–3419 (2023). doi: 10.1093/nar/gkad126; pmid: 36840711
30. G. Yusupova, L. Jenner, B. Rees, D. Moras, M. Yusupov, Structural basis for messenger RNA movement on the ribosome. *Nature* **444**, 391–394 (2006). doi: 10.1038/nature05281; pmid: 17051149
31. A. Korostelev *et al*., Interactions and dynamics of the Shine Dalgarno helix in the 70*S* ribosome. *Proc. Natl. Acad. Sci. U.S.A.* **104**, 16840–16843 (2007). doi: 10.1073/pnas.0707850104; pmid: 17940016
32. A. B. Loveland, A. A. Korostelev, Structural dynamics of protein S1 on the 70*S* ribosome visualized by ensemble cryo-EM. *Methods* **137**, 55–66 (2018). doi: 10.1016/j.ymeth.2017.12.004; pmid: 29247757
33. B. Beckert *et al*., Structure of a hibernating 100S ribosome reveals an inactive conformation of the ribosomal protein S1. *Nat. Microbiol.* **3**, 1115–1121 (2018). doi: 10.1038/s41564-018-0237-0; pmid: 30177741
34. K. Byrgazov *et al*., Structural basis for the interaction of protein S1 with the *Escherichia coli* ribosome. *Nucleic Acids Res.* **43**, 661–673 (2015). doi: 10.1093/nar/gku1314; pmid: 25510494
35. J. Y. Kang *et al*., Structural basis for transcript elongation control by NusG family universal regulators. *Cell* **173**, 1650–1662.e14 (2018). doi: 10.1016/j.cell.2018.05.017; pmid: 29887376
36. C. Zhu *et al*., Transcription factors modulate RNA polymerase conformational equilibrium. *Nat. Commun.* **13**, 1546 (2022). doi: 10.1038/s41467-022-29148-0; pmid: 35318334
37. M. V. Sukhodolets, S. Garges, Interaction of *Escherichia coli* RNA polymerase with the ribosomal protein S1 and the Sm-like ATPase Hfq. *Biochemistry* **42**, 8022–8034 (2003). doi: 10.1021/bi020638i; pmid: 12834354
38. C. Wang *et al*., Structural basis of transcription-translation coupling. *Science* **369**, 1359–1365 (2020). doi: 10.1126/science.abb5317; pmid: 32820061
39. A. Schedlbauer *et al*., A conserved rRNA switch is central to decoding site maturation on the small ribosomal subunit. *Sci. Adv.* **7**, 7 (2021). doi: 10.1126/sciadv.abf7547; pmid: 34088665
40. M. Belinite *et al*., Stabilization of ribosomal RNA of the small subunit by spermidine in *Staphylococcus aureus*. *Front. Mol. Biosci.* **8**, 738752 (2021). doi: 10.3389/fmolb.2021.738752; pmid: 34869582
41. M. Dorywalska *et al*., Site-specific labeling of the ribosome for single-molecule spectroscopy. *Nucleic Acids Res.* **33**, 182–189 (2005). doi: 10.1093/nar/gki151; pmid: 15647501
42. F. Krupp *et al*., Structural basis for the action of an all-purpose transcription anti-termination factor. *Mol. Cell* **74**, 143–157.e5 (2019). doi: 10.1016/j.molcel.2019.01.016; pmid: 30795892
43. S. Marzi *et al*., Structured mRNAs regulate translation initiation by binding to the platform of the ribosome. *Cell* **130**, 1019–1031 (2007). doi: 10.1016/j.cell.2007.07.008; pmid: 17889647

44. S. Nakagawa, Y. Niimura, T. Gojobori, Comparative genomic analysis of translation initiation mechanisms for genes lacking the Shine-Dalgarno sequence in prokaryotes. *Nucleic Acids Res.* **45**, 3922–3931 (2017). doi: 10.1093/nar/gkx124; pmid: 28334743
45. K. R. Andersen, N. C. Leksa, T. U. Schwartz, Optimized *E. coli* expression strain LOBSTR eliminates common contaminants from His-tag purification. *Proteins* **81**, 1857–1861 (2013). doi: 10.1002/prot.24364; pmid: 23852738

ACKNOWLEDGMENTS

We thank D. E. Brodersen for providing the RelB-RelE expression construct; A. Durand and N. Marechal for help with data collection at the IGBMC; the European Synchrotron Radiation Facility for the provision of microscope time on CM01; E. Kandiah and G. Effantin for assistance; S. Afifah Wigati for optimization of EMSA experiments; and members of the Weixlbaumer, Webster, Walter, and Rappsilber labs for critical reading of the manuscript. **Funding:** This work was supported by the Agence Nationale de la Recherche FRISBI ANR-10-INBS-05 (M.W.W., H.R., M.T., C.S.A., A.W.); Agence Nationale de la Recherche ANR-10-LABX-0030-INRT (M.W.W., H.R., M.T., C.S.A., A.W.); Agence Nationale de la Recherche (ANR-10-IDEX-0002-02 to M.W.W., H.R., M.T., C.S.A., A.W.); EMBO (long-term postdoctoral fellowship to M.W.W.); IMCBio (PhD fellowship to H.R.); Zentrales Innovationsprogramm Mittelstand (ZIM) des Bundesministeriums für Wirtschaft und Klimaschutz (16KN073238 to K.C.); European Research Council (starting grant TRANSREG 679734 to A.W.); the National Institutes of Health (grant R35GM131922 to N.G.W.); and the National Science Foundation (MCB grant 2140320 to N.G.W.). The Wellcome Centre for Cell Biology is supported by core funding from the Wellcome Trust (203149 to J.R.); the Biotechnology and Biological Sciences Research Council (BBSRC) Institute Strategic Programme (BB/P013511/1 and BB/X01102X/1 to M.W.W.); and UK Research and Innovation (UKRI) Future Leaders Fellowship (MR/X033481/1 to M.W.W.). **Author contributions:** MWW and AW conceived the study. M.W.W., H.R., A.W., M.T., and C.S.A. acquired, processed, and analyzed the cryo-EM data and built and refined the model. M.T. and N.M. performed the biochemical experiments. A.C. and N.G.W. performed the single-molecule experiments and analyzed the data. A.G., K.C., and J.R. performed the in-cell cross-linking mass spectrometry and analyzed the data. M.W.W., A.C., H.R., A.G., N.G.W., and A.W. wrote and edited the manuscript. **Competing interests:** The authors declare no competing interests. **Data and materials availability:** Electron density maps for complexes were deposited in the EM database (EMD-51616, EMD-51602, EMD-51603, EMD-51604, EMD-51623, EMD-51596, EMD-51597, EMD-51598, EMD-51599, EMD-51600, EMD-51622, EMD-51591, EMD-51592, EMD-51593, EMD-51594, EMD-51595, EMD-51618, EMD-51584, EMD-51585, EMD-51586, EMD-51601, EMD-51617, EMD-51619, EMD-51580, EMD-51581, EMD-51582, EMD-51583, EMD-51620, EMD-51576, EMD-51577, EMD-51578, EMD-51579, EMD-51615, EMD-51572, EMD-51573, EMD-51574, EMD-51575, EMD-51621, EMD-51587, EMD-51588, EMD-51589, EMD-51590, and EMD-51517). Refined coordinates were deposited in the PDB database under accession codes 9GUQ, 9GUX, 9GUW, 9GUS, 9GUR, 9GUT, 9GUU, 9GUP, 9GUV, and 9GR1. Cross-linking MS raw files and identifications were deposited at the ProteomeXChange Jpost with identifier JPST002435 (PXD048229).

SUPPLEMENTARY MATERIALS

science.org/doi/10.1126/science.ado8476
Figs. S1 to S11
Tables S1 to S4
References (*46*–*79*)
MDAR Reproducibility Checklist
Movies S1 to S4
Data S1

Submitted 23 February 2024; accepted 27 September 2024
10.1126/science.ado8476

Science
AAAS

Supplementary Materials for

Molecular basis of mRNA delivery to the bacterial ribosome

Michael W. Webster *et al*.

Corresponding authors: Michael W. Webster, michael.webster@jic.ac.uk; Albert Weixlbaumer, albert.weixlbaumer@igbmc.fr

Science **386**, eado8476 (2024)
DOI: 10.1126/science.ado8476

The PDF file includes:

Other Supplementary Material for this manuscript includes the following:

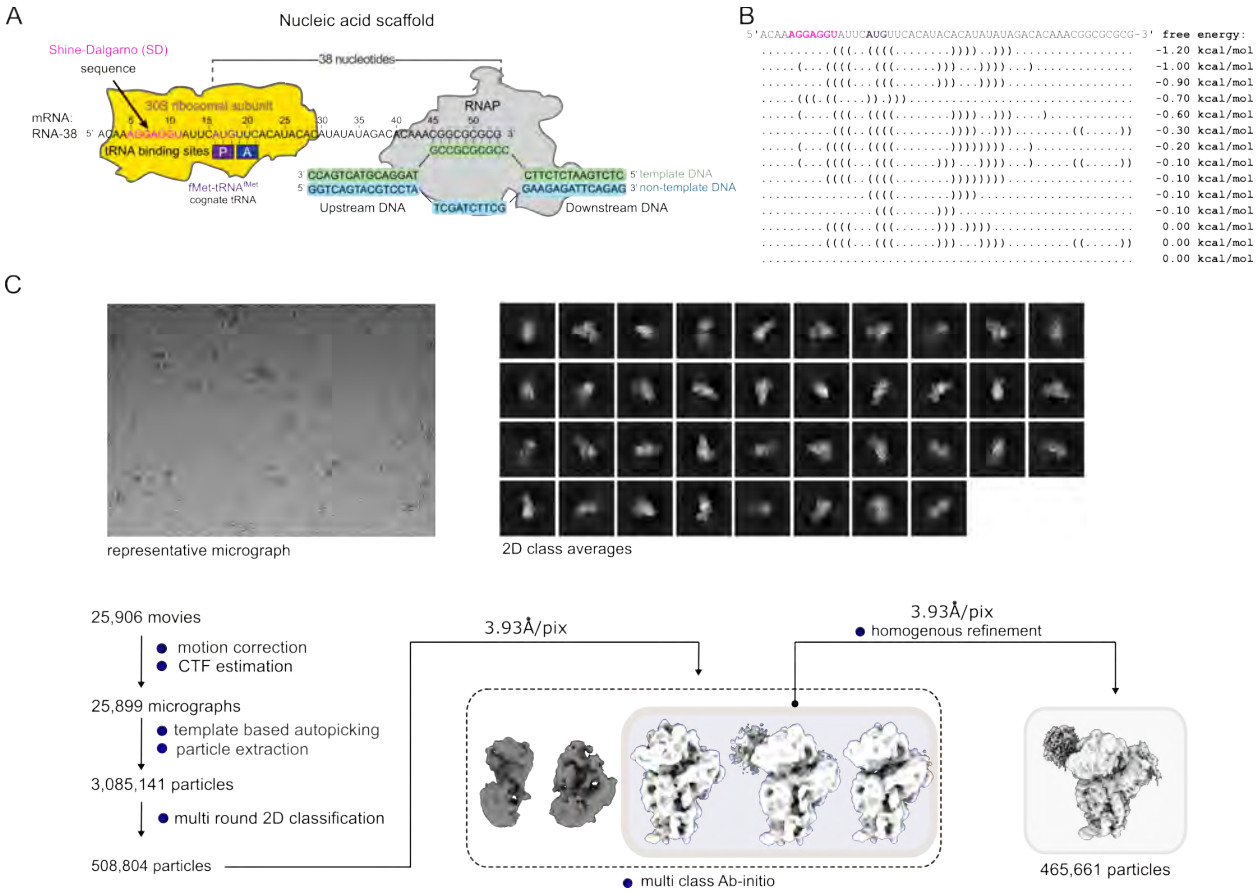

Fig. S1 (part 1). Sample preparation and classification of 30S-RNAP complexes. (**A**) Complex preparation for cryo-EM. RNA polymerase (RNAP, grey) was mixed with DNA and RNA oligonucleotides (template DNA, non-template DNA, and RNA-38) to reconstitute a transcription elongation complex (TEC), which was purified by size-exclusion chromatography and subsequently mixed with 30S ribosomal subunits (gold) and fMet-tRNA^{fMet}. A consensus Shine-Dalgarno (SD, magenta) sequence directs the ribosome to bind the nascent transcript so the start codon (AUG, purple) can accommodate in the ribosomal P-site. (**B**) RNA-38 is predicted to form weak secondary structures. (**C**) Representative micrograph and 2D classes for 30S-TEC complexes (top). Data collection and initial data processing scheme (to be continued in Fig. S1 (part 2) - next page).

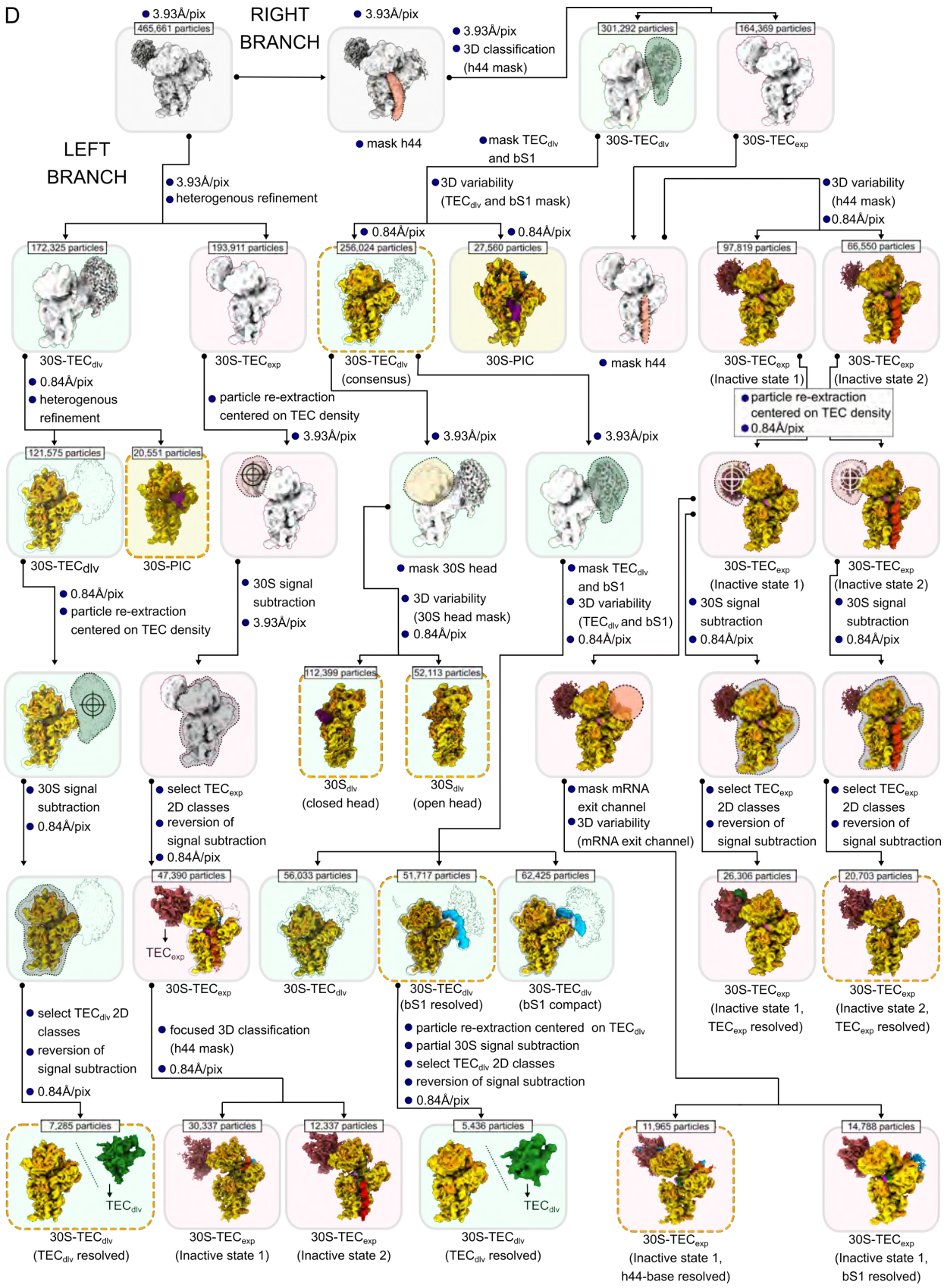
D
3.93Å/pix
465,661 particles
RIGHT BRANCH
3.93Å/pix
mask h44
3.93Å/pix
3D classification (h44 mask)
301,292 particles
164,369 particles
LEFT BRANCH
3.93Å/pix
heterogenous refinement
mask TECdlv and bS1
30S-TECdlv
30S-TECexp
3D variability (TECdlv and bS1 mask)
0.84Å/pix
0.84Å/pix
3D variability (h44 mask)
0.84Å/pix
172,325 particles
193,911 particles
256,024 particles
27,560 particles
97,819 particles
66,550 particles
30S-TECdlv
0.84Å/pix
heterogenous refinement
30S-TECexp
30S-TECdlv (consensus)
30S-PIC
mask h44
30S-TECexp (Inactive state 1)
30S-TECexp (Inactive state 2)
particle re-extraction centered on TEC density
3.93Å/pix
3.93Å/pix
3.93Å/pix
particle re-extraction centered on TEC density
0.84Å/pix
121,575 particles
20,551 particles
30S-TECdlv
30S-PIC
mask 30S head
mask TECdlv and bS1
3D variability (TECdlv and bS1)
0.84Å/pix
30S-TECexp (Inactive state 1)
30S-TECexp (Inactive state 2)
0.84Å/pix
particle re-extraction centered on TEC density
30S signal subtraction
3.93Å/pix
3D variability (30S head mask)
0.84Å/pix
30S signal subtraction
0.84Å/pix
30S signal subtraction
0.84Å/pix
112,399 particles
52,113 particles
30Sdlv (closed head)
30Sdlv (open head)
mask mRNA exit channel
3D variability (mRNA exit channel)
select TECexp 2D classes
reversion of signal subtraction
0.84Å/pix
select TECexp 2D classes
reversion of signal subtraction
select TECexp 2D classes
reversion of signal subtraction
47,390 particles
56,033 particles
51,717 particles
62,425 particles
26,306 particles
20,703 particles
TECexp
30S-TECexp
30S-TECdlv
30S-TECdlv (bS1 resolved)
30S-TECdlv (bS1 compact)
30S-TECexp (Inactive state 1, TECexp resolved)
30S-TECexp (Inactive state 2, TECexp resolved)
select TECdlv 2D classes
reversion of signal subtraction
0.84Å/pix
focused 3D classification (h44 mask)
0.84Å/pix
particle re-extraction centered on TECdlv
partial 30S signal subtraction
select TECdlv 2D classes
reversion of signal subtraction
0.84Å/pix
7,285 particles
30,337 particles
12,337 particles
5,436 particles
11,965 particles
14,788 particles
TECdlv
30S-TECdlv (TECdlv resolved)
30S-TECexp (Inactive state 1)
30S-TECexp (Inactive state 2)
TECdlv
30S-TECdlv (TECdlv resolved)
30S-TECexp (Inactive state 1, h44-base resolved)
30S-TECexp (Inactive state 1, bS1 resolved)

Fig. S1 (part 2). (**D**) Two strategies were employed to classify 30S-TEC complexes. Global classification (left branch) revealed two groups of particles initially: A 30S-TEC_{dlv} complex with additional density surrounding the 30S platform domain (light green background), and a 30S-TEC_{exp} complex (light red background) with additional density close to the mRNA entry channel in a position similar to the TEC in a transcribing-translating expressome (*27*).
Further classification of 30S-TEC_{dlv} particles revealed a small fraction that lacked TEC density and represents a 30S pre-initiation complex with fMet-$tRNA^{fMet}$ bound to the mRNA start codon in the P-site (30S-PIC, yellow background, middle leftmost branch; 30S, gold; fMet-$tRNA^{fMet}$ purple).
Focused classification and partial 30S signal subtraction revealed the density close to the mRNA exit channel in 30S-TEC_{dlv} particles to be a loosely bound TEC (30S-TEC_{dlv}; 30S, gold; TEC_{dlv}, green, bottom leftmost branch).
Focused classification centered on the density close to the mRNA entry channel of 30S-TEC_{exp} particles and partial 30S signal subtraction revealed a TEC coupled through NusG to the 30S (30S-TEC_{exp}; 30S, gold; TEC_{exp} red). Further focused classification using a mask around 16S rRNA helix44 (h44) identified two groups of inactive 30S in 30S-TEC_{exp} particles. In inactive state 1, h44 localizes to the mRNA exit channel while in inactive state 2, h44 relocated to the subunit interface (red orange) but fails to form a functional decoding center (30S-TEC_{exp} Inactive state 1 and 2; 30S, gold; TEC_{exp} red; 2nd and 3rd boxed reconstructions from the left in the bottom row).
An alternative approach using focused classification based on h44 provided consistent results (right branch) and separated 30S-TEC_{dlv} and 30S-PIC (second row, middle) from 30S-TEC_{exp} that were eventually classified into inactive states 1 and 2 (rightmost branch). 3D variability analysis using a mask covering the exit channel revealed a dynamic equilibrium in the extent to which bS1 OB domains bind h44 (Inactive state 1 h44-base resolved and Inactive state 1 bS1 resolved).
3D variability analysis in CryoSPARC, as well as focused classification and refinement using a mask covering the 30S head allowed us to identify subsets of 30S-TEC_{dlv} particles with a closed or open 30S head domain (middle). The 30S with closed head contained fMet-$tRNA^{fMet}$ bound to the solvent side of the 30S neck region (purple). 3D variability analysis using a mask covering TEC_{dlv} and bS1 density revealed variably ordered bS1 (30S-TEC_{dlv} bS1 resolved and 30S-TEC_{dlv} bS1 compact) and confirmed the presence of TEC_{dlv} (green) tethered through the mRNA and bS1 to the 30S platform (bottom row, rightmost reconstruction).
Particle numbers are indicated on top of boxed reconstructions. Reconstructions highlighted with orange dashed boxes represent deposited cryo-EM maps that were used for model building and refinement.

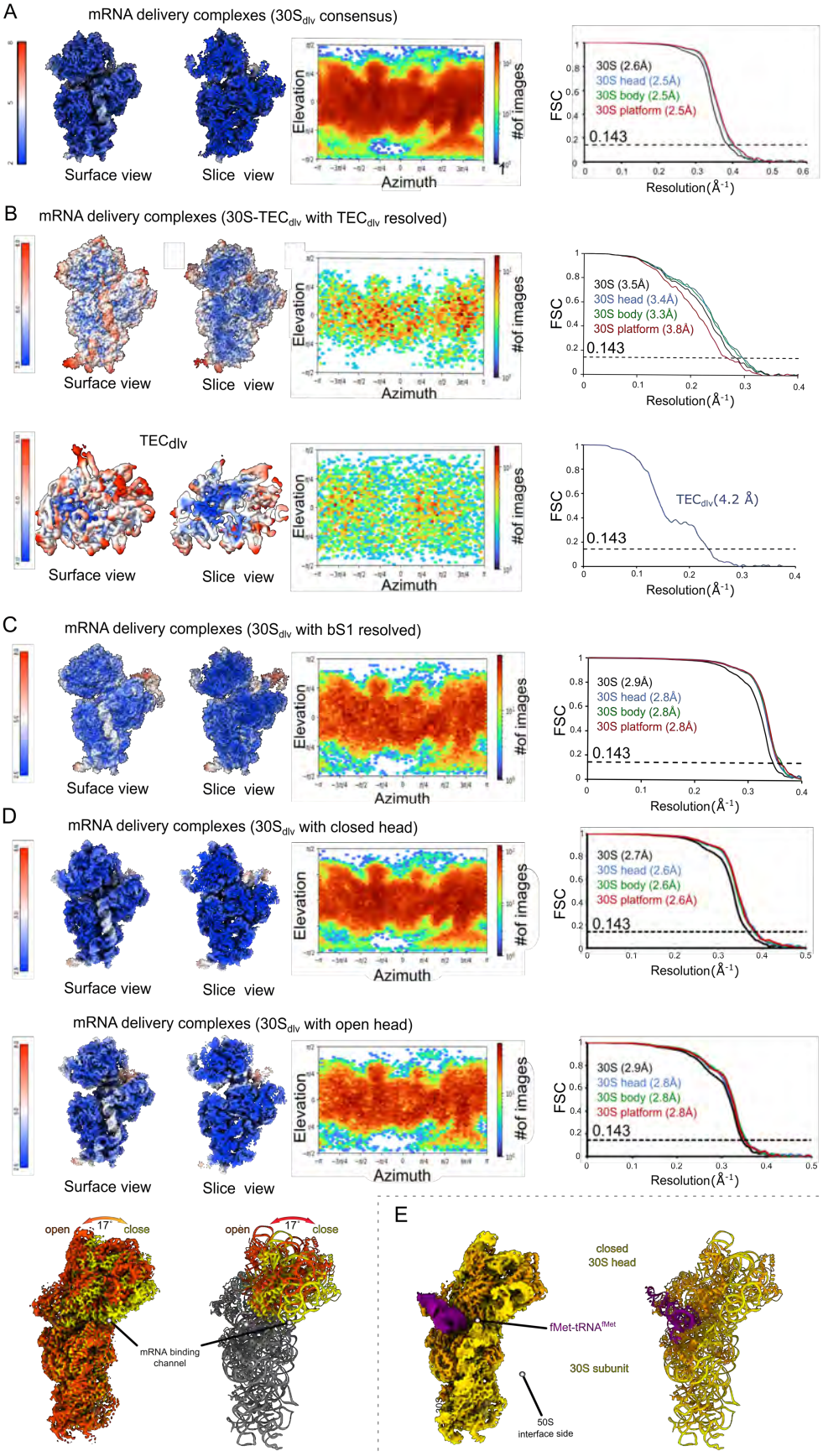
A
mRNA delivery complexes (30S$_{dlv}$ consensus)
Surface view
Slice view
Elevation
Azimuth
#of images
FSC
30S (2.6Å)
30S head (2.5Å)
30S body (2.5Å)
30S platform (2.5Å)
0.143
Resolution(Å^{-1})
B
mRNA delivery complexes (30S-TEC$_{dlv}$ with TEC$_{dlv}$ resolved)
Surface view
Slice view
30S (3.5Å)
30S head (3.4Å)
30S body (3.3Å)
30S platform (3.8Å)
TEC$_{dlv}$
TEC$_{dlv}$(4.2 Å)
C
mRNA delivery complexes (30S$_{dlv}$ with bS1 resolved)
Suface view
30S (2.9Å)
30S head (2.8Å)
30S body (2.8Å)
30S platform (2.8Å)
D
mRNA delivery complexes (30S$_{dlv}$ with closed head)
30S (2.7Å)
30S head (2.6Å)
30S body (2.6Å)
30S platform (2.6Å)
mRNA delivery complexes (30S$_{dlv}$ with open head)
open
close
17°
mRNA binding channel
E
closed 30S head
fMet-tRNA^{fMet}
30S subunit
50S interface side

Fig. S2: Local resolution, orientation plots, FSC curves and 30S head movement of mRNA delivery complexes. (**A**) Surface and slice view of the consensus reconstruction of the mRNA delivery complex colored by local resolution. Orientation plot and FSC curves for focused refinements and their nominal resolutions are shown on the right. (**B**) Surface and slice view colored by local resolution of 30S subunit (top) and TEC_{dlv} (bottom), corresponding orientation plots and FSC curves for focused refinements with nominal resolutions (right). These reconstructions correspond to particle subsets that facilitated confirming the presence of a TEC in the delivery position (TEC_{dlv}). (**C**) Same as A and B but for particle subset identified by focused classification with resolved bS1 density. (**D**) Surface and slice view colored by local resolution of 30S subunit with closed head domain (top) and open head domain (middle), corresponding orientation plots and FSC curves for focused refinements with nominal resolutions (right). The 30S head is flexible in all the mRNA delivery complexes and oscillates between an open and closed position according to 3D variability analysis of the consensus dataset affecting the accessibility of the mRNA binding channel (bottom left). Similar head rotations have been observed for all subsets of mRNA delivery complexes (not shown). (**E**) fMet-$tRNA^{fMet}$ (purple) binds the solvent side of the 30S subunit neck region when the head is in a closed position in mRNA delivery complexes. fMet-$tRNA^{fMet}$ interacts mostly through its backbone in the anticodon stem and elbow region with positively charged and polar residues in ribosomal proteins uS2, uS3, uS4 and uS5. It is unclear if this is physiologically relevant or simply the result of non-specific binding.

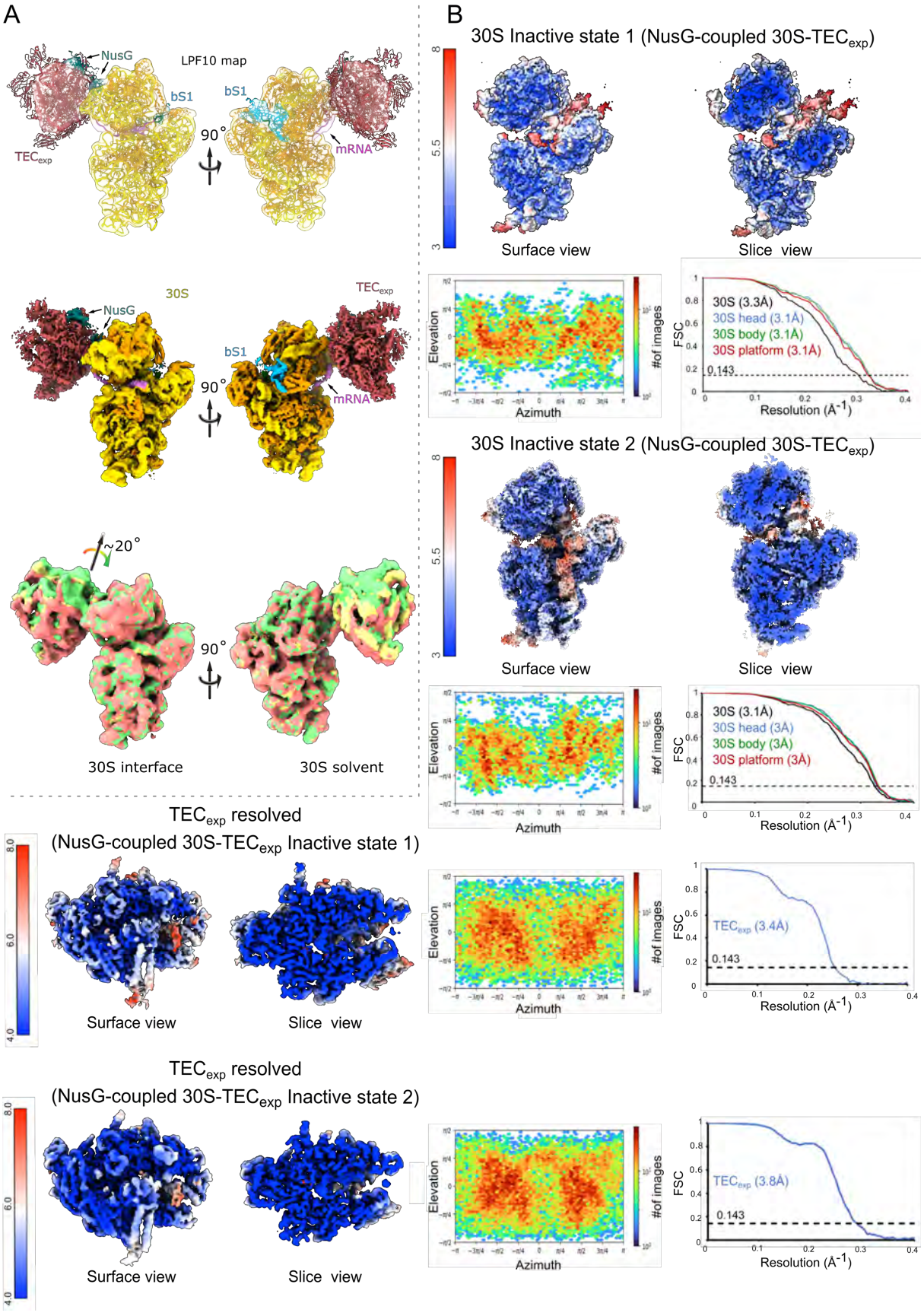
A
NusG
LPF10 map
bS1
bS1
90°
mRNA
TEC$_{exp}$
30S
NusG
TEC$_{exp}$
bS1
90°
mRNA
~20°
90°
30S interface
30S solvent
TEC$_{exp}$ resolved
(NusG-coupled 30S-TEC$_{exp}$ Inactive state 1)
Surface view
Slice view
TEC$_{exp}$ resolved
(NusG-coupled 30S-TEC$_{exp}$ Inactive state 2)
Surface view
Slice view
B
30S Inactive state 1 (NusG-coupled 30S-TEC$_{exp}$)
Surface view
Slice view
Elevation
Azimuth
#of images
FSC
30S (3.3Å)
30S head (3.1Å)
30S body (3.1Å)
30S platform (3.1Å)
0.143
Resolution (Å^{-1})
30S Inactive state 2 (NusG-coupled 30S-TEC$_{exp}$)
Surface view
Slice view
30S (3.1Å)
30S head (3Å)
30S body (3Å)
30S platform (3Å)
TEC$_{exp}$ (3.4Å)
TEC$_{exp}$ (3.8Å)

Fig. S3. Inactive 30S complexes with a TEC tethered through mRNA and NusG. (A) Low-pass filtered transparent map and model (top) and composite map (middle) of the consensus reconstruction for the inactive 30S complexes. A TEC (red, TEC_{exp}) is tethered through the shared mRNA (pink) and through NusG (teal) to the 30S subunit in a manner similar to a NusG-coupled transcribing-translating expressome (PDB: 6ZTJ) (*27*). The mRNA binds ribosomal protein uS3 before entering the mRNA entry channel. 3D variability analysis (bottom) highlights the flexibility of the TEC_{exp} with respect to the 30S subunit. **(B)** Surface and slice views colored by local resolution for the NusG-coupled 30S-TEC_{exp} Inactive state 1 (top), NusG-coupled 30S-TEC_{exp} Inactive state 2 (middle), and for the focused reconstruction of the TEC_{exp} (bottom). Corresponding orientation plots and FSC curves for focused refinements with nominal resolutions are shown.

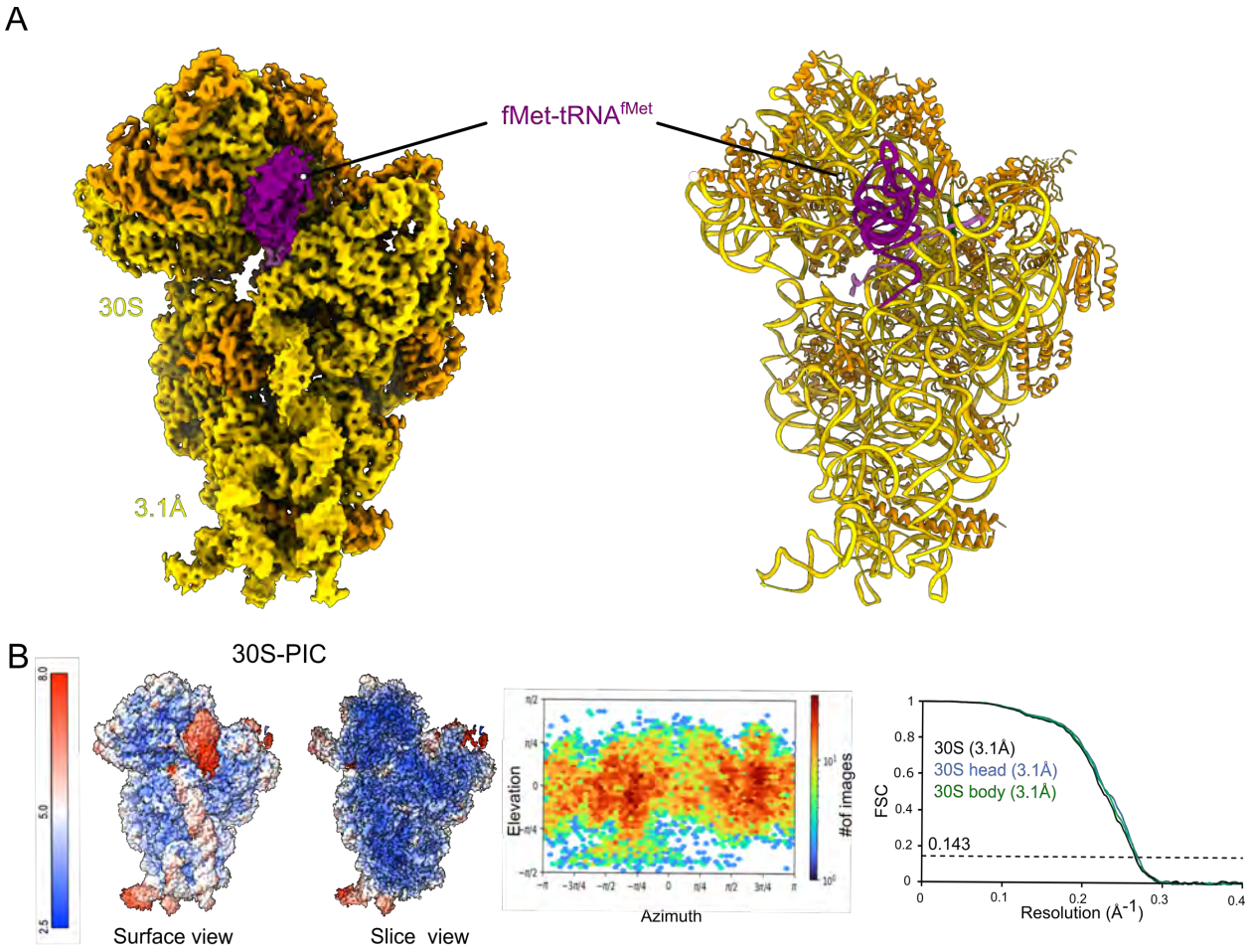

Fig. S4. 30S pre-initiation complex with mRNA and tRNA. (**A**) Map (left) and model (right) of a small fraction of particles, which formed a 30S pre-initiation complex (30S-PIC). The mRNA is accommodated in the main mRNA binding channel and allows interaction with the initiator tRNA, fMet-tRNA^{fMet} (purple), in the ribosomal P-site. (**B**) Surface and slice view colored by local resolution of the 30S-PIC. Corresponding orientation plot and FSC curves for focused refinements with nominal resolutions are shown on the right.

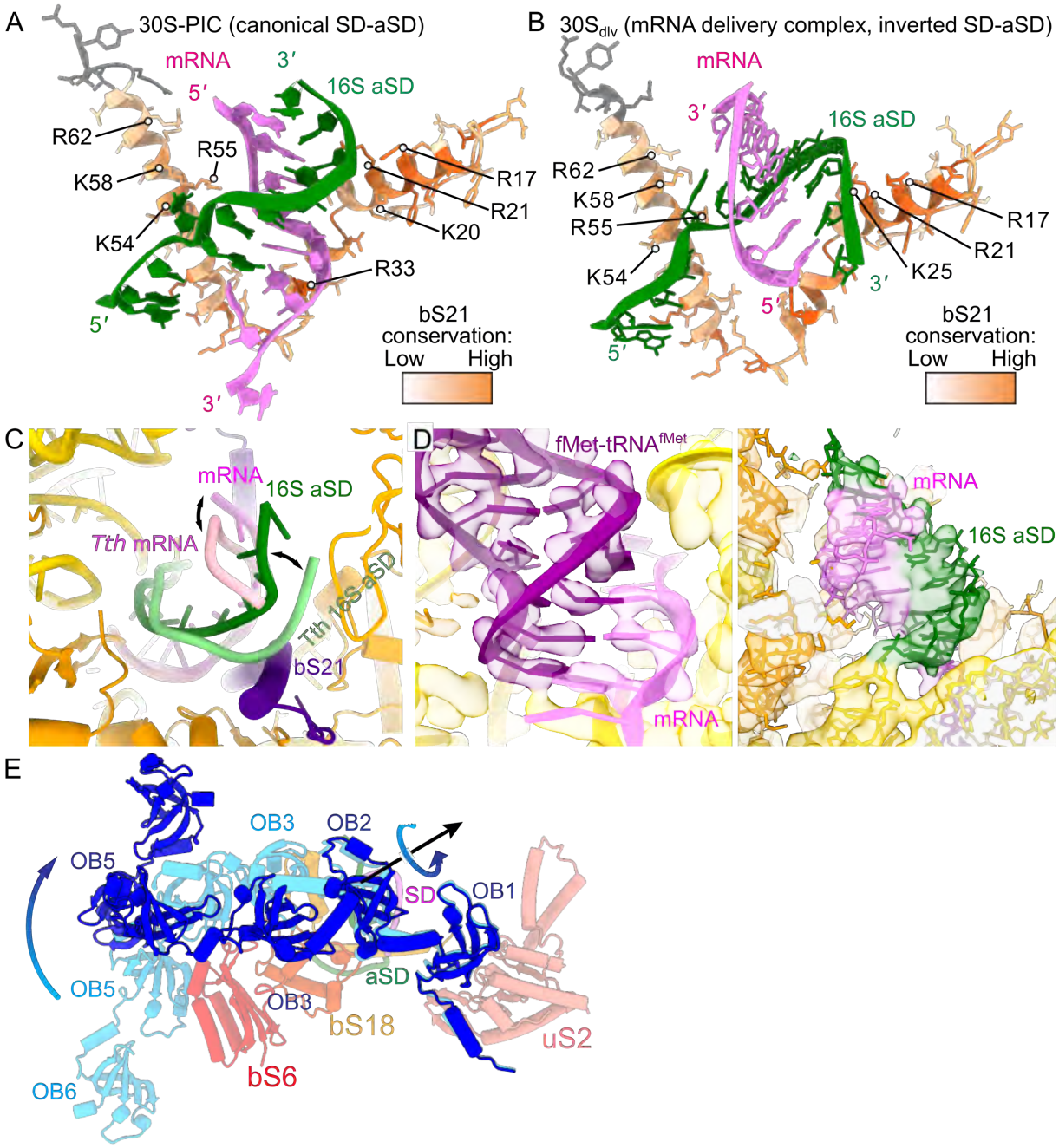

Fig. S5. Comparison and SD-aSD interactions and conformations, and alternative bS1 conformation. (**A**) Structural models of the SD duplex and its interactions with bS21 in the accommodated state (30S-PIC) and (**B**) mRNA delivery complexes (30S$_{dlv}$). bS21 is colored by per-residue conservation (orange, high; white, low) and basic residues that interact with the SD duplex are indicated (R, Arg; K, Lys). (**C**) The orientation of the SD-aSD in our 30S-PIC is most similar to recent 30S-PIC complexes obtained with *Thermus thermophilus* (*T. th.*) ribosomes (PDB: 5LMT) (*28*). The small differences can be explained by the absence of ribosomal protein bS21 in *T. th.* (**D**) fMet-tRNA^{fMet} binds the AUG start codon consistent with previous results (left) and the mRNA forms a canonical SD-aSD helix in the mRNA exit channel of the ribosome (right).

(**E**) bS1 is conformationally heterogeneous and in addition to an extended conformation (cyan) can also adopt an alternative, more compact conformations (dark blue).

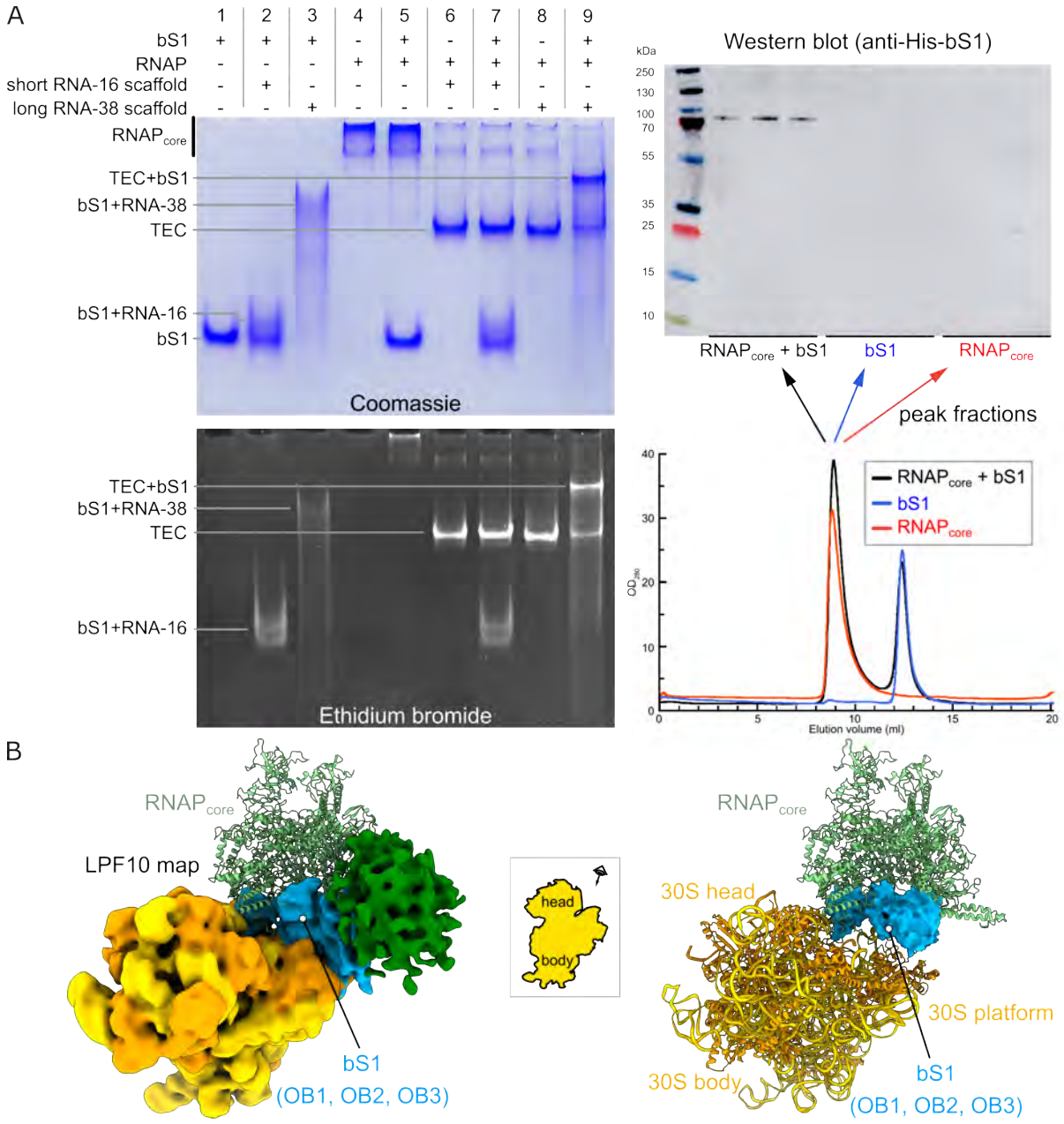

Fig. S6. Ribosomal protein bS1 interacts through the shared mRNA and through a weak and variable interface with a TEC. (**A**) EMSA experiments (left, gel is stained with Coomassie, top, and Ethidium bromide, bottom) suggest that bS1 can only bind and form a stable complex with a TEC if a sufficiently long mRNA is available (compare lanes 7 and 9, RNA-16 is 16nt long, RNA-38 is 53nt long). Size-exclusion chromatography experiments (right) are consistent and suggest only small amounts of bS1 bind and co-purify with a TEC. Note that size-exclusion chromatography experiments in presence of nucleic acids are not shown because they are not conclusive because the bS1 peak broadens as a result of binding to RNA and overlaps with the RNAP peak (compare lane 3 in native gel on the left, which broadens as a result of bS1 binding to RNA-38). (**B**) A recent reconstruction (*12*) of a 30S bound to RNAP core (light green ribbon) via

ribosomal protein uS2 partially overlaps with the wide range of TEC_{dlv} positions indicated by the mRNA delivery complex consensus reconstruction (green density). However, bS1-OB1 to bS1-OB3 (cyan), bound to uS2 would overlap with the position of RNAP core bound to uS2 (right).

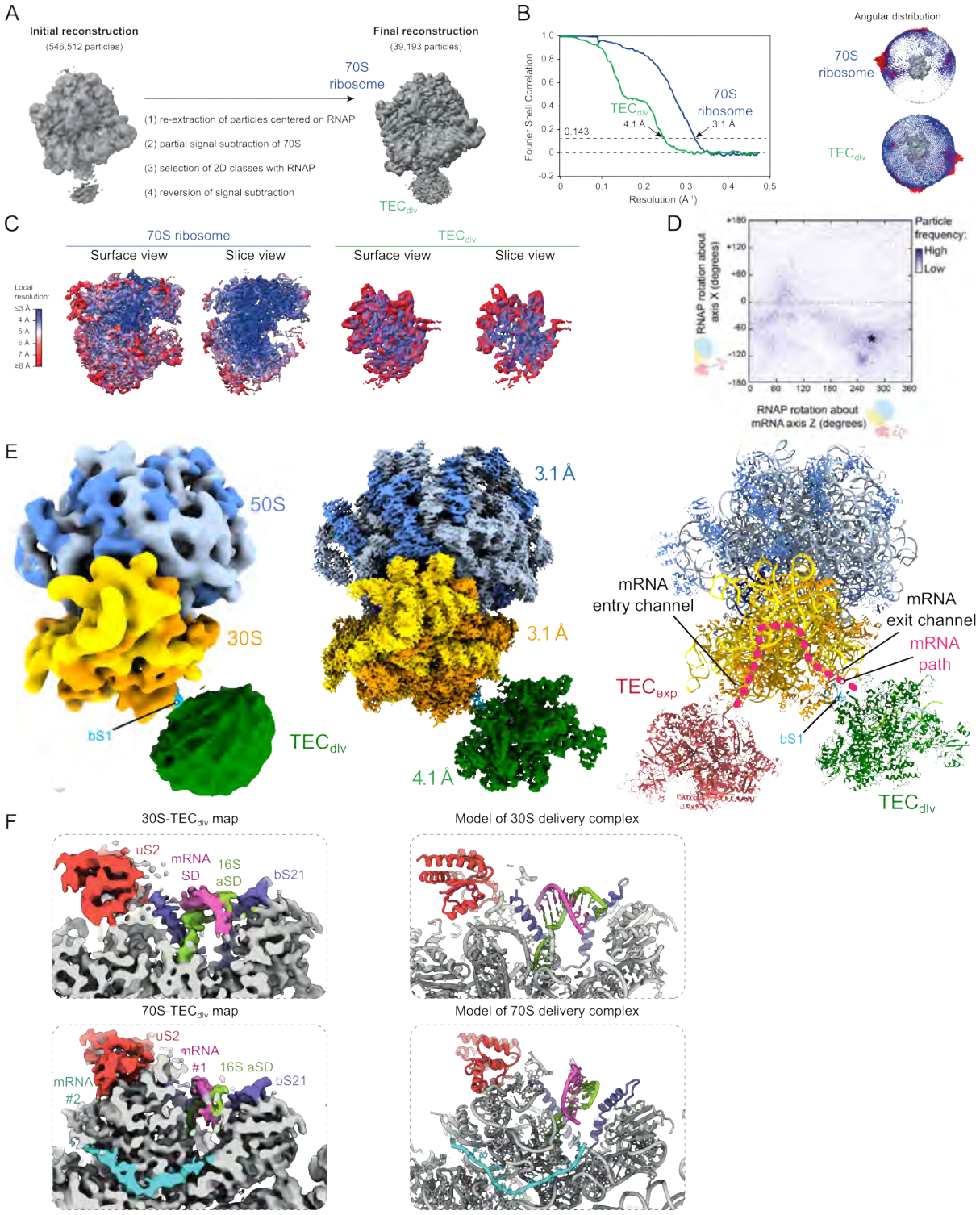

Fig. S7. Structural models of mRNA delivery in the context of a translating 70S ribosome. (**A**) Upon classification (detailed), we identified a subset of particles in a recent reconstruction of an uncoupled *E. coli* expressome (*27*) that contained a TEC in a position consistent with mRNA delivery. (**B**) FSC curves and particle orientation plots for focused 70S and TEC_{dlv} reconstructions.

(**C**) Surface and slice views colored by local resolution for the focused 70S (left) and focused TEC_{dlv} reconstruction (right). (**D**) Plot of TEC_{dlv}-ribosome relative orientation across all imaged particles contributing to the cryo-EM reconstruction. A region of higher particle frequency (asterisk) is the most prevalent complex architecture and was selected for construction of the representative structural model in (E). (**E**) Consensus cryo-EM map filtered to 8 Å resolution (left), focused cryo-EM maps (middle), and atomic model (right) of a 70S ribosome in complex with a TEC that occupies the mRNA delivery position close to ribosomal protein bS1 (cyan). The TEC in the expressome position (red, right) and the mRNA path through the 30S subunit are indicated to highlight the difference. (**F**) Maps of the 70S-TEC_{dlv} complex are consistent with models of the 30S-TEC_{dlv} complex and suggest reorientation of the SD-aSD duplex.

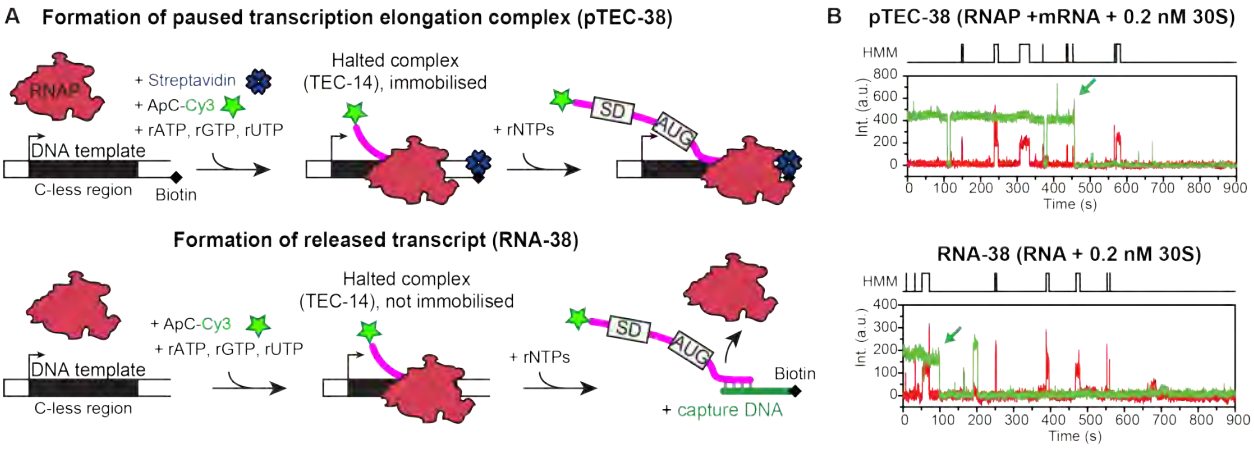

Fig. S8. Sample preparation for single molecule colocalization experiments and representative single molecule time trajectory. (A) Preparation of the paused elongation complex (pTEC-38, top panel) and released transcript (RNA-38, bottom panel) containing the nascent Cy3-labeled mRNA transcript for monitoring 30S binding using single-molecule colocalization via SiM-KARB (*26*). **(B)** Representative single molecule time trajectories showing transient 30S binding (red) to pTEC-38 (green, top panel) and RNA-38 (green, bottom panel). The resulting Hidden Markov Modelling (HMM) is indicated on the top of each trace. Dark green arrows indicate Cy3 fluorophore bleaching.

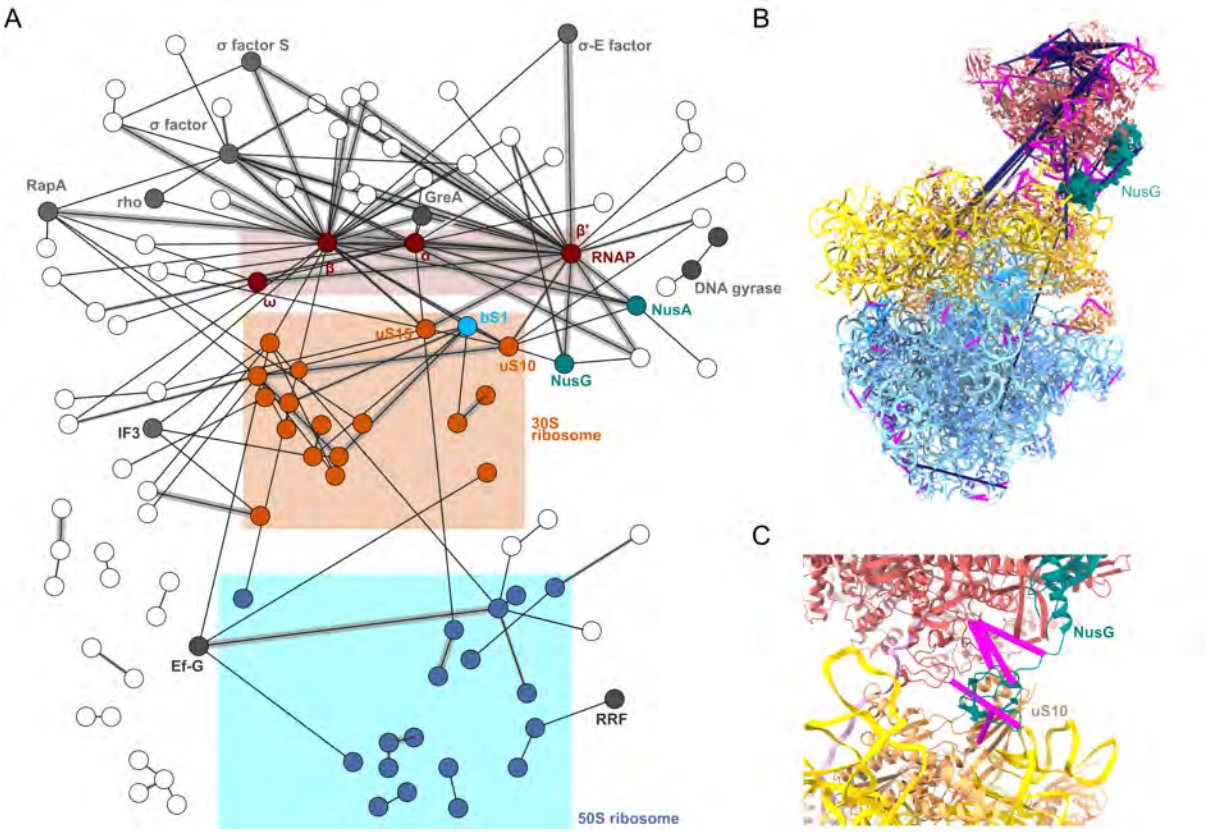

Fig. S9. *In cell* crosslinking MS of RNAP β-subunit-tagged *E. coli* cells. (**A**) *In cell* DSSO CLMS network after affinity enrichment of RpoB (RNAP **β**-subunit). Nodes denote proteins, while edges denote the presence of at least 1 crosslink between the proteins. Edge thickness reflects the number of crosslinks (thinnest, 1 crosslink; medium, 2 crosslinks; and thick, more than 3 crosslinks). The network is reported at a 5% false discovery rate at the residue level and comprises 1,458 residue pairs, 523 of which are heteromeric (involving residues belonging to different proteins). (**B**) Mapping of *in vivo* crosslinks onto the structure of the NusG-coupled expressome (PDB: 6ZTJ) validates the NusG-uS10 interaction as well as the overall architecture of the ribosome and RNAP, while indicating an additional area in which RNAP is proximal to the ribosome (Crosslinks satisfied in model (<30 Å Cα-Cα distance) magenta; crosslinks violated in model (>30 Å Cα-Cα distance) dark purple). (**C**) Zoom in on the NusG-uS10 interaction area showing the satisfied restraints between NusG, uS10 and RNAP.

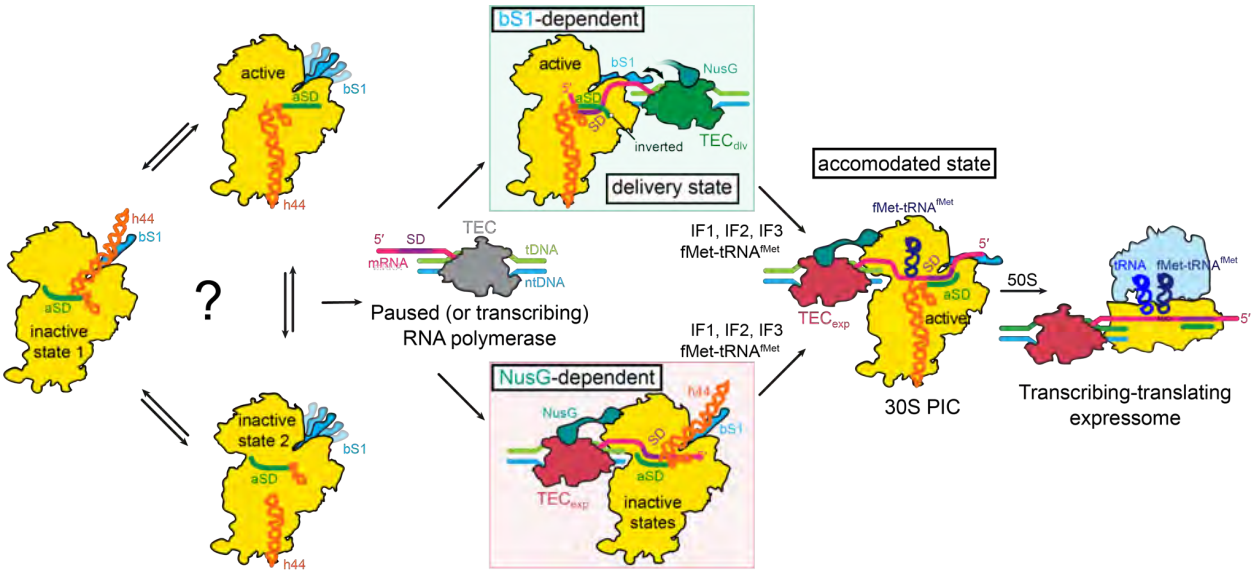

Fig. S10. Working model for 30S recruitment to the TEC and establishment of coupling between the TEC and the ribosome. Free 30S may interconvert between active and inactive states *in vivo* according to RNA SHAPE probing but their prevalence is currently unknown (*22*, *23*). Inactive states observed in our study are characterized by h44 (orange) occupying the mRNA exit channel and interacting with bS1 (left, inactive state 1) or h44 not correctly folding on the subunit interface side (left, inactive state 2). The aSD occupies a position overlapping with the ribosomal A-Site in the main mRNA binding channel in inactive states (aSD highlighted in green, left).

In the bS1-dependent pathway (top, green box) a TEC (grey) encounters active or inactive 30S and bS1 binds and guides the nascent mRNA for inverted SD-aSD duplex formation (delivery state, 30S active). Initiation factors (IF1, IF2, and IF3) and fMet-tRNA^{fMet} may support formation of a bona-fide 30S PIC with an accommodated mRNA and this may enable the TEC to occupy the expressome position (TEC$_{exp}$, middle, accommodated state).

Alternatively, in the NusG-dependent pathway, the TEC binds and is tethered to inactive 30S by NusG (teal) but fails to activate the small subunit (bottom, red box). Initiation factors allow full activation so both pathways lead to formation of a transcribing-translating expressome (middle, right).

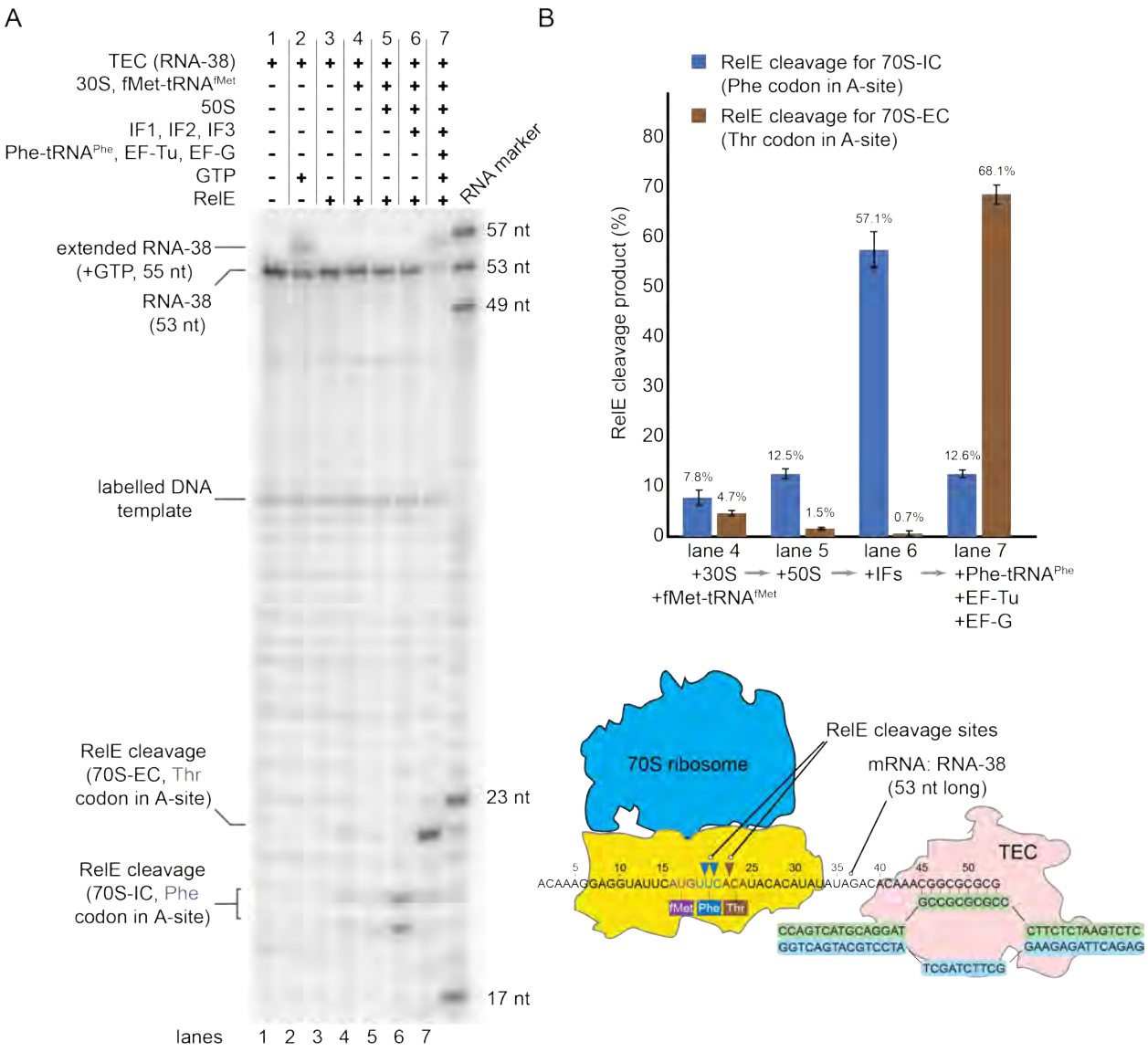

Fig. S11. RelE cleavage assay and quantification to confirm functional 70S complex formation. (**A**) Complexes of a TEC and a ribosome were formed stepwise analogous to cryo-EM grid preparation (see Materials and Methods). A TEC with RNA-38 was formed, purified by size-exclusion chromatography, and the nascent RNA was labeled with ^{32}P-γ-ATP (lane 1). Addition of GTP confirms TEC activity (lane 2) – note that DNA design ensures a stable transcription bubble that disfavors RNA extension (see schematic bottom right) . Addition of RelE (lanes 3-7) cleaves the mRNA of a 70S ribosome with an empty A-site. Addition of 50S, or 50S and translation initiation factors (IF1, IF2, and IF3) leads to increasing formation of functional 70S ribosomes (compare lanes 4, 5, and 6). Further addition of EF-Tu, Phe-tRNA^{Phe}, EF-G, and GTP shows complete 70S translocation and RNA extension by the TEC (compare also schematic at the bottom right). Note the RelE produces 2 cleavage products in a 70S initiation complex (70S-IC) when fMet-tRNA^{fMet} is bound in the P-site (e.g. lanes 5 and 6) but only one after translocation with Phe-tRNA^{Phe} in the P-site (70S elongation complex – 70S-EC, lane 7). (**B**) Quantification of three

independent experiments suggests IFs increase the fraction of functional 70S ribosomes. IFs may support activation of 30S in 30S-TEC_{exp} and may support mRNA accommodation in both 30S-TEC_{exp} and 30S-TEC_{dlv} complexes.

Table S1. Cryo-EM data collection, refinement, and validation statistics

Cryo-EM reconstructions	30S-PIC (no TEC)	30S-TEC$_{exp}$ Inactive state 1	30S-TEC$_{exp}$ Inactive state 2	30S-TEC$_{dlv}$ (TEC$_{dlv}$ resolved)		30S$_{dlv}$ (bS1 resolved)	30S$_{dlv}$ (mRNA delivery consensus)	30S$_{dlv}$ (mRNA delivery, open head)	30S$_{dlv}$ (mRNA delivery, closed head)	70S-TEC$_{dlv}$
				30S	TEC$_{dlv}$					
PDB IDs	9GUQ	9GUX	9GUW	9GUS	9GUR	9GUT	9GUU	9GUP	9GUV	9GR1
EMDB IDs										
Composite maps	EMD-51616	EMD-51623	EMD-51622	EMD-51618	EMD-51617	EMD-51619	EMD-51620	EMD-51615	EMD-51621	
Consensus maps	EMD-51602	EMD-51596	EMD-51591	EMD-51584		EMD-51580	EMD-51576	EMD-51572	EMD-51587	EMD-51517
30S focused head maps	EMD-51603	EMD-51597	EMD-51592	EMD-51585		EMD-51581	EMD-51577	EMD-51573	EMD-51588	
30S focused body maps	EMD-51604	EMD-51598	EMD-51593	EMD-51586		EMD-51582	EMD-51578	EMD-51574	EMD-51589	
30S focused platform maps		EMD-51599	EMD-51594	EMD-51601		EMD-51583	EMD-51579	EMD-51575	EMD-51590	
focused TEC maps		EMD-51600	EMD-51595							EMD-51517
Data collection and Processing										
Microscope	Titan KRIOS	Titan KRIOS	Titan KRIOS	Titan KRIOS	Titan KRIOS	Titan KRIOS	Titan KRIOS	Titan KRIOS	Titan KRIOS	Titan KRIOS
Voltage (keV	300	300	300	300	300	300	300	300	300	300
Camera	Gatan K3	Gatan K3	Gatan K3	Gatan K3	Gatan K3	Gatan K3	Gatan K3	Gatan K3	Gatan K3	Gatan K2
Magnification	105K	105K	105K	105K	105K	105K	105K	105K	105K	105K
Pixel size at detector (e^-/Å)	0.84	0.84	0.84	0.84	0.84	0.84	0.84	0.84	0.84	1.052
Total electron exposure (e^-/Å^{-2})	49.95	49.95	49.95	49.95	49.95	49.95	49.95	49.95	49.95	42
Exposure Rate (e^-/pixel/sec)	18.55	18.55	18.55	18.55	18.55	18.55	18.55	18.55	18.55	6.4
Number of frames collected during exposure	50	50	50	50	50	50	50	50	50	40
Automation software	Serial-EM	Serial-EM	Serial-EM	Serial-EM	Serial-EM	Serial-EM	Serial-EM	Serial-EM	Serial-EM	Serial-EM
Defocus range (μm)	-0.8 to -2	-0.8 to -2	-0.8 to -2	-0.8 to -2	-0.8 to -2	-0.8 to -2	-0.8 to -2	-0.8 to -2	-0.8 to -2	-0.8 to -2
Energy filter slit width	20	20	20	20	20	20	20	20	20	20
Micrographs used	25,899	25,899	25,899	25,899	25,899	25,899	25,899	25,899	25,899	8,524
Total extracted particles	3,085,141	3,085,141	3,085,141	3,085,141	3,085,141	3,085,141	3,085,141	3,085,141	3,085,141	546,512
For each reconstruction										
Final Particles	20,551	11,965	20,703	7,284	7,284	51,717	256,024	52,113	112,399	39,139
Point-group symmetry	C1	C1	C1	C1	C1	C1	C1	C1	C1	C1
Nominal resolution (Å)	3.1	3.3	3.1	3.5	4.2	2.8	2.6	2.8	2.7	3.2
FSC 0.5 (masked/unmasked)	3.7/9.13	4.2/14.45	3.69/10.69	4.37/17.18	6.96/20.62	3.24/9.22	2.9/5.48	3.2/8.94	3.01/6.87	3.71/7.25
FSC 0.143 (masked/unmasked)	3.1/4.8	3.3/8.38	3.07/6.63	3.48/9.12	4.19/10.30	2.9/5.17	2.6/3.74	2.8/4.97	2.7/4.07	3.14/3.92
Resolution range (local at FSC 0.5 Å)	1.8 - 53.41	1.7 - 58.06	1.7 – 53.61	1.78 – 58.1	3.91 – 70.421	2.4 – 48.44	2.1 - 44.72	2.4 – 49.2	1.8 – 44.7	2.9 – 51.7
Map sharpening B-factor (Å^2)										
Consensus	-61.6	-38.4	-49.91	-44.4	-56.6	-61.0	-76.5	-63.3	-72.3	-86.8
30S head focused	-54.8	-50.7	-58	-57.9		-63.8	-76.1	-61.6	-68.5	
30S body focused	-54.8	-47.93	-57.1	-48.6		-64.0	-75.4	-62.1	-70.3	
30S platform focused		-46.2	-53.1	-61.4		-61.0	-73.7	-62.1	-67.9	
Model composition.										
Non-hydrogen atoms	55193	81311	80595	55373	26790	58207	55336	53689	55998	142297
Protein residues	2523	6026	5870	2597	3271	2939	2596	2595	2774	5617
RNA bases	1641	1594	1572	1634	16	1633	1633	1556	1633	4556

DNA bases		60	60		60					
Ligands (Zn^{2+}/Mg^{2+})	126	2/133	3/119	125	2/1	137	120	86	86	1/420
Model refinement										
Refinement package (real space)	Phenix 1.21.2	Phenix 1.21.2	Phenix 1.21.2	Phenix 1.21.2	Phenix 1.21.2	Phenix 1.21.2	Phenix 1.21.2	Phenix 1.21.2	Phenix 1.21.2	Phenix 1.21.2
Nominal resolution (Å)	3.1	3.3	3.1	3.5	4.2	2.9	2.5	2.8	2.6	3.1
Map cross-correlation (within mask)	0.89	0.81	0.80	0.83	0.80	0.85	0.81	0.85	0.87	0.72
Model-to-map FSC 0.50	3.2	3.7	3.1	3.5	4.6	2.9	2.8	3	2.9	3.3
Average B factor protein ($Å^2$)	99.70	75.00	94.18	95.60	217.44	73.51	34.48	66.83	62.34	20.95
Average B factor nucleotide ($Å^2$)	116.58	85.99	74.62	106.93	268.00	71.96	34.10	70.03	65.18	20.73
RMS deviation										
Bond lengths (Å)	0.050	0.007	0.007	0.008	0.003	0.021	0.003	0.007	0.007	0.008
Bond angles (°)	0.605	0.848	0.829	0.774	0.579	1.209	0.554	0.729	0.744	0.756
Validation										
Molprobity Score	2.64	2.7	2.38	2.18	2.05	2.25	2.25	2.3	2.3	1.79
CaBLAM outlliers	2.7	2.80	2.07	1.87	3.19	2.5	2.03	1.9	2.3	
Molprobity Clash score	9	14	11	10	6	9	6	9	6	7.94
Rotamer outliers (%)	5.29	6.5	4.6	3.32	2.47	5.9	3.4	5.9	6.7	1.42
C-beta deviations	0.00	0.00	0.00	0.00	0.00	0.00	0.00	0.00	0.00	0.00
Ramachandran plot										
Favored (%)	91.49	93.37	95.81	96.24	94.06	97.23	96.35	96.63	95.75	96.35
Allowed (%)	8.43	5.99	4.02	3.64	5.85	2.59	3.36	3.26	3.96	3.43
Outliers (%)	0.08	0.64	0.2	0.12	0.09	0.1	0.27	0.12	0.29	0.22

Table S1. Summary of data collection and refinement statistics.

Table S2. Oligonucleotides used in this study

Oligonucleotide	Sequence (5′-3′)
template DNA (tDNA), Cryo-EM	CTCTGAATCTCTTCCCGCGCGCCGTAGGACGTACTGACC
non-template DNA (ntDNA), Cryo-EM	GGTCAGTACGTCCTATCGATCTTCGGAAGAGATTCAGAG
RNA-38, Cryo-EM	ACAAAGGAGGUAUUCAUGUUCACAUACACAUAUAUAGACACA AACGGCGCGCG
RNA-16, EMSA	GAGUCCGCGGCGCGCG
MF38 (1), SiM-KARB	TCCAGATCCCGAAAATTTATCAAAAAGAGTATTGACTTAAAGTC TAACCTATAGGATACTTACAGCCACAAAGGAGGTATTCATGTTC AC
MF38-CP, SiM-KARB	AGACCACGTTGAAAGATTGGGTTACCGCGCGCCGTTTGTGTCTA TATATGTGTATGTGAACATGAATACCTCCTTTGTGGC
MF38-EC, SiM-KARB	/5Biosg/TTGGGTTACCGCGCGCCGTTTGTGTCTATATATGTGTATG TGAACATGAATACCTCCTTTGTGGC
Anchor_bio, SiM-KARB	/5Biosg/AGACCACGTTGAAAGATTGGGTTAC
Hp5extn._ribo_5Cy5_3Cy5, SiM-KARB	/5Cy5/AAAGGGAGATCAGGATATAAAG/3Cy5Sp/

Table S3: Kinetic parameters extracted from 30S binding assay

Construct	30S	k_{on} (10^7 M^{-1} s^{-1})	k_{off} (s^{-1})
RNA-38	WT	Fast[a]: 30.6 ± 0.1 (35%) Slow[a]: 1.70 ± 0.01 (65%) Overall[b]: 11.4 ± 1.1	Fast[a]: 0.23 ± 0.01 (91%) Slow[a]: 0.02 ± 0.01 (9%) Overall[b]: 0.32 ± 0.16
	ΔS1	Fast[a]: 26.3 ± 0.1 (45%) Slow[a]: 1.65 ± 0.01 (55%) Overall[b]: 12.55 ± 0.35	Fast[a]: 0.37 ± 0.01 (69%) Slow[a]: 0.07 ± 0.01 (31%) Overall[b]: 0.25 ± 0.01
pTEC-38	WT	Fast[a]: 31.5 ± 0.1 (48%) Slow[a]: 2.41 ± 0.02 (52%) Overall[b]: 14.85 ± 0.63	Fast[a]: 0.19 ± 0.01 (83%) Slow[a]: 0.03 ± 0.01 (17%) Overall[b]: 0.23 ± 0.14
	ΔS1	Fast[a]: 27.4 ± 0.1 (28%) Slow[a]: 2.52 ± 0.02 (72%) Overall[b]: 8.83 ± 0.56	Fast[a]: 0.46 ± 0.01 (64%) Slow[a]: 0.07 ± 0.01 (36%) Overall[b]: 0.32 ± 0.01

[a]Values were calculated from single or double-exponential fits of the pool data from all the experiments in a given condition. The percentages indicate the contribution of each phase to the overall rate constant. The reported error is the standard deviation (SD) of the fit. In the case of single-exponential fit only one value is reported arbitrary as a fast rate constant.

[b]Values represent the average ± the standard deviation (SD) of the mean from independent experiments.

Table S4: 30S subunit and TEC domains that define approximate boundaries used for masking in focused refinements, classifications, and signal subtraction (note that masks can be combined or subtracted from each other)

Masked region	Ribosomal proteins	16S rRNA residues	DNA	fMet-tRNA^{fMet}, mRNA
30S head (all complexes)	uS3 (chain D) uS7 (chain H) uS9 (chain J) uS10 (chain K) uS13 (chain N) uS14 (chain O) uS19 (chain T) NusG-CTD (chain Z)	residues 930-1068 and 1107-1387 (chain A)		fMet-tRNA^{fMet} (30S-PIC)
30S body (including 30S platform; all complexes)	bS1 (chain B) uS2 (chain C) uS4 (chain E) uS5 (chain F) bS6 (chain G) uS8 (chain I) uS11 (chain L) uS12 (chain M) uS15 (chain P) bS16 (chain Q) uS17(chain R) bS18 (chain S) bS20 (chain U) uS21 (chain V)	residues 1-929, 1069-1106 and 1388-1544 (chain A)		
30S body (excluding 30S platform; all complexes)	uS2 (chain C) uS4 (chain E) uS5 (chain F) uS8 (chain I) uS12 (chain M) bS16 (chain Q) uS17(chain R) bS20 (chain U)	residues 1-567, 591-649,916-929, 1069-1106 and 1388-1544 (chain A)		Optional fMet-tRNA^{fMet} ($30S_{dlv}$ closed head conformation)
30S platform (all complexes)	bS1 (chain B) bS6 (chain G) uS11 (chain L) uS15 (chain P) bS18 (chain S) uS21 (chain V)	residues 568-590 and 650-915 (chain A)		
h44		residues 1400-1502 (chain A)		

TEC_{dlv} or TEC_{exp}	$\alpha 1$ (chain 1) $\alpha 2$ (chain 2) β (chain 3) β' (chain 4) ω (chain 5) NusG- NTD (chain Z)		template DNA (chain 6) non-template DNA (chain 7) mRNA (chain W)	mRNA (chain W) residues ~38-53

Movie S1. The 30S head oscillates in the mRNA delivery complexes. In the mRNA delivery complexes no mRNA is accommodated in the main mRNA binding channel of the 30S subunit because it is instead bound by bS1. The head domain exhibits a large degree of rotational freedom with respect to the 30S body and this enables opening of the mRNA binding channel and may facilitate mRNA accommodation. In addition, fMet-tRNA^{fMet} (purple) appears to preferentially bind to 30S subunits with a closed head domain. The tRNA backbone in the anticodon stem, and elbow region contacts positively charged and polar residues in ribosomal proteins uS2, uS3, uS4, and uS5 on the solvent side of the 30S neck region.

Movie S2. TEC$_{exp}$ movements relative to the 30S ribosomal subunit. 3D variability analysis in CryoSPARC using a mask covering the TEC$_{exp}$ reveals that the NusG-coupled TEC$_{exp}$ (red) bound in the expressome position and coupled through NusG (teal) to ribosomal protein uS10 does not occupy a single, stable orientation relative to the 30S ribosomal subunit. Instead, it can rotate and translate relative to the ribosome consistent with results obtained for NusG-coupled expressomes (*27*).

Movie S3. The Shine-Dalgarno anti-Shine-Dalgarno helix adopts an inverted position in the mRNA delivery complexes. The mRNA exit channel is lined by several ribosomal proteins (bS1, cyan; uS2 salmon; bS18, orange; bS21, blue). The cryo-EM density for the SD-aSD helix is not consistent with the orientation it adopts in a canonical pre-initiation complex (30S-PIC). Instead, the aSD rotates approximately around rRNA residue 1533. This facilitates the mRNA to be delivered and annealed to the aSD so the 3′-end points towards bS1 and TEC$_{dlv}$ instead of the tRNA binding sites on the ribosome.

Movie S4. h44 and bS1 movements in inactive state 1 relative to the 30S ribosomal subunit. The base of h44 occupies the mRNA exit channel in inactive state 1 consistent with late 30S maturation intermediates (*39*). 3D variability analysis in CryoSPARC using a mask covering the mRNA exit channel reveals that bS1 OB2 can bind h44. In contrast, the interactions between OB3 and h44 seem more transient and suggest an equilibrium exists between OB domains binding and detaching from h44 to allow mRNA binding by bS1 and h44 accommodation on the 30S subunit interface.

Data S1. Complete list of crosslinked peptides from in cell crosslinking mass spectrometry. The complete list is available as an excel file for download.

References and Notes

1. M. A. Sørensen, J. Fricke, S. Pedersen, Ribosomal protein S1 is required for translation of most, if not all, natural mRNAs in *Escherichia coli* in vivo. *J. Mol. Biol.* **280**, 561–569 (1998). doi:10.1006/jmbi.1998.1909 Medline

2. J. Shine, L. Dalgarno, The 3′-terminal sequence of *Escherichia coli* 16*S* ribosomal RNA: Complementarity to nonsense triplets and ribosome binding sites. *Proc. Natl. Acad. Sci. U.S.A.* **71**, 1342–1346 (1974). doi:10.1073/pnas.71.4.1342 Medline

3. J. A. Steitz, K. Jakes, How ribosomes select initiator regions in mRNA: Base pair formation between the 3′ terminus of 16*S* rRNA and the mRNA during initiation of protein synthesis in *Escherichia coli*. *Proc. Natl. Acad. Sci. U.S.A.* **72**, 4734–4738 (1975). doi:10.1073/pnas.72.12.4734 Medline

4. K. Saito, R. Green, A. R. Buskirk, Translational initiation in *E. coli* occurs at the correct sites genome-wide in the absence of mRNA-rRNA base-pairing. *eLife* **9**, e55002 (2020). doi:10.7554/eLife.55002 Medline

5. C. Backendorf, C. J. C. Ravensbergen, J. Van der Plas, J. H. van Boom, G. Veeneman, J. Van Duin, Basepairing potential of the 3′ terminus of 16*S* RNA: Dependence on the functional state of the 30*S* subunit and the presence of protein S21. *Nucleic Acids Res.* **9**, 1425–1444 (1981). doi:10.1093/nar/9.6.1425 Medline

6. B. M. Burmann, S. H. Knauer, A. Sevostyanova, K. Schweimer, R. A. Mooney, R. Landick, I. Artsimovitch, P. Rösch, An α helix to β barrel domain switch transforms the transcription factor RfaH into a translation factor. *Cell* **150**, 291–303 (2012). doi:10.1016/j.cell.2012.05.042 Medline

7. S. Chatterjee, A. Chauvier, S. S. Dandpat, I. Artsimovitch, N. G. Walter, A translational riboswitch coordinates nascent transcription-translation coupling. *Proc. Natl. Acad. Sci. U.S.A.* **118**, e2023426118 (2021). doi:10.1073/pnas.2023426118 Medline

8. H. El Sayyed, O. J. Pambos, M. Stracy, M. E. Gottesman, A. N. Kapanidis, Single-molecule tracking reveals the functional allocation, in vivo interactions, and spatial organization of universal transcription factor NusG. *Mol. Cell* **84**, 926–937.e4 (2024). doi:10.1016/j.molcel.2024.01.025 Medline

9. T. Yokoyama, Y. Murayama, T. Uchikubo-Kamo, Y. Tomabechi, A. Nagao, T. Suzuki, M. Shirouzu, S. Sekine, Structural insight into bacterial co-transcriptional translation initiation. *bioRxiv*, 2024.03.19.585385 (2024).

10. M. Irastortza-Olaziregi, O. Amster-Choder, Coupled transcription-translation in prokaryotes: An l. *Front. Microbiol.* **11**, 624830 (2021). doi:10.3389/fmicb.2020.624830

11. M. W. Webster, A. Weixlbaumer, Macromolecular assemblies supporting transcription-translation coupling. *Transcription* **12**, 103–125 (2021). doi:10.1080/21541264.2021.1981713 Medline

12. G. Demo, A. Rasouly, N. Vasilyev, V. Svetlov, A. B. Loveland, R. Diaz-Avalos, N. Grigorieff, E. Nudler, A. A. Korostelev, Structure of RNA polymerase bound to ribosomal 30*S* subunit. *eLife* **6**, e28560 (2017). doi:10.7554/eLife.28560 Medline

13. P. Milón, M. V. Rodnina, Kinetic control of translation initiation in bacteria. *Crit. Rev. Biochem. Mol. Biol.* **47**, 334–348 (2012). doi:10.3109/10409238.2012.678284 Medline

14. M. A. Canonaco, C. O. Gualerzi, C. L. Pon, Alternative occupancy of a dual ribosomal binding site by mRNA affected by translation initiation factors. *Eur. J. Biochem.* **182**, 501–506 (1989). doi:10.1111/j.1432-1033.1989.tb14856.x Medline

15. M. H. de Smit, J. van Duin, Translational standby sites: How ribosomes may deal with the rapid folding kinetics of mRNA. *J. Mol. Biol.* **331**, 737–743 (2003). doi:10.1016/S0022-2836(03)00809-X Medline

16. S. M. Studer, S. Joseph, Unfolding of mRNA secondary structure by the bacterial translation initiation complex. *Mol. Cell* **22**, 105–115 (2006). doi:10.1016/j.molcel.2006.02.014 Medline

17. C. O. Gualerzi, C. L. Pon, Initiation of mRNA translation in bacteria: Structural and dynamic aspects. *Cell. Mol. Life Sci.* **72**, 4341–4367 (2015). doi:10.1007/s00018-015-2010-3 Medline

18. X. Qu, L. Lancaster, H. F. Noller, C. Bustamante, I. Tinoco Jr., Ribosomal protein S1 unwinds double-stranded RNA in multiple steps. *Proc. Natl. Acad. Sci. U.S.A.* **109**, 14458–14463 (2012). doi:10.1073/pnas.1208950109 Medline

19. M. Duval, A. Korepanov, O. Fuchsbauer, P. Fechter, A. Haller, A. Fabbretti, L. Choulier, R. Micura, B. P. Klaholz, P. Romby, M. Springer, S. Marzi, *Escherichia coli* ribosomal protein S1 unfolds structured mRNAs onto the ribosome for active translation initiation. *PLOS Biol.* **11**, e1001731 (2013). doi:10.1371/journal.pbio.1001731 Medline

20. A. Zamir, R. Miskin, D. Elson, Interconversions between inactive and active forms of ribosomal subunits. *FEBS Lett.* **3**, 85–88 (1969). doi:10.1016/0014-5793(69)80103-1 Medline

21. D. Moazed, B. J. Van Stolk, S. Douthwaite, H. F. Noller, Interconversion of active and inactive 30 S ribosomal subunits is accompanied by a conformational change in the decoding region of 16 S rRNA. *J. Mol. Biol.* **191**, 483–493 (1986). doi:10.1016/0022-2836(86)90143-9 Medline

22. J. L. McGinnis, Q. Liu, C. A. Lavender, A. Devaraj, S. P. McClory, K. Fredrick, K. M. Weeks, In-cell SHAPE reveals that free 30*S* ribosome subunits are in the inactive state. *Proc. Natl. Acad. Sci. U.S.A.* **112**, 2425–2430 (2015). doi:10.1073/pnas.1411514112 Medline

23. D. Jahagirdar, V. Jha, K. Basu, J. Gomez-Blanco, J. Vargas, J. Ortega, Alternative conformations and motions adopted by 30*S* ribosomal subunits visualized by cryo-electron microscopy. *RNA* **26**, 2017–2030 (2020). doi:10.1261/rna.075846.120 Medline

24. R. A. Mooney, S. E. Davis, J. M. Peters, J. L. Rowland, A. Z. Ansari, R. Landick, Regulator trafficking on bacterial transcription units in vivo. *Mol. Cell* **33**, 97–108 (2009). doi:10.1016/j.molcel.2008.12.021 Medline

25. M. H. Larson, R. A. Mooney, J. M. Peters, T. Windgassen, D. Nayak, C. A. Gross, S. M. Block, W. J. Greenleaf, R. Landick, J. S. Weissman, A pause sequence enriched at translation start sites drives transcription dynamics in vivo. *Science* **344**, 1042–1047 (2014). doi:10.1126/science.1251871 Medline

26. S. Ray, S. S. Dandpat, S. Chatterjee, N. G. Walter, Precise tuning of bacterial translation initiation by non-equilibrium 5′-UTR unfolding observed in single mRNAs. *Nucleic Acids Res.* **50**, 8818–8833 (2022). doi:10.1093/nar/gkac635 Medline

27. M. W. Webster, M. Takacs, C. Zhu, V. Vidmar, A. Eduljee, M. Abdelkareem, A. Weixlbaumer, Structural basis of transcription-translation coupling and collision in bacteria. *Science* **369**, 1355–1359 (2020). doi:10.1126/science.abb5036 Medline

28. T. Hussain, J. L. Llácer, B. T. Wimberly, J. S. Kieft, V. Ramakrishnan, Large-scale movements of IF3 and tRNA during bacterial translation initiation. *Cell* **167**, 133–144.e13 (2016). doi:10.1016/j.cell.2016.08.074 Medline

29. G. D'Urso, S. Chat, R. Gillet, E. Giudice, Structural insights into the binding of bS1 to the ribosome. *Nucleic Acids Res.* **51**, 3410–3419 (2023). doi:10.1093/nar/gkad126 Medline

30. G. Yusupova, L. Jenner, B. Rees, D. Moras, M. Yusupov, Structural basis for messenger RNA movement on the ribosome. *Nature* **444**, 391–394 (2006). doi:10.1038/nature05281 Medline

31. A. Korostelev, S. Trakhanov, H. Asahara, M. Laurberg, L. Lancaster, H. F. Noller, Interactions and dynamics of the Shine Dalgarno helix in the 70*S* ribosome. *Proc. Natl. Acad. Sci. U.S.A.* **104**, 16840–16843 (2007). doi:10.1073/pnas.0707850104 Medline

32. A. B. Loveland, A. A. Korostelev, Structural dynamics of protein S1 on the 70*S* ribosome visualized by ensemble cryo-EM. *Methods* **137**, 55–66 (2018). doi:10.1016/j.ymeth.2017.12.004 Medline

33. B. Beckert, M. Turk, A. Czech, O. Berninghausen, R. Beckmann, Z. Ignatova, J. M. Plitzko, D. N. Wilson, Structure of a hibernating 100S ribosome reveals an inactive conformation of the ribosomal protein S1. *Nat. Microbiol.* **3**, 1115–1121 (2018). doi:10.1038/s41564-018-0237-0 Medline

34. K. Byrgazov, I. Grishkovskaya, S. Arenz, N. Coudevylle, H. Temmel, D. N. Wilson, K. Djinovic-Carugo, I. Moll, Structural basis for the interaction of protein S1 with the *Escherichia coli* ribosome. *Nucleic Acids Res.* **43**, 661–673 (2015). doi:10.1093/nar/gku1314 Medline

35. J. Y. Kang, R. A. Mooney, Y. Nedialkov, J. Saba, T. V. Mishanina, I. Artsimovitch, R. Landick, S. A. Darst, Structural basis for transcript elongation control by NusG family universal regulators. *Cell* **173**, 1650–1662.e14 (2018). doi:10.1016/j.cell.2018.05.017 Medline

36. C. Zhu, X. Guo, P. Dumas, M. Takacs, M. Abdelkareem, A. Vanden Broeck, C. Saint-André, G. Papai, C. Crucifix, J. Ortiz, A. Weixlbaumer, Transcription factors modulate RNA polymerase conformational equilibrium. *Nat. Commun.* **13**, 1546 (2022). doi:10.1038/s41467-022-29148-0 Medline

37. M. V. Sukhodolets, S. Garges, Interaction of *Escherichia coli* RNA polymerase with the ribosomal protein S1 and the Sm-like ATPase Hfq. *Biochemistry* **42**, 8022–8034 (2003). doi:10.1021/bi020638i Medline

38. C. Wang, V. Molodtsov, E. Firlar, J. T. Kaelber, G. Blaha, M. Su, R. H. Ebright, Structural basis of transcription-translation coupling. *Science* **369**, 1359–1365 (2020). doi:10.1126/science.abb5317 Medline

39. A. Schedlbauer, I. Iturrioz, B. Ochoa-Lizarralde, T. Diercks, J. P. López-Alonso, J. L. Lavin, T. Kaminishi, R. Çapuni, N. Dhimole, E. de Astigarraga, D. Gil-Carton, P. Fucini, S. R. Connell, A conserved rRNA switch is central to decoding site maturation on the small ribosomal subunit. *Sci. Adv.* **7**, 7 (2021). doi:10.1126/sciadv.abf7547 Medline

40. M. Belinite, I. Khusainov, H. Soufari, S. Marzi, P. Romby, M. Yusupov, Y. Hashem, Stabilization of ribosomal RNA of the small subunit by spermidine in *Staphylococcus aureus*. *Front. Mol. Biosci.* **8**, 738752 (2021). doi:10.3389/fmolb.2021.738752 Medline

41. M. Dorywalska, S. C. Blanchard, R. L. Gonzalez, H. D. Kim, S. Chu, J. D. Puglisi, Site-specific labeling of the ribosome for single-molecule spectroscopy. *Nucleic Acids Res.* **33**, 182–189 (2005). doi:10.1093/nar/gki151 Medline

42. F. Krupp, N. Said, Y. H. Huang, B. Loll, J. Bürger, T. Mielke, C. M. T. Spahn, M. C. Wahl, Structural basis for the action of an all-purpose transcription anti-termination factor. *Mol. Cell* **74**, 143–157.e5 (2019). doi:10.1016/j.molcel.2019.01.016 Medline

43. S. Marzi, A. G. Myasnikov, A. Serganov, C. Ehresmann, P. Romby, M. Yusupov, B. P. Klaholz, Structured mRNAs regulate translation initiation by binding to the platform of the ribosome. *Cell* **130**, 1019–1031 (2007). doi:10.1016/j.cell.2007.07.008 Medline

44. S. Nakagawa, Y. Niimura, T. Gojobori, Comparative genomic analysis of translation initiation mechanisms for genes lacking the Shine-Dalgarno sequence in prokaryotes. *Nucleic Acids Res.* **45**, 3922–3931 (2017). doi:10.1093/nar/gkx124 Medline

45. K. R. Andersen, N. C. Leksa, T. U. Schwartz, Optimized *E. coli* expression strain LOBSTR eliminates common contaminants from His-tag purification. *Proteins* **81**, 1857–1861 (2013). doi:10.1002/prot.24364 Medline

46. Y. Zhang, U. Werling, W. Edelmann, SLiCE: A novel bacterial cell extract-based DNA cloning method. *Nucleic Acids Res.* **40**, e55 (2012). doi:10.1093/nar/gkr1288 Medline

47. K. A. Twist, S. I. Husnain, J. D. Franke, D. Jain, E. A. Campbell, B. E. Nickels, M. S. Thomas, S. A. Darst, L. F. Westblade, A novel method for the production of in vivo-assembled, recombinant *Escherichia coli* RNA polymerase lacking the α C-terminal domain. *Protein Sci.* **20**, 986–995 (2011). doi:10.1002/pro.622 Medline

48. X. Guo, A. G. Myasnikov, J. Chen, C. Crucifix, G. Papai, M. Takacs, P. Schultz, A. Weixlbaumer, Structural basis for NusA stabilized transcriptional pausing. *Mol. Cell* **69**, 816–827.e4 (2018). doi:10.1016/j.molcel.2018.02.008 Medline

49. M. N. Vassylyeva, J. Lee, S. I. Sekine, O. Laptenko, S. Kuramitsu, T. Shibata, Y. Inoue, S. Borukhov, D. G. Vassylyev, S. Yokoyama, Purification, crystallization and initial crystallographic analysis of RNA polymerase holoenzyme from *Thermus thermophilus*. *Acta Crystallogr. D Biol. Crystallogr.* **58**, 1497–1500 (2002). doi:10.1107/S0907444902011770 Medline

50. D. Moazed, S. Stern, H. F. Noller, Rapid chemical probing of conformation in 16 S ribosomal RNA and 30 S ribosomal subunits using primer extension. *J. Mol. Biol.* **187**, 399–416 (1986). doi:10.1016/0022-2836(86)90441-9 Medline

51. G. Blaha, U. Stelzl, C. M. T. Spahn, R. K. Agrawal, J. Frank, K. H. Nierhaus, Preparation of functional ribosomal complexes and effect of buffer conditions on tRNA positions

observed by cryoelectron microscopy. *Methods Enzymol.* **317**, 292–309 (2000). doi:10.1016/S0076-6879(00)17021-1 Medline

52. Y. Shimizu, A. Inoue, Y. Tomari, T. Suzuki, T. Yokogawa, K. Nishikawa, T. Ueda, Cell-free translation reconstituted with purified components. *Nat. Biotechnol.* **19**, 751–755 (2001). doi:10.1038/90802 Medline

53. R. Jünemann, J. Wadzack, F. J. Triana-Alonso, J. U. Bittner, J. Caillet, T. Meinnel, K. Vanatalu, K. H. Nierhaus, In vivo deuteration of transfer RNAs: Overexpression and large-scale purification of deuterated specific tRNAs. *Nucleic Acids Res.* **24**, 907–913 (1996). doi:10.1093/nar/24.5.907 Medline

54. E. Cayama, A. Yépez, F. Rotondo, E. Bandeira, A. C. Ferreras, F. J. Triana-Alonso, New chromatographic and biochemical strategies for quick preparative isolation of tRNA. *Nucleic Acids Res.* **28**, E64 (2000). doi:10.1093/nar/28.12.e64 Medline

55. S. Q. Zheng, E. Palovcak, J.-P. Armache, K. A. Verba, Y. Cheng, D. A. Agard, MotionCor2: Anisotropic correction of beam-induced motion for improved cryo-electron microscopy. *Nat. Methods* **14**, 331–332 (2017). doi:10.1038/nmeth.4193 Medline

56. A. Punjani, J. L. Rubinstein, D. J. Fleet, M. A. Brubaker, cryoSPARC: Algorithms for rapid unsupervised cryo-EM structure determination. *Nat. Methods* **14**, 290–296 (2017). doi:10.1038/nmeth.4169 Medline

57. K. Zhang, Gctf: Real-time CTF determination and correction. *J. Struct. Biol.* **193**, 1–12 (2016). doi:10.1016/j.jsb.2015.11.003 Medline

58. J. Zivanov, T. Nakane, B. O. Forsberg, D. Kimanius, W. J. H. Hagen, E. Lindahl, S. H. W. Scheres, New tools for automated high-resolution cryo-EM structure determination in RELION-3. *eLife* **7**, e42166 (2018). doi:10.7554/eLife.42166 Medline

59. T. D. Goddard, C. C. Huang, E. C. Meng, E. F. Pettersen, G. S. Couch, J. H. Morris, T. E. Ferrin, UCSF ChimeraX: Meeting modern challenges in visualization and analysis. *Protein Sci.* **27**, 14–25 (2018). doi:10.1002/pro.3235 Medline

60. E. F. Pettersen, T. D. Goddard, C. C. Huang, E. C. Meng, G. S. Couch, T. I. Croll, J. H. Morris, T. E. Ferrin, UCSF ChimeraX: Structure visualization for researchers, educators, and developers. *Protein Sci.* **30**, 70–82 (2021). doi:10.1002/pro.3943 Medline

61. J. Agirre, M. Atanasova, H. Bagdonas, C. B. Ballard, A. Baslé, J. Beilsten-Edmands, R. J. Borges, D. G. Brown, J. J. Burgos-Mármol, J. M. Berrisford, P. S. Bond, I. Caballero, L. Catapano, G. Chojnowski, A. G. Cook, K. D. Cowtan, T. I. Croll, J. É. Debreczeni, N. E. Devenish, E. J. Dodson, T. R. Drevon, P. Emsley, G. Evans, P. R. Evans, M. Fando, J. Foadi, L. Fuentes-Montero, E. F. Garman, M. Gerstel, R. J. Gildea, K. Hatti, M. L. Hekkelman, P. Heuser, S. W. Hoh, M. A. Hough, H. T. Jenkins, E. Jiménez, R. P. Joosten, R. M. Keegan, N. Keep, E. B. Krissinel, P. Kolenko, O. Kovalevskiy, V. S. Lamzin, D. M. Lawson, A. A. Lebedev, A. G. W. Leslie, B. Lohkamp, F. Long, M. Malý, A. J. McCoy, S. J. McNicholas, A. Medina, C. Millán, J. W. Murray, G. N. Murshudov, R. A. Nicholls, M. E. M. Noble, R. Oeffner, N. S. Pannu, J. M. Parkhurst, N. Pearce, J. Pereira, A. Perrakis, H. R. Powell, R. J. Read, D. J. Rigden, W. Rochira, M. Sammito, F. Sánchez Rodríguez, G. M. Sheldrick, K. L. Shelley, F. Simkovic, A. J. Simpkin, P. Skubak, E. Sobolev, R. A. Steiner, K. Stevenson, I. Tews, J. M. H. Thomas, A. Thorn, J. T. Valls, V. Uski, I. Usón, A. Vagin, S. Velankar, M. Vollmar, H. Walden, D. Waterman,

K. S. Wilson, M. D. Winn, G. Winter, M. Wojdyr, K. Yamashita, The CCP4 suite: Integrative software for macromolecular crystallography. *Acta Crystallogr. D Struct. Biol.* **79**, 449–461 (2023). doi:10.1107/S2059798323003595 Medline

62. Z. L. Watson, F. R. Ward, R. Méheust, O. Ad, A. Schepartz, J. F. Banfield, J. H. D. Cate, Structure of the bacterial ribosome at 2 Å resolution. *eLife* **9**, e60482 (2020). doi:10.7554/eLife.60482 Medline

63. P. Emsley, B. Lohkamp, W. G. Scott, K. Cowtan, Features and development of Coot. *Acta Crystallogr. D Biol. Crystallogr.* **66**, 486–501 (2010). doi:10.1107/S0907444910007493 Medline

64. J. Jumper, R. Evans, A. Pritzel, T. Green, M. Figurnov, O. Ronneberger, K. Tunyasuvunakool, R. Bates, A. Žídek, A. Potapenko, A. Bridgland, C. Meyer, S. A. A. Kohl, A. J. Ballard, A. Cowie, B. Romera-Paredes, S. Nikolov, R. Jain, J. Adler, T. Back, S. Petersen, D. Reiman, E. Clancy, M. Zielinski, M. Steinegger, M. Pacholska, T. Berghammer, S. Bodenstein, D. Silver, O. Vinyals, A. W. Senior, K. Kavukcuoglu, P. Kohli, D. Hassabis, Highly accurate protein structure prediction with AlphaFold. *Nature* **596**, 583–589 (2021). doi:10.1038/s41586-021-03819-2 Medline

65. D. Liebschner, P. V. Afonine, M. L. Baker, G. Bunkóczi, V. B. Chen, T. I. Croll, B. Hintze, L. W. Hung, S. Jain, A. J. McCoy, N. W. Moriarty, R. D. Oeffner, B. K. Poon, M. G. Prisant, R. J. Read, J. S. Richardson, D. C. Richardson, M. D. Sammito, O. V. Sobolev, D. H. Stockwell, T. C. Terwilliger, A. G. Urzhumtsev, L. L. Videau, C. J. Williams, P. D. Adams, Macromolecular structure determination using X-rays, neutrons and electrons: Recent developments in Phenix. *Acta Crystallogr. D Struct. Biol.* **75**, 861–877 (2019). doi:10.1107/S2059798319011471 Medline

66. A. J. Rinaldi, P. E. Lund, M. R. Blanco, N. G. Walter, The Shine-Dalgarno sequence of riboswitch-regulated single mRNAs shows ligand-dependent accessibility bursts. *Nat. Commun.* **7**, 8976 (2016). doi:10.1038/ncomms9976 Medline

67. M. A. Lauber, J. Rappsilber, J. P. Reilly, Dynamics of ribosomal protein S1 on a bacterial ribosome with cross-linking and mass spectrometry. *Mol. Cell. Proteomics* **11**, 1965–1976 (2012). doi:10.1074/mcp.M112.019562 Medline

68. A. E. Dahlberg, Two forms of the 30 S ribosomal subunit of *Escherichia coli*. *J. Biol. Chem.* **249**, 7673–7678 (1974). doi:10.1016/S0021-9258(19)81289-9 Medline

69. M. Kitagawa, T. Ara, M. Arifuzzaman, T. Ioka-Nakamichi, E. Inamoto, H. Toyonaga, H. Mori, Complete set of ORF clones of *Escherichia coli* ASKA library (a complete set of *E. coli* K-12 ORF archive): Unique resources for biological research. *DNA Res.* **12**, 291–299 (2005). doi:10.1093/dnares/dsi012 Medline

70. L. Lancaster, H. F. Noller, Involvement of 16*S* rRNA nucleotides G1338 and A1339 in discrimination of initiator tRNA. *Mol. Cell* **20**, 623–632 (2005). doi:10.1016/j.molcel.2005.10.006 Medline

71. A. Chauvier, J. Cabello-Villegas, N. G. Walter, Probing RNA structure and interaction dynamics at the single molecule level. *Methods* **162-163**, 3–11 (2019). doi:10.1016/j.ymeth.2019.04.002 Medline

72. J. R. Widom, Y. A. Nedialkov, V. Rai, R. L. Hayes, C. L. Brooks 3rd, I. Artsimovitch, N. G. Walter, Ligand modulates cross-coupling between riboswitch folding and transcriptional pausing. *Mol. Cell* **72**, 541–552.e6 (2018). doi:10.1016/j.molcel.2018.08.046 Medline

73. M. Blanco, N. G. Walter, "Analysis of complex single-molecule FRET time trajectories" in *Methods in Enzymology* (Elsevier, 2010), vol. 472, pp. 153–178.

74. L. Kolbowski, M. L. Mendes, J. Rappsilber, Optimizing the parameters governing the fragmentation of cross-linked peptides in a tribrid mass spectrometer. *Anal. Chem.* **89**, 5311–5318 (2017). doi:10.1021/acs.analchem.6b04935 Medline

75. J. Cox, M. Mann, MaxQuant enables high peptide identification rates, individualized p.p.b.-range mass accuracies and proteome-wide protein quantification. *Nat. Biotechnol.* **26**, 1367–1372 (2008). doi:10.1038/nbt.1511 Medline

76. M. C. Chambers, B. Maclean, R. Burke, D. Amodei, D. L. Ruderman, S. Neumann, L. Gatto, B. Fischer, B. Pratt, J. Egertson, K. Hoff, D. Kessner, N. Tasman, N. Shulman, B. Frewen, T. A. Baker, M. Y. Brusniak, C. Paulse, D. Creasy, L. Flashner, K. Kani, C. Moulding, S. L. Seymour, L. M. Nuwaysir, B. Lefebvre, F. Kuhlmann, J. Roark, P. Rainer, S. Detlev, T. Hemenway, A. Huhmer, J. Langridge, B. Connolly, T. Chadick, K. Holly, J. Eckels, E. W. Deutsch, R. L. Moritz, J. E. Katz, D. B. Agus, M. MacCoss, D. L. Tabb, P. Mallick, A cross-platform toolkit for mass spectrometry and proteomics. *Nat. Biotechnol.* **30**, 918–920 (2012). doi:10.1038/nbt.2377 Medline

77. M. L. Mendes, L. Fischer, Z. A. Chen, M. Barbon, F. J. O'Reilly, S. H. Giese, M. Bohlke-Schneider, A. Belsom, T. Dau, C. W. Combe, M. Graham, M. R. Eisele, W. Baumeister, C. Speck, J. Rappsilber, An integrated workflow for crosslinking mass spectrometry. *Mol. Syst. Biol.* **15**, e8994 (2019). doi:10.15252/msb.20198994 Medline

78. S. H. Giese, A. Belsom, L. Sinn, L. Fischer, J. Rappsilber, Noncovalently associated peptides observed during liquid chromatography-mass spectrometry and their affect on cross-link analyses. *Anal. Chem.* **91**, 2678–2685 (2019). doi:10.1021/acs.analchem.8b04037 Medline

79. G. C. P. van Zundert, A. M. J. J. Bonvin, DisVis: Quantifying and visualizing accessible interaction space of distance-restrained biomolecular complexes. *Bioinformatics* **31**, 3222–3224 (2015). doi:10.1093/bioinformatics/btv333 Medline